A Fractal Approach to
Structure Analysis and Micro-Mechanical Modeling
of Elastomer Materials

Dem Fachbereich Maschinenbau

der Universität Hannover

zur Erlangung der venia legendi im Fach

Polymere Werkstoffe

vorgelegte Habilitationsschrift

von

Dr. rer. nat. Manfred Klüppel

Deutsches Institut für Kautschuktechnologie e. V.

Eupener Str. 33

30519 Hannover

Abstract:

The paper considers the fractal nature of filler networks on different length scales and relates it to the specific reinforcing properties of active fillers in elastomer composites. On nanoscopic length scales, the surface structure and primary aggregate morphology of carbon blacks, the most widely used filler in technical rubber goods, are analyzed by static gas adsorption and transmission electron microscopy (TEM) techniques, respectively. They are found to be closely related to two distinct disordered growth mechanisms during carbon black processing, surface growth and aggregate growth. This implies that carbon blacks exhibit characteristic self-similar structures, which can be quantified by two fractal exponents, the surface and mass fractal dimension.

The role of disorder becomes also apparent on mesoscopic length scales of elastomer composites, where a filler network in formed due to attractive filler-filler interactions. An analysis of the dc-conductivity and dielectric properties of conductive carbon black-rubber composites indicates that no universal percolation structure is realized, but a superimposed kinetic aggregation mechanism of the particles takes place. The assumed kinetic cluster-cluster aggregation (CCA) of filler particles in elastomers is confirmed by the predicted scaling behavior of the small strain elastic modulus. The dielectric data demonstrate that charge transport above the percolation threshold is limited by a hopping or tunneling mechanism of charge carriers over small gaps of order 1 nm between adjacent carbon black particles. From this finding and a series of flocculation experiments of the uncross-linked composites at elevated temperature, a model of filler-filler bonds is developed. It indicates that the forces in filler clusters are transmitted by nanoscopic, flexible bridges of glassy polymer between adjacent particles, implying that a high flexibility and strength of filler clusters in elastomers is reached.

Based on the analysis of in-rubber morphology of filler particles and clusters on nanoscopic and mesoscopic length scales, a constitutive micro-mechanical model of stress softening and hysteresis of filler reinforced rubbers up to large strain is developed. It refers to a non-affine tube model of rubber elasticity, including hydrodynamic amplification of the rubber matrix by a fraction of rigid filler clusters with filler-filler bonds in the unbroken, virgin state. The filler-induced hysteresis is described by an anisotropic free energy density, considering the cyclic breakdown and re-aggregation of the residual fraction of more fragile filler clusters with already broken filler-filler bonds. Experimental investigations of the quasi-static stress-strain behavior of silica and carbon black filled rubbers up to large strain agree well with adaptations found by the developed model. The obtained microscopic material parameter appear reasonable, providing information on the mean size and distribution width of filler clusters, the tensile strength of filler-filler bonds and the polymer network chain density.

Contents:

Appendix:

A.   G. Heinrich and M. Klüppel, "A hypothetical mechanism of carbon black formation based on molecular ballistic deposition", Kautschuk Gummi Kunstst. **54**, 159 (2001).

B.   G. Heinrich and M. Klüppel, "Recent advances in the theory of filler networking in elastomers", Adv. Polym. Sci. **160**, 1 (2002)

C.   M. Klüppel and G. Heinrich, "Fractal structures in carbon black reinforced rubbers", Rubber Chem. Technol. **68**, 623 (1995).

D.   M. Klüppel, R. H. Schuster and G. Heinrich, "Structure and properties of reinforcing fractal filler networks in elastomers", Rubber Chem. Technol. **70**, 243 (1997).

E.   A. Bischoff, M. Klüppel and R. H. Schuster, "Mechanical behavior at low strain of microgel containing elastomers", Polym. Bulletin **40**, 283 (1998)

F.   M. Klüppel and J. Schramm, "A generalized tube model of rubber elasticity and stress-softening of filler reinforced elastomer systems", Macromol. Theory Simul. **9**, 742 (2000)

1.   Introduction

Since the development of fractal geometry by Mandelbrot [1,2] it has been learned that the apparently random structure of many colloidal aggregates formed in disorderly growth processes is subject to strong statistical constraints [3-8]. It is now well known that the fractal structure of colloidal aggregates results from the random movement , e.g. diffusion, of the aggregating particles that may be represented in computer simulations of cluster growth processes via random walks of single particles [3,9] or whole clusters [10,11]. Thereby, different universality classes of fractal aggregates can be distinguished by characteristic fractal exponents, dependent on the conditions of cluster growth [12].

In these studies we are primary interested in two classes of disorderly grown colloidal aggregates:

(i)   Clusters that are build in a diffusion limited cluster-cluster aggregation (CCA) process, where particles and clusters diffuse across each other and stick upon contact, irreversibly.

(ii)   Clusters resulting from a ballistic cluster-cluster aggregation process, where particles and clusters move on linear trajectories.

A physical realization of the CCA-process is found during fast gelation of colloids in solution, where physical (and not chemical) bonds between particles and clusters are formed. From light scattering data of corresponding gold-, silica- and polystyrene clusters as well as from computer simulations of CCA-clusters the fractal dimension takes the universal values $d_f \approx 1.8$ in all these cases [3-8,12,13]. The size distribution of the clusters is typically found to be broadly peaked around a maximum cluster size. This is in contrast to percolation clusters, where the size distribution shows a characteristic scaling behavior implying that the number of clusters increases successively with decreasing cluster size [6,7].

A physical realization of ballistic cluster-cluster aggregation is found during carbon black processing, where also surface growth due to random deposition of carbon nuclei takes place [14-18]. Corresponding computer simulations of primary aggregate formation under ballistic conditions yields for the mass fractal dimension $d_f \approx 1.95$ [11,12]. The surface growth of carbon black appears to be governed by a random deposition mechanism that falls into a universality class with a surface fractal dimension $d_s \approx 2.6$ [3,6,7,19]. We will consider the simultaneous cluster and surface growth of carbon black more closely in Section 3, where also the energetic surface structure is analyzed [20]. A reprint of Ref. 18, describing fractal models of carbon black surface formation, is found in Appendix A.

Recently it has been argued that CCA-clusters are also built in elastomer composites. Accordingly, their particular structure can be used for the modeling of rubber reinforcement by active fillers like carbon blacks or silica [21-25]. This

approach is not evident, because long range diffusion of filler particles or clusters, as assumed in the CCA-process, is strongly suppressed in high viscosity media. Instead, the polymeric structure of highly entangled rubbers give rise to fluctuations of colloidal particles around their mean position with a fluctuation length of the order of the entanglement length of the rubber [22-24]. For that reason the assumption of CCA-clusters in filler reinforced rubbers appears reasonable for sufficient large filler concentrations, only, where the mean trajectory length of aggregating particles or clusters becomes smaller than the fluctuation length. This condition is fulfilled for filler concentrations Φ above the gel point Φ^* of the filler network if the gelation concept of Ball and Brown is applied [25]. Then, the mean trajectory length in gelling systems becomes small and the cluster size is governed by the available empty space only. However, due to the restricted mobility of filler particles in rubber the gel point is shifted to filler concentrations that are orders of magnitude larger than the critical concentration Φ^* in solution [22,23]. This is the main difference between the two systems that appears to be important for rubber reinforcement. A reprint of Refs. 22, 23 and 24 is found in Appendix B, C and D, respectively.

Different concentration limits of the filler arise from the CCA concept [22]. With increasing filler concentration first an aggregation limit Φ^+ is reached. For $\Phi > \Phi^+$, the distance of neighboring filler particles becomes sufficiently small for the onset of flocculation and clusters with solid fraction Φ_A are formed. Dependent on the concentration of filler particles, this flocculation process leads to spatially separated clusters or, for $\Phi > \Phi^*$, a through going filler network that can be considered as a space-filling configuration of fractal CCA-clusters. The different cases for spherical filler particles are shown schematically in Fig. 1.

$$\Phi < \Phi^+ \qquad \Phi > \Phi^+ \qquad \Phi > \Phi^*$$

$$\Phi_{eff} = \Phi \qquad \Phi_{eff} = \Phi/\Phi_A$$

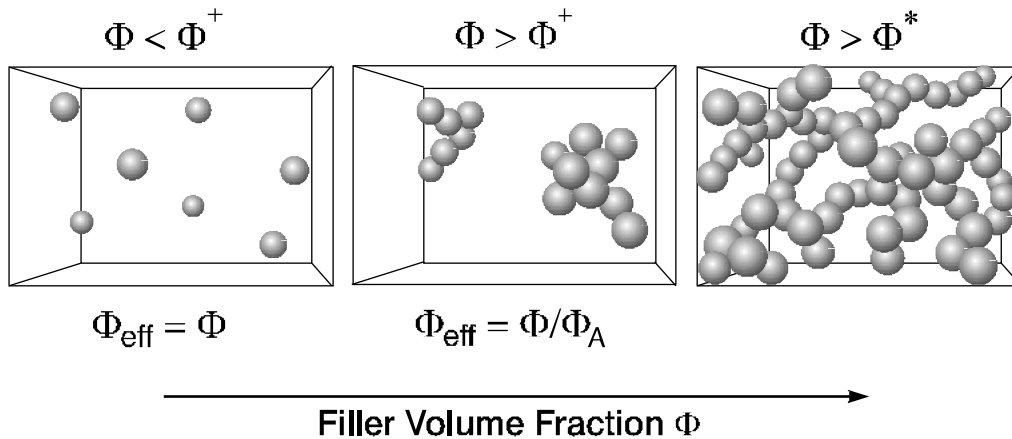Filler Volume Fraction Φ

Fig. 1: Schematic view of filler morphology in three concentration regimes. For $\Phi < \Phi^*$ reinforcement is due to hydrodynamic amplification by particles ($\Phi < \Phi^+$) or clusters ($\Phi > \Phi^+$) with $\Phi_{eff} = \Phi$ or $\Phi_{eff} = \Phi/\Phi_A$, respectively. For $\Phi > \Phi^*$ reinforcement is due to the deformation of a flexible filler network.

So far, the formation and structure of filler networks in elastomers and the mechanical response, e. g. the pronounced dynamic amplitude dependence or stress softening, of reinforced rubbers is not fully understood, though this question is of high technical interest. A deeper understanding of filler networking and reinforcement could provide a useful tool for the design, preparation and testing of high performance elastomers, as applied in tires, seals, bearings and other dynamically loaded elastomer components. Different attempts have been considered in the past that were primary focussing on the reinforcing mechanism of carbon black, the most widely used filler in rubber industry [26,27]. The strongly non-linear dynamic-mechanical response of carbon black filled rubbers, reflected primary by the amplitude dependence of the viscoelastic complex modulus, was brought into clear focus by the extensive work of Payne [28-35]. Therefore, this effect is often referred to as Payne effect.
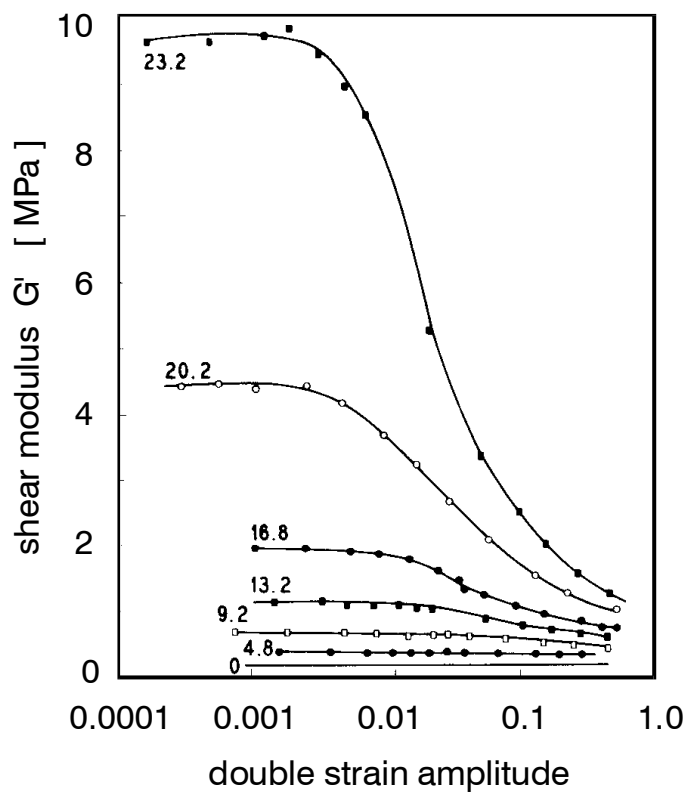
Fig. 2a: Amplitude dependence of the storage modulus of Butyl/N330-samples at various carbon black concentrations [28].

As shown in Fig. 2a, for a specific frequency and temperature, the storage modulus G' decreases from a small strain plateau value G'_o to an apparently high amplitude plateau value G'_∞ with increasing strain amplitude. The loss modulus G" shows a more or less pronounced peak. It can be evaluated from the tangent of the measured loss angle, tan δ = G"/G', as depicted in Fig. 2b. Obviously, the loss

tangent shows a low plateau value at small strain amplitude, almost independent of filler concentration, and passes through a broad maximum with increasing strain.
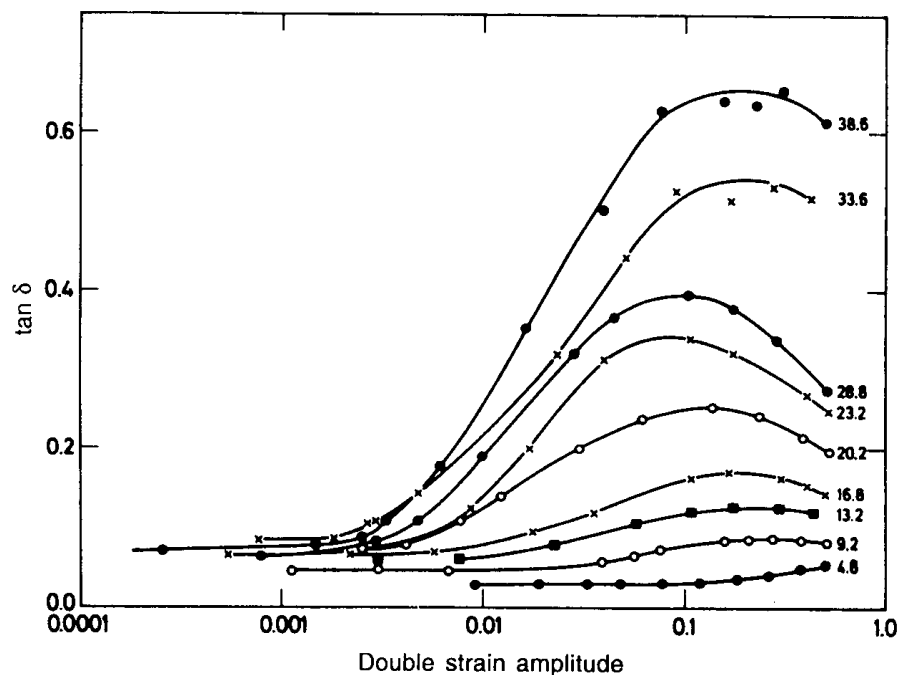

Fig. 2b: Amplitude dependence of the loss tangent of the Butyl/N330-samples shown in Fig. 2a at various carbon black concentrations [28].

The Payne effect of carbon black reinforced rubbers has also been investigated intensively by a number of different researchers [36-39]. In most cases, standard diene rubbers widely used in the tire industry, like SBR, NR and BR, have been applied, but also carbon black filled bromobutyl rubbers [40-42] or functional rubbers containing tin end-modified polymers [43] were used. The Payne effect was described in the framework of various experimental procedures, including pre-conditioning-, recovery- and dynamic stress-softening studies [44]. The typically almost reversible, non-linear response found for carbon black composites has also been observed for silica filled rubbers [44-46].

The temperature dependence of the Payne effect has been studied by Payne and other authors [28,32,47]. With increasing temperature an Arrhenius-like drop of the moduli is found, if the deformation amplitude is kept constant. Beside this effect, the impact of filler surface characteristics in the non-linear dynamic properties of filler reinforced rubbers has been discussed in a review of Wang [47], where basic theoretical interpretations and modeling is presented. The Payne effect has also been investigated in composites containing polymeric model fillers, like microgels of different particle size and surface chemistry, which could provide some more insight

8

into the fundamental mechanisms of rubber reinforcement by colloidal fillers [48,49]. A reprint of Ref. 48 is found in Appendix E.

The pronounced amplitude dependence of the complex modulus, referred to as Payne effect, has also been observed in low viscosity media, e. g. composites of carbon black with decane and liquid paraffin [50], carbon black suspensions in ethylene vinylacetate copolymers [51] and for clay/water suspensions [52,53]. It was found that the storage modulus decreases with dynamic strain amplitude in a qualitative manner similar to that of carbon black filled rubbers. This emphasizes the role of a physically bonded filler network structure in the Payne effect, which governs the small strain dynamic properties even in absence of rubber. Further, these results indicate that the Payne effect is primarily determined by structure effects of the filler. The elastomer seems to act merely as a dispersing medium that influences the kinetics of filler aggregation, but does not have a pronounced influence on the overall mechanical behavior of three-dimensional filler networks. However, the critical strain amplitude where the Payne effect appears is found to be shifted to significantly smaller values, if the low viscosity composites are compared to corresponding rubber composites. This indicates a strong impact of the polymer-matrix on the stability and strength of filler networks.

The strong non-linearity of the viscoelastic modulus with increasing dynamic strain amplitude has been related to a cyclic breakdown and re-aggregation of filler-filler bonds [21-24,48,54-56]. Thereby, different geometrical arrangements of particles in a particular filler network structure, resulting e. g. from percolation as in the L-N-B-model of Lin and Lee [56] or kinetic cluster-cluster aggregation [21-23,48], have been considered. Nevertheless, a full micro-mechanical description of energy storage and -dissipation in dynamically excited reinforced rubbers is still outstanding. A review of the different attempts is given in Appendix B.

Beside the Payne effect, relevant for dynamical loading of filler reinforced rubbers, the pronounced stress softening, characteristic for quasi-static deformations up to large strain, is of major interest for technical applications. It is often referred to as Mullins effect due to the extensive studies of Mullins and coworkers [58-60] on the stress softening phenomena. Dependent on the history of straining, e.g. the extent of previous stretching, the rubber material undergoes an almost permanent change that alters the elastic properties and increases hysteresis, drastically. Most of the softening occurs in the first deformation and after a few deformation cycles the rubber approaches a steady state with a constant stress-strain behavior. The softening is usually only present at deformations smaller than the previous maximum. An example of (discontinuous) stress softening is shown in Fig. 3, where the maximum strain is increased, successively, from one uniaxial stretching cycle to the next.
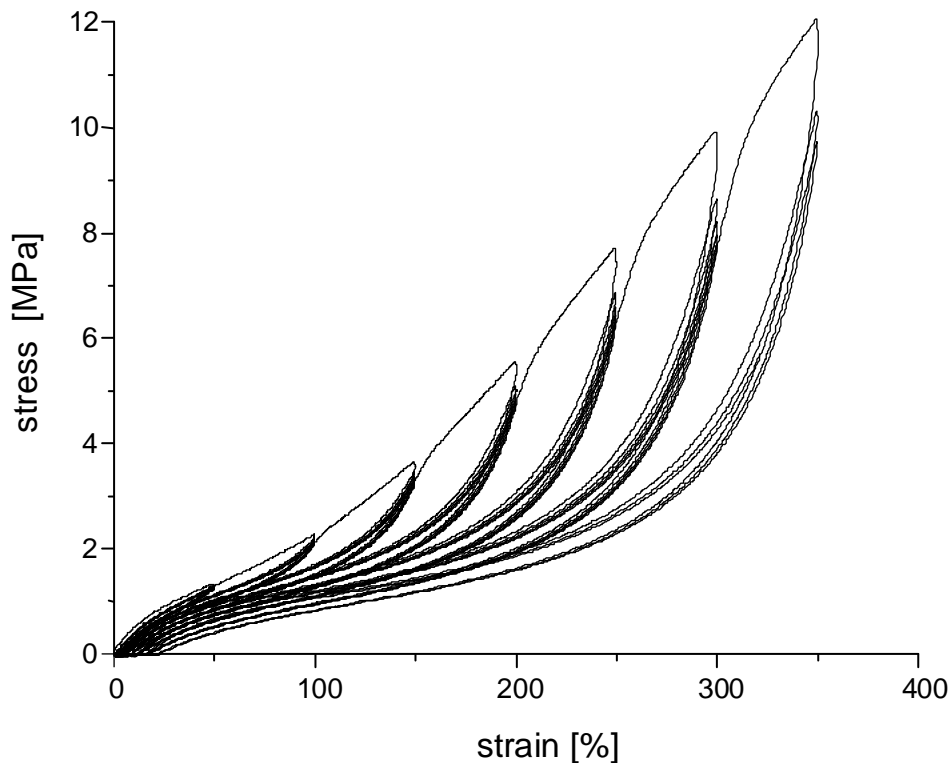
Fig. 3: Example of stress softening with successively increasing maximum strain after every fifth cycle for an S-SBR-sample filled with 50 phr carbon black.

So far the micro-mechanical origin of the Mullins effect is not totally understood [26,36,61]. Beside the action of the entropy elastic polymer network that is quite well understood on a molecular-statistical basis [57,62], the impact of filler particles on stress-strain properties is of high importance. On the one hand side the addition of hard filler particles leads to a stiffening of the rubber matrix that can be described by a hydrodynamic strain amplification factor [22,63-65]. On the other hand side the constraints introduced into the system by filler-polymer bonds result in a decreased network entropy. Accordingly, the free energy that equals the negative entropy times the temperature increases linear with the effective number of network junctions [64-67]. A further effect is obtained from the formation of filler clusters or a filler network due to strong attractive filler-filler bonds [21,22,26,36,61,64-67].

Stress softening is supposed to be affected by different influences and mechanisms that have been discussed by a variety of authors. In particular, it has been attributed to a breakdown or slippage [68-71] and dis-entanglements [72] of bonds between filler and rubber, a strain-induced crystallization-decrystallization [73,74] or a re-arrangement of network chain junctions in filled systems [60]. A model of stress-induced rupture or separation of network chains from the filler surface has been derived by Govindjee and Simo [69], who developed a complete macroscopic constitutive theory on the basis of statistical mechanics. A remarkable approach has been proposed by Witten et al. [21], who found a scaling law for the

stress-strain behavior in the first stretching cycle by modeling the breakdown of a CCA-network of filler particles. They used purely geometrical arguments by referring to the available space for the filler clusters in strained samples, leading to universal scaling exponents that involve the characteristic fractal exponents of CCA-clusters. However, they did not consider effects coming in from the rubber matrix or the polymer-filler interaction strength, though these are evident from experimental data, e. g. the impact of matrix cross-linking or filler surface treatment (graphitization) on stress-strain curves. It indicates that stress-induced breakdown of filler clusters takes place, where the stress on the filler clusters is transmitted by the rubber matrix.

The above interpretations of the Mullins effect of stress softening ignore the important results of Haarwood et al. [73,74], who showed that a plot of stress in second extension vs. ratio between strain and pre-strain of natural rubber filled with a variety of carbon blacks yields a single master curve [60,73]. This demonstrates that stress softening is related to hydrodynamic strain amplification due to the presence of the filler. Based on this observation a micro-mechanical model of stress softening has been developed by referring to hydrodynamic reinforcement of the rubber matrix by rigid filler clusters that are irreversibly broken during the first deformation cycle [75,76]. Thereby, a non-Gaussian tube model of rubber elasticity has been applied [[57],62,77,78]. A reprint of Ref. 76 is provided in Appendix F.

In the present paper we will first focus on the specific morphology and energetic surface properties of carbon black (Section 3). In particular, we will consider the surface roughness and activity on atomic length scales as obtained by recent gas adsorption investigations [20,79-82]. Then, we will concentrate on the primary aggregate structure that can be well characterized by TEM-measurements [83-85]. Both morphological characteristics of carbon black are compared to results of computer simulations and analytical models of disorderly growth processes under ballistic conditions [18,84]. In Section 4, we will consider the structures involved in secondary aggregation and networking of carbon black in elastomers [22,23] that has also been extended to elastomer blends [86,87]. We will discuss the developed model in the framework of experimental results concerning filler flocculation and dielectric properties of carbon black reinforced rubbers. Based on the investigations of carbon black morphology and energetic surface structure we will then develop a model of rubber reinforcement by kinetically aggregated filler networks in Section 5. We will first consider the linear viscoelastic behavior by referring to the elasticity of the fractal CCA-unit cells of the filler network [22-24,48,85,88]. Then, we will focus on a micro-mechanical concept of stress-induced filler cluster breakdown that combines the hyperelastic response of the hydrodynamically reinforced rubber matrix with the non-linear viscoelastic response of reversibly broken filler clusters [75,76,89]. It allows for an explanation of both, the Payne effect and the Mullins effect, by referring to a single micro-mechanical mechanism.

2.   Experimental

2.1   Materials

The following commercial rubber grades were applied for the preparation of filler reinforced composites:

(i)   natural rubber NR (SMR 5L; 99.9 vol.% cis),

(ii)   solution-styrene-butadiene rubber S-SBR (Buna VSL-2525-0; 25 vol.% vinyl, 25 vol. % styrene, M_w=206 600 g/mol, M_w/M_n = 2.75),

(iii)   solution-styrene-butadiene rubber S-SBR (Buna VSL-5025-0; 50 vol.% vinyl, 25 vol. % styrene, M_w=188 600 g/mol),

(iv)   emulsion-styrene-butadiene rubber E-SBR (Intol 1524; 15 vol.% vinyl, 23.5 vol.% styrene, M_w=205 300 g/mol, M_w/M_n = 2.12),

(v)   ethylene-propylene-diene rubber EPDM (Keltan 512; 55 vol.% ethylene)

(vi)   nitrile-butadiene rubber NBR (Perbunan 3307; 33 vol.% acryl-nitrile).

In addition to the commercial rubbers, model polymers (S-SBR; 29 vol.% vinyl, 25 vol.% styrene) with variable molar mass and narrow molecular weight distribution (M_w/M_n = 1.1) were applied in Section 4.3.

Manufacturing Process	Grade No.	N_2SA [m^2/g]	DBP-No. [ml/100 g]
channel-gas	-	267	-
furnace	N115	143	113
furnace	N134	152	107
furnace	N220	116	114
furnace	N234	128	125
furnace	N326	78	72
furnace	N330	81	102
furnace	N339	95	120
furnace	N550	41	121
furnace	N660	36	90
furnace	N772	29	72

Tab. 1:   List of carbon blacks and colloid properties; (N_2SA: Nitrogen surface area; DBP-No: di-butylphtalat absorption per hundred grams carbon black)

As reinforcing fillers, carbon blacks with different structure and specific surface area were employed as listed in Table 1. Furthermore, a commercial silica grade (Ultrasil GR 7000) together with a bi-functional silane (Si 69) as coating agent was applied (Section 5). The filler loading was ranging from very small amounts up to 100 phr. The notation "per hundred rubber" (phr), representing the mass (in grams) of an ingredient with respect to 100 grams of rubber, is widely used in rubber industry. The conversion to volume fraction Φ is obtained by the elementary formula $\Phi = phr / \rho_{CB} (100 \, g / \rho_{Pol} + phr / \rho_{CB})^{-1}$, where phr is the mass of carbon black (in grams) per 100 g polymer, while $\rho_{Pol} \approx 0.9 \, g/cm^3$ and $\rho_{CB} \approx 1.8 \, g/cm^3$ is the mass density of the pure polymer and carbon black, respectively. For silica the mass density is $\rho_{silica} \approx 1.9 \, g/cm^3$.

As polymeric model fillers with narrow size distribution, three different microgel types were applied: poly(styrene)-microgel, PS(m), and poly(methoxi-styrene)-microgel, PMS(m). These two were prepared by emulsion polymerization techniques as described in Appendix E. The third microgel was a commercial grade (Micromorph-1P) based on poly(styrene) with a weak surface functionalization (around 3 %) by OH-groups, allowing for a chemical coupling with the polymer matrix by the bi-functional silane (Si 69).

2.2 Sample preparation

The rubber composites were processed in an interlocking mixer (Werner & Pfleiderer GK 1.5 E) with a mixing chamber of 1500 cm^3. For obtaining a sufficient dispersion of the filler, 4 min mixing time was applied, unless otherwise stated. For the silica/silane- and microgel/silane systems a two step mixing procedure was applied to insure a sufficient silanization of the filler surfaces. In all cases, 2.5 phr ZnO and 1 phr stearinic acid was added. The mixer was filled up to 75% of its capacity for the specimens with less than 40 phr filler, 70% for loadings between 40 and 70 phr and 60% for more than 70 phr filler.

The cross-linking system (1.7 phr sulfur and 2.5 phr of the accelerator N-cyclohexylbenzothiazol-2-sulfenamide (CBS)) was added on a roller mill in a separate mixing step. For the EPDM-samples, the amount of cross-linker was increased by adding 1.5 phr of the accelerator diphenyl guanidine (DPG).

The composites with graphitized blacks were mixed on a roller mill for 20 minutes. The composites were cured in a steam press up to 90% of the rheometer optimum (T$_{90}$ time) at 160 °C.

2.3 Gas adsorption measurements

The morphological and energetic surface characterization of carbon black on atomic length scales was performed by volumetric gas adsorption techniques. A schematic view of three different application regimes of this technique is shown in Fig. 4. According to this scheme, the surface roughness of different carbon black grades and graphitized blacks was estimated in the mono- and multi-layer regime. Furthermore, a characterization of the energy distribution of adsorption sites of carbon black and other colloids was obtained in the sub-layer regime.

A classical volumetric adsorption apparatus equipped with absolute capacitance pressures transducers was used for the estimation of adsorption isotherms in the pressure range 10^{-3} mbar $< p < 10^3$ mbar. Before adsorption measurements the carbon black samples were extracted with toluene and water/methanol (1:1) and after drying degassed overnight at 200°C at a pressure below 10^{-4} mbar. The time allowed for equilibrium of each point of the isotherm was between five and ninety minutes depending on the sample and the adsorbed amount.
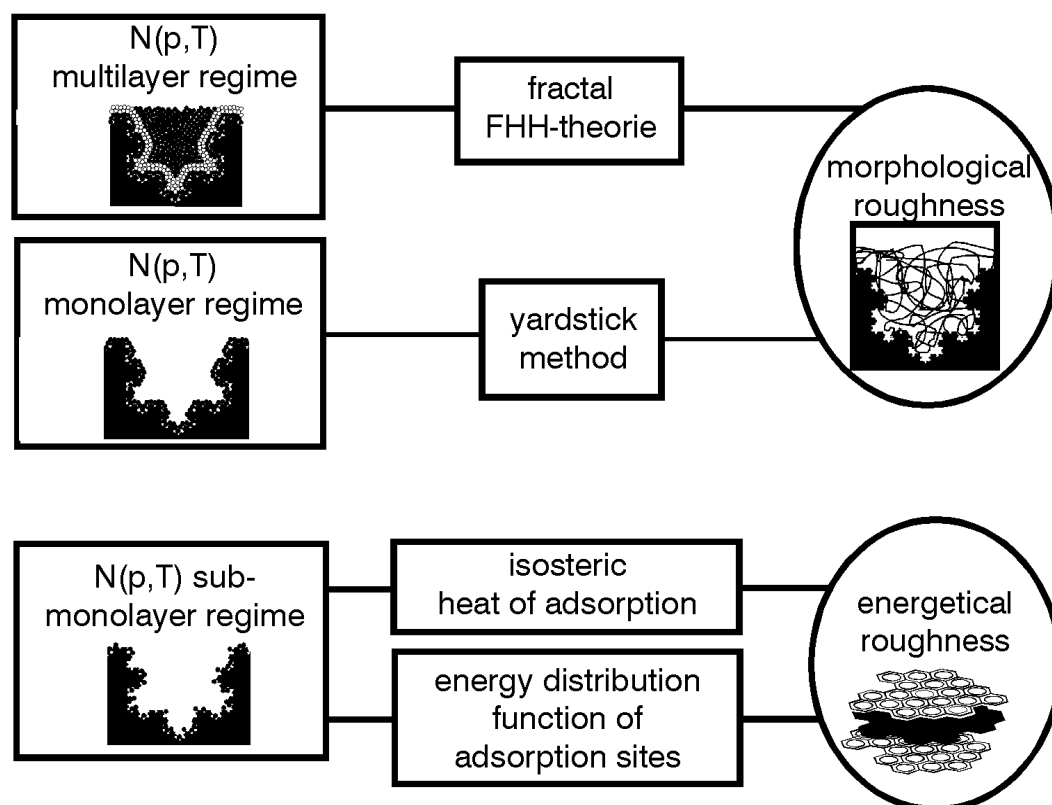
Fig. 4: Schematic representation of gas adsorption techniques in different layer regimes (decreasing pressure from top to bottom).

2.4   Microscopic techniques

The macro-dispersion of the fillers was determined by light-microscopic techniques with computer-assisted image processing on the light-microscope on glazed cuttings of the vulcanized samples. Five picture details were evaluated for each specimen. The dispersion coefficient D was calculated from the ratio of non-dispersed filler agglomerates and the volume fracture Φ of the filler in the composites in accordance with ASTM:D2663.

For the characterization of micro-dispersion, i. e. in rubber primary aggregate morphology of carbon black, the uncured composites were immersed for a week in a good solvent, with the solvent being changed a number of times in order to remove the unbounded polymer. Afterwards the specimens were dispersed in a vibrator. The highly diluted suspensions were then dipped on a grid and carefully condensed. Micro-graphs were taken using the Electron-Spectroscopy-Imaging-Transmission-Electron-Microscopy (ESI-TEM) technique on an EM 902 (Zeiß) equipment. For the evaluation of aggregate morphology (analogous to ASTM: 3849) roughly 500 particles of each carbon black type were measured with respect to cross-sectional area A, perimeter P and diameter d. This preparation procedure is indicated by the terminology "in rubber state".

In a second preparation procedure, referred to as "dry state", the carbon black was resolved in a solvent and dispersed by ultrasonic treatment. Afterwards, the highly diluted suspension was dipped on a grid and treated as above.

Further morphological investigations by TEM were performed on ultra-thin cuts (80 nm) obtained on an Ultra Cut FC 4E (Reichert-Jung) microtome. By making use of energy filters (ESI), the inelastically scattered electrons were removed. The micro-graphs provided by the elastically scattered electrons only show a good contrast based on the differences in carbon densities in the phases under consideration.

2.5   Mechanical analysis

Dynamic-mechanical testing of cross-linked samples was carried out on specimen strips (28 x 10 x 2 mm) with a Rheometrics Dynamic Analyzer II (RDA) in torsion mode. The temperature sweeps were performed at a frequency of 1 Hz and 0.5 % strain. The dynamic strain sweeps were carried out at a frequency of 1 Hz and a temperature of 20°C in a displacement range from 0.1% to 4% strain. Dynamic-mechanical measurements in uniaxial tension and compression direction were made with dumbbells by a 1000 Hz MTS-Hydropulser. Dynamic-mechanical testing of uncross-linked samples was performed with a Rubber Process Analyzer RPA 2000 (Alpha Technologies) from 0.28 % to 350 % strain at 60 °C and 160 °C, respectively.

The quasi-static mechanical testing of the vulcanized samples was performed with a tensile tester Zwick 1445. Uniaxial stress-strain measurements were carried out on (S2) strip-samples with cyclically increasing load (discontinuous damage mode) and up to rupture stress. The uniaxial hysteresis cycles in the small and medium strain regime and those in stretching-compression mode were obtained with dumbbells. Equi-biaxial stress-strain measurements were performed with a stretching frame by using quadratic sample sheets of size 100 x 100 mm and thickness 2 mm up to 110 % strain. The stretching velocity was chosen to be small (10 mm/min) in order to avoid dynamic contributions to the moduli. This corresponds to a strain rate of $\partial\varepsilon/\partial t \approx 10^{-2}$ s^{-1}.

2.6   Dielectric measurements

The samples were prepared as cross-linked sheets of a thickness between 1 and 2 mm. The dielectric measurements in a frequency range from 10^{-1} to 10^{7} Hz were performed using a frequency response analysis system consisting of a computer controlled Solartron SI 1260 Impedance/Gain-Phase Analyzer and a Novocontrol broadband dielectric converter. The high frequency measurements in the range from 10^{6} to 10^{9} Hz were performed in the wave reflection mode with an Agilent 4291B RF Impedance Analyzer.

3. The disordered nature of carbon black

Reinforcement of elastomers by colloidal fillers, like carbon black or silica, plays an important role in the improvement of mechanical properties of high performance rubber materials. The reinforcing potential is mainly attributed to two effects:

(i) the formation of a physically bonded flexible filler network and

(ii) strong polymer filler couplings.

Both of these effects refer to a high surface activity and specific surface of the filler particles [26,27,47]. In view of a deeper understanding of such structure-property relationships of filled rubbers it is useful to consider the morphological and energetic surface structure of carbon black particles as well as the primary and secondary aggregate structure in rubber more closely.

3.1 Surface roughness and activity on atomic length scales

3.1.1 Universality of carbon black surface roughness

For the characterization of surface roughness of carbon blacks, different experimental techniques have been applied in the past. Beside microscopic investigations, e. g. AFM that give an impressive but more qualitative picture [90-92], scattering techniques as SANS [93] and SAXS [94-96] as well as gas adsorption techniques [79-84,97-99] have been used for a fractal analysis of surface roughness. The results discussed in the literature appear somewhat controversy, since almost flat surfaces with $d_s \approx 2$ [98,99] and also rough surfaces with $2.2 < d_s < 2.6$ [79-84,93-96] are found.

The reason for these discrepancies lies on the one side in the restricted resolution of SANS and SAXS, since the scattering data could only be evaluated for wave vector $q_s < 1$ nm^{-1} in most cases. This corresponds to length scales larger than about 6 nm, while the gas adsorption data typically were obtained at length scales smaller than 6 nm. Recent investigations by SAXS have been extended down to smaller length scales with $q_s > 1$ nm^{-1}, where a scattering from the graphitic layers at the carbon surface was observed. It means that the surface scattering was shielded by that of sheet like structures [94]. On the other side the discrepancies between the gas adsorption results arise primary from the evaluation procedure of the effective cross-sections σ of the different gases, as far as the yardstick method in the mono-layer regime is concerned. The estimation of surface fractal dimensions in the multi-layer regime is complicated by the fact that contributions of two different surface potentials have to be considered, resulting from van-der-Waals- and surface tension interaction, respectively. Dependent on the dominance of one of the two potentials,

remarkably different estimates of surface roughness are obtained. For that reason a proper analysis of these factors is necessary for getting reliable results.

In the present paper we will summarize results of two different evaluation procedures for the surface roughness of carbon blacks. In the mono-layer regime we refer to the scaling behavior of the estimated BET-surface area with the size of adsorbed probe molecules (yardstick method). On smooth flat surfaces the BET-area is independent of the adsorbed probe or applied yardstick, while on rough surfaces it decreases with increasing probe (yardstick) size due to the inability of the large molecules to explore smaller cavities. This is shown schematically in Fig. 5.
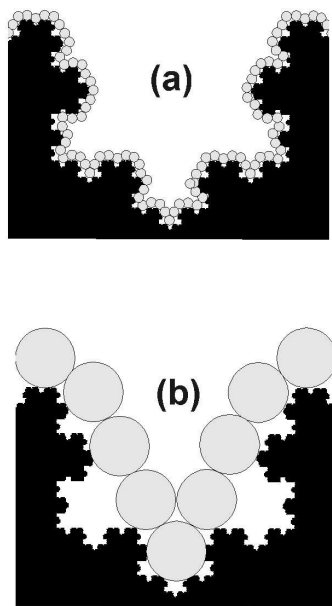

Fig. 5: Schematic presentation of a mono-layer coverage of a fractal surface with (a) small and (b) large gas molecules.

In the case of carbon black a power law behavior of the BET-surface area with varying yardstick size is observed, indicating a self-similar structure of the carbon black surface. Double logarithmic "yardstick-plots" of the BET-mono-layer amount N_m vs. cross-section σ of the probe molecules are shown in Fig. 6 for an original furnace black N220 and a graphitized (T=2500 °C) sample N220g. It demonstrates that the roughness exponent or surface fractal dimension d_s differs for the two carbon black samples. By using the relation introduced by Mandelbrot [1,2]:

$$N_m \sim \sigma^{-\frac{d_s}{2}} \qquad (1)$$

one obtains from the slopes of the two regression lines of Fig. 6 a surface fractal dimension $d_s \approx 2.56$ for the N220-sample and $d_s \approx 2.32$ for the graphitized N220g sample. An extrapolation of both regression lines yields an intersection at an ultimate cross-section that corresponds to a yardstick length of about 1 nm, indicating that graphitization reduces the roughness of carbon black on small length scales below 1 nm, only. Fig. 6 clearly demonstrates that the reduction of BET-surface area during graphitization is length scale (yardstick) dependent, proving that it is related to a change of surface morphology and not e. g. a result of reduced energetic surface activity (see below).
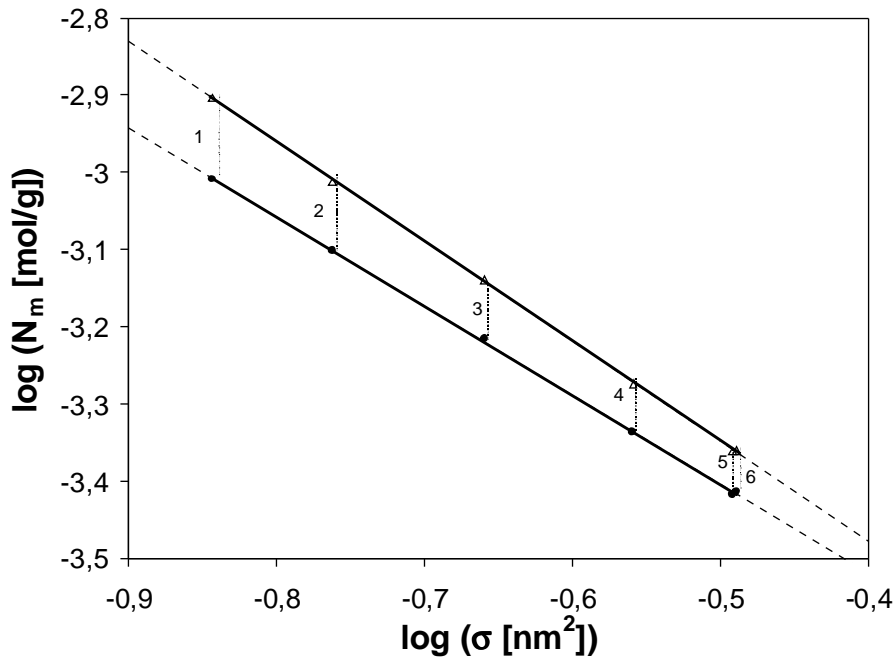

Fig. 6: Yardstick-plot (Equ.(1)) of N220 (△) and a graphitized N220g (●) with adsorption cross section σ determined from the bulk liquid density ρ (Equ.(2)); 1 argon, 2 methane, 3 ethane, 4 propane, 5 iso-butane, 6 n-butane; The slopes yield for N220: $d_s = 2.56 \pm 0.04$, for N220g: $d_s = 2.32 \pm 0.03$. Adsorption temperatures and densities ρ are chosen according to the evaporation points of the gases at 1000 mbar.

An important point in the above evaluation of carbon black surface morphology is the correct estimation of the cross-section σ of the applied probe molecules. This is done by referring to the mass density ρ of the probe molecules in the bulk liquid state that are considered as spheres in a hexagonal close packing:

$$\sigma = 1.091 \left(\frac{M}{N_a \rho} \right)^{2/3} \qquad (2)$$

Here, M is the molar mass of the probe molecules and N_a is the Avogadro number. The crucial point now is the temperature dependence of ρ that differs for the different probe molecules, mainly due to variations in the characteristic temperatures, e. g. the evaporation points.

We found that Equ. (2) can be applied without further corrections and high correlation coefficients of the "yardstick-plots" in Figs. 6 and 7 are obtained, only if the temperature during the adsorption experiments of a chemically similar, homological series of gases is chosen according to the same reference state, as defined in the framework of the theory of corresponding states. This is demonstrated in the "yardstick-plots" of Fig. 7, showing that for the same carbon black (N220g) a different scaling factor is obtained within one series of gases, if the adsorption temperatures are chosen with respect to different reference pressures, i. e. the evaporation temperatures at $p_o = 10^3$ mbar and $p_o = 10^4$ mbar, respectively.

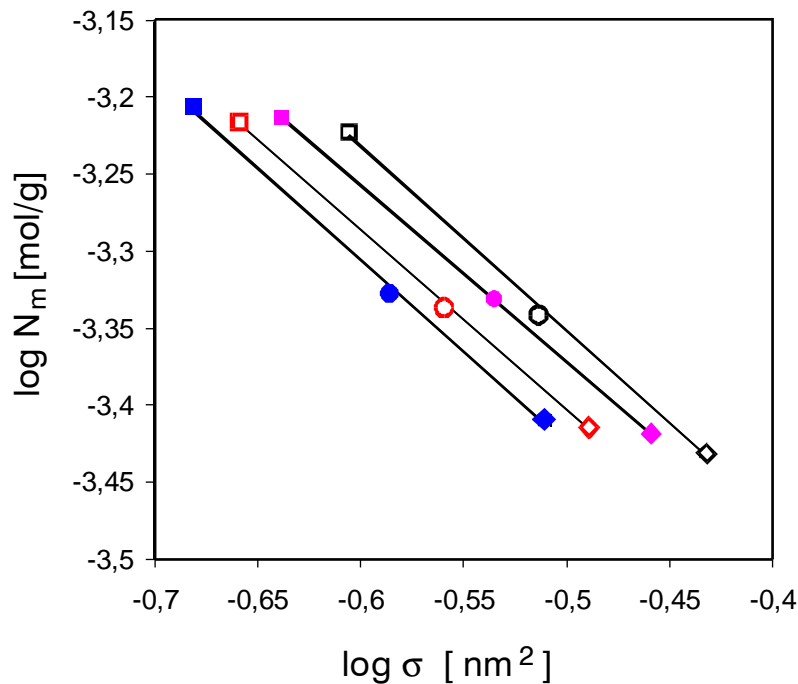**Fig. 7:** Yardstick-plots (Equ.(1)) of the graphitized black N220g obtained with a series of alkenes (ethylene, propylene, iso-butylene) (filled symbols) and alkanes (ethane, propane, iso-butane) (open symbols); Adsorption temperatures are chosen as evaporation points at vapor pressures $p_0 \approx 10^3$ mbar (lower curves) and $p_0 \approx 10^4$ mbar (upper curves) of the condensed gases, respectively.

As shown in Fig. 7, a different scaling factor is also observed for the two different homological series of gases, i.e. the alkanes and alkenes, respectively. However, the scaling exponent and hence the surface fractal dimension $d_s \approx 2.3$ is unaffected by the choice of the reference pressure or applied series of adsorption gases.

An alternative approach to the characterization of surface morphology of carbon blacks is the consideration of film formation of adsorbed molecules in the multi-layer regime. In this case, the surface roughness is evaluated with respect to a fractal extension of the classical Frenkel-, Halsey-, Hill (FHH)-theory, where beside the van der Waals surface potential the vapor-liquid surface tension has to be taken into account [100,101]. Then the Helmholtz free energy of the adsorbed film is given as the sum of the van der Waals attraction potential of all molecules in the film with all atoms in the adsorbent, the vapor-liquid surface free energy and the free energy of all molecules in the bulk liquid. This leads to the following relation between the adsorbed amount N and the relative pressure p/p_0 [100,101]:

$$N \sim \left(\ln \frac{p_o}{p} \right)^{-\vartheta} \tag{3}$$

with:
$$\vartheta = \frac{3 - d_s}{3} \qquad \text{FHH-regime} \tag{3a}$$

$$\vartheta = 3 - d_s \qquad \text{CC-regime} \tag{3b}$$

The different exponents for the FHH- and capillary condensation (CC)-regime consider the two cases where adsorption is dominated by the van der Waals potential and the vapor-liquid surface tension, respectively. The two cases are shown schematically in Figs. 8 (b) and (c), respectively. Note that in the CC-regime a flat vapor-liquid surface is obtained due to a minimization of curvature by the surface tension. Contrary, in the FHH-regime the vapor-liquid surface is curved, since it is located on equi-potential lines of the van der Waals potential with constant distance to the adsorbent surface.
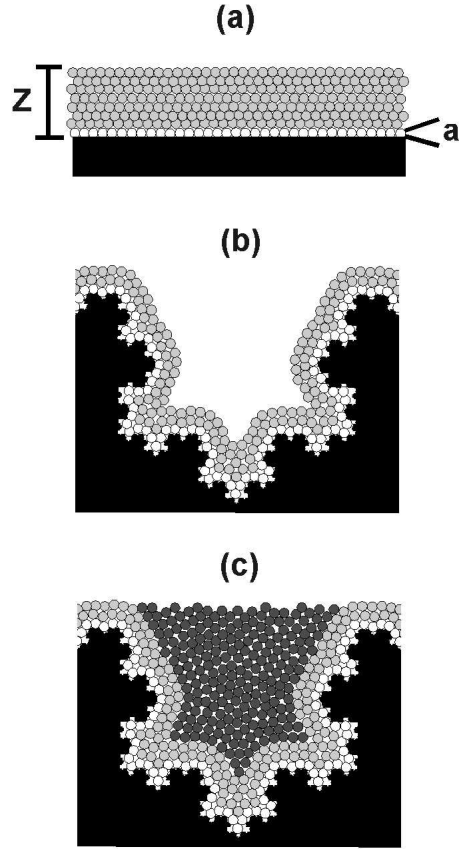
Fig. 8: Schematic view of the coverage of (a) a smooth and (b), (c) a fractal surface according to the fractal FHH-theory; ○ monolayer-regime, ◎ FHH-regime, ● CC-regime; z: average film thickness, a: monolayer thickness

At low relative pressures p/p_0 or thin adsorbate films, adsorption is expected to be dominated by the van der Waals attraction of the adsorbed molecules by the solid that falls off with the third power of the distance to the surface (FHH-regime, Equ. (3a)). At higher relative pressures p/p_0 or thick adsorbate films, the adsorbed amount N is expected to be determined by the surface tension γ of the adsorbate vapor interface (CC-regime, Equ. (3b)), because the corresponding surface potential falls off less rapidly with the first power of the distance to the surface, only. The cross-over length $z_{crit.}$ between both regimes depends on the number density n_p of probe molecules in the liquid, the surface tension γ, the van der Waals interaction parameter α as well as on the surface fractal dimension d_s [100,101] :

$$z_{crit.} = \sqrt{\frac{\alpha\, n_p}{(d_s - 2)\, \gamma}} \qquad (4)$$

Note, that the cross-over length $z_{crit.}$ decreases with increasing surface fractal dimension d_s, implying that the FHH-regime may not be observed on very rough surfaces, i.e. the film formation may be governed by the surface tension γ on all length scales $z > a$ (compare Fig. 10).

The film thickness z is related to the surface relative coverage N/N_m and the mean thickness $a \approx 0.35$ nm of one layer of nitrogen molecules [102] according to the scaling law [1,2]:

$$\frac{N}{N_m} = \left(\frac{z}{a}\right)^{3-d_s} \tag{5}$$

The monolayer amount N_m can be estimated from a classical BET-plot and hence the film thickness z can be obtained directly from the adsorbed amount N if the surface fractal dimension d_s is known.
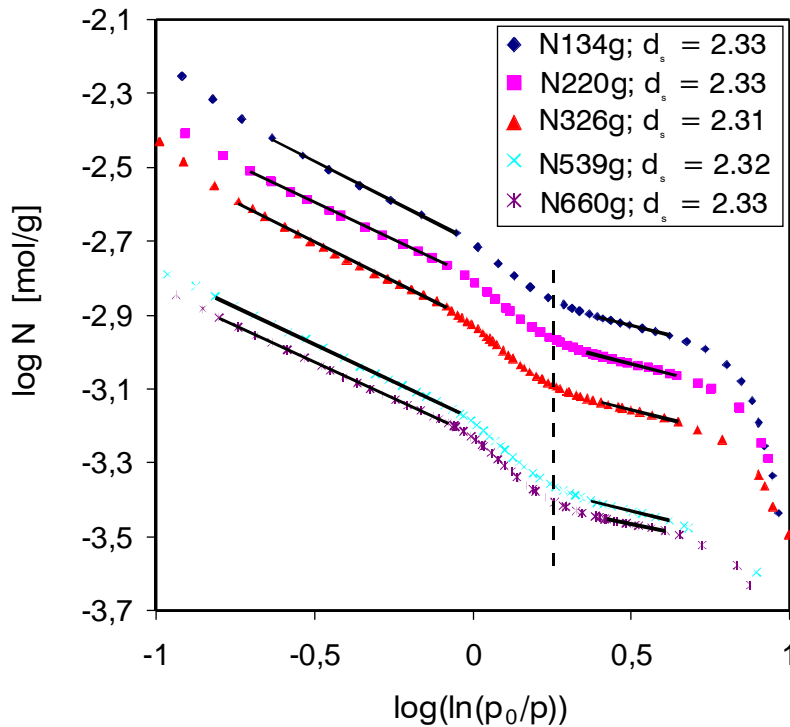
Fig. 9: FHH-plot of nitrogen adsorption isotherms at 77 K on various graphitized furnace blacks, as indicated. The dashed line characterizes the transition between the FHH- and the CC-regime. The d_s-values, listed in the insert, refer to the FHH-regime at low pressures.

So called FHH-plots of the nitrogen adsorption isotherms at 77 K of various graphitized furnace blacks are shown in Fig. 9. The graphitized furnace blacks have two linear ranges. Starting from low pressures (right side), the first linear range is fitted by Equ. (3a), because the film is not very thick and the van der Waals attraction

of the molecules by the solid governs the adsorption process (FHH-regime). With rising pressure, at a critical film thickness of about $z_{crit.} \approx 0.5$ nm (Equ. (5)), the vapor-liquid surface tension γ becomes dominant and a step-like increase of the adsorbed amount is observed. The fractal FHH-theory claims fractal dimensions of $d_s \approx 2.3$ up to a length scale of $z \approx 1$ nm, independent of grade number. At this length scale a geometrical cut-off appears and the surface becomes rougher. In the final linear regime, corresponding to $z > 1$ nm, the surface fractal dimension takes the value $d_s \approx 2.6$ (CC-regime). This linear range has an upper cut off length of $z \approx 6$ nm.
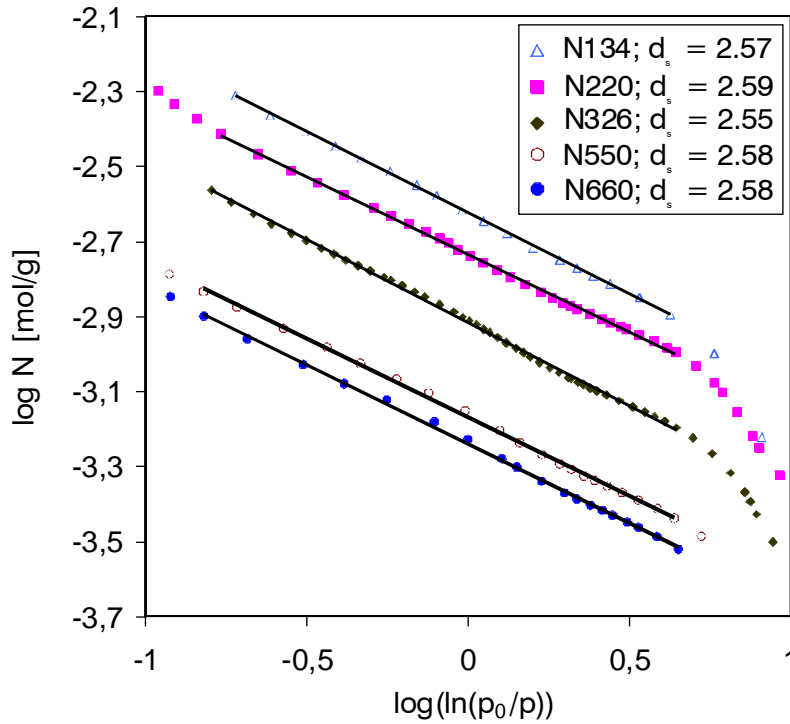

Fig. 10: FHH-plots of nitrogen adsorption isotherms at 77 K of various furnace blacks, as indicated. The surface fractal dimension appears to be universal, i. e. it varies between $d_s = 2.55$ and $d_s = 2.59$ for the depicted furnace blacks.

Fig. 10 shows that contrary to the graphitized blacks the untreated furnace blacks have only one linear range with a fractal dimension of $d_s \approx 2.6$ (CC-regime, Equ. (3b)). Obviously the van der Waals attraction can be neglected and the surface tension γ controls the adsorption process on all length scales. This is due to the larger surface fractal dimension d_s as compared to the graphitized furnace blacks that shifts the cross-over length $z_{crit.}$ to smaller values (Equ. (4)). Assuming that the number density n, the surface tension γ of the adsorbate and the van der Waals interaction parameter α are approximately the same for liquid nitrogen adsorbed on graphitized and untreated furnace blacks, a cross-over length of $z_{crit.} \approx 0{,}35$ nm can be estimated from Equ. (4) with the experimental values of the fractal dimensions and the crossover length $z_{crit.} \approx 0.5$ nm on a graphitized carbon black. The value

$z_{crit.} \approx 0,35$ nm is already in the range of the detection limit given by the layer thickness a ≈ 0.35 nm. Hence, the nitrogen adsorption on furnace carbon blacks is dominated by the vapor-liquid surface tension on all length scales and a cross-over between the FHH- and the CC-regime does not appear.

The results for the surface fractal dimension of a series of furnace blacks and graphitized blacks, obtained by nitrogen adsorption in the multilayer regime, are summarized in Fig. 11. The cut off lengths are quite similar within both series of blacks and agree with those found in Figs. 9 and 10. In Fig. 11 a weak trend of increasing surface fractal dimension with increasing specific surface (decreasing primary particle size) is observed. This results from increasing curvature of the particle surface with decreasing size, since crystallite structures with edges are present on the surface that lead to a more pronounced roughness, if arranged on a strongly curved surface. We will see in the next section that the amount of crystallite edges and slit shaped cavities increases slightly with increasing specific surface, leading to a more pronounced energetic surface activity for the fine carbon blacks. This relative small effect correlates well with the weak trend of the surface fractal dimension observed in Fig. 11.
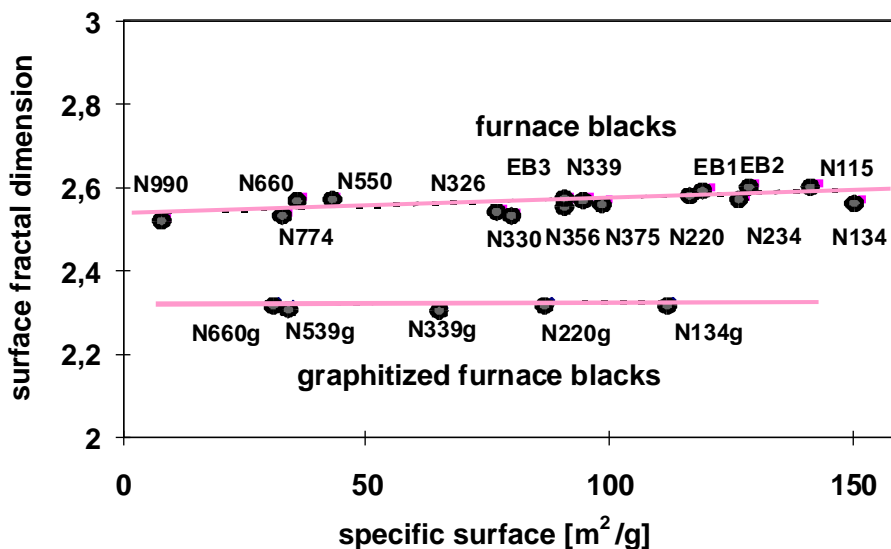
Fig. 11: Surface fractal dimensions d_s on atomic length scales of furnace blacks and graphitized blacks in dependence of specific surface. The data are obtained from nitrogen adsorption isotherms in the multilayer regime.

The observed almost universal value of the surface fractal dimension $d_s \approx 2.6$ of furnace blacks can be traced back to the conditions of disordered surface growth during carbon black processing. It compares very well to the results evaluated within the an-isotropic KPZ-model as well as numerical simulations of surface growth found for random deposition with surface relaxation. This is demonstrated in some detail in Appendix A.

3.1.2 Energy distribution of carbon black surfaces

The energy distribution f(Q) of carbon black surfaces is calculated by assuming that the measured overall isotherm consists of a sum of generalized Langmuir isotherms of various interaction energies Q, implying that the energy distribution can be identified with the numerically obtained weighting function [103,104]. For a continuous distribution function f(Q) the overall isotherm Θ(p,T) is given by:

$$\Theta(p,T) = \int_0^\infty \theta(p,T,Q) \cdot f(Q)\, dQ \qquad (6)$$

The integral in Equ. (6) is normalized to unity. This has to be taken into consideration if solid samples with different specific surface areas are compared.

For an evaluation of the local model isotherm θ(p,T,Q) with constant interaction energy Q, the effects of multi-layer adsorption and lateral interactions between neighboring adsorbed molecules are considered by applying two modifications to the Langmuir isotherm: (i) a multi-layer correction according to the well known BET-concept and (ii) a correction due to lateral interactions with neighboring gas molecules introduced by Fowler and Guggenheim (FG) [105]:

$$\theta(p,T,Q) = \frac{b_{BET}^2 \cdot b_{FG} \cdot b_L \cdot p}{1 + b_{BET} \cdot b_{FG} \cdot b_L \cdot p} \qquad (7)$$

with:

$$b_{BET} = \frac{1}{1 - \dfrac{p}{p_0}} \qquad (8)$$

$$b_{FG} = e^{\frac{z\omega\theta}{RT}} \qquad (9)$$

$$b_L = \frac{N_a \sigma \tau_0}{\sqrt{2\pi MRT}} \cdot e^{\frac{Q}{RT}} \qquad (10)$$

Here, z is the number of neighboring adsorption sites, ω is the contribution of the lateral interaction to Q and θ is the probability that the neighboring sites are

occupied by a gas molecule. R is the gas constant, T is temperature, τ_0 is Frenkel's characteristic adsorption time, σ is the adsorption cross-section of the gas molecules, N_a is Avogado's constant and M is the molar mass. Note that the probability that the neighbor sites are occupied with other gas molecules is taken to be the local surface coverage θ and not the overall surface coverage Θ. This means that sites with the same interaction energies Q are assumed to be arranged in patches, which is in accordance with the picture of graphite like micro crystallites on the surface of the carbon black particles [26]. A probability Θ stands for a random distribution of sites with Q.

By referring to adsorption isotherms of ethylene down to very low surface coverages (10^{-3} - 1 mono-layers), the energy distribution function of adsorption sites on different furnace blacks was estimated with Equs. (6) to (10) by applying a numerical iteration procedure introduced by Adamson et al. [103]. This is described in some detail in Refs. 20 and 79. For a test of the evaluation procedure, the resulting energy distribution functions obtained from four different isotherms (three different temperatures) of ethylene on N220 are compared in Fig. 12. It becomes obvious that the isotherms measured at different temperatures lead to the same result for the energy distribution function, approximately, confirming the applied procedure. An analysis of the energy distribution function of ethylene on N220 is shown in Fig. 13, where the distribution function is fitted to four different Gauss-functions.
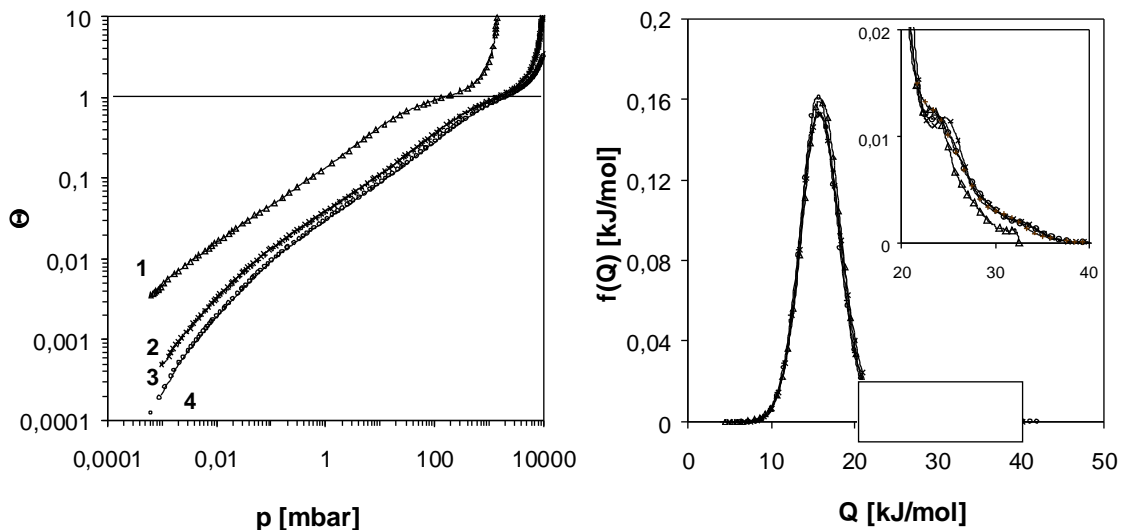

Fig. 12: Adsorption isotherms ($\Theta=N/N_m$) and corresponding energy distribution functions of ethylene on N220 at various temperatures; ((1) T=177 K; (2)(3) T=223 K; (4) T=233 K)
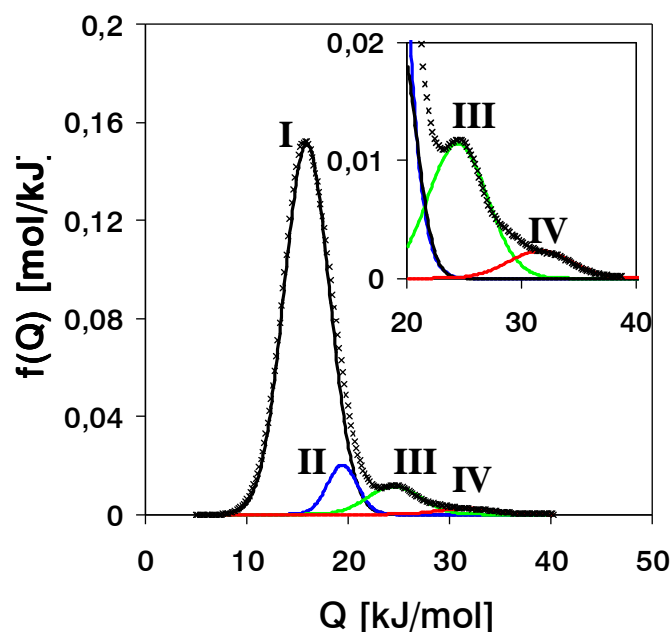
Fig. 13: Fitting of the energy distribution function of ethylene on N220, already shown in Fig. 12 (T = 223 K), to four Gaussian-peaks (I-IV).

Obviously, the good fit indicates that four different types of adsorption sites can be distinguished on the N220 surface. We relate the low energetic peak (I) to the basaltic layers and peak (III) to the edges of carbon crystallites. Peak (II) is referred to amorphous carbon and peak (IV) results from a few highly energetic slit like cavities between carbon crystallites. This is shown schematically in Fig. 14.

Fig. 14: Schematic view of the association between morphological arrangements of carbon crystallites and energetic characteristics of carbon black surfaces. Four different types of adsorption sites are distinguished that refer to the de-convolution shown in Fig. 13.

The attachment of peak (II) to the amorphous carbon is concluded from the observation that this peak does not appear in the case of the graphitized black N220g and graphitic powder. The corresponding isotherms and energy distribution functions are depicted in Fig. 15. A comparison to the above analyzed N220 and a strong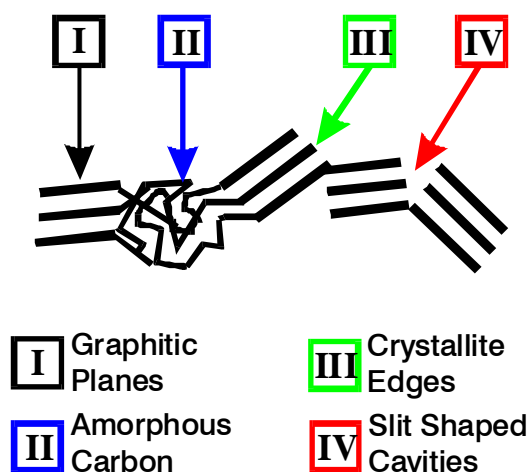ly reinforcing channel gas black demonstrates the relatively large amount of highly energetic sites of these blacks (Fig. 15).
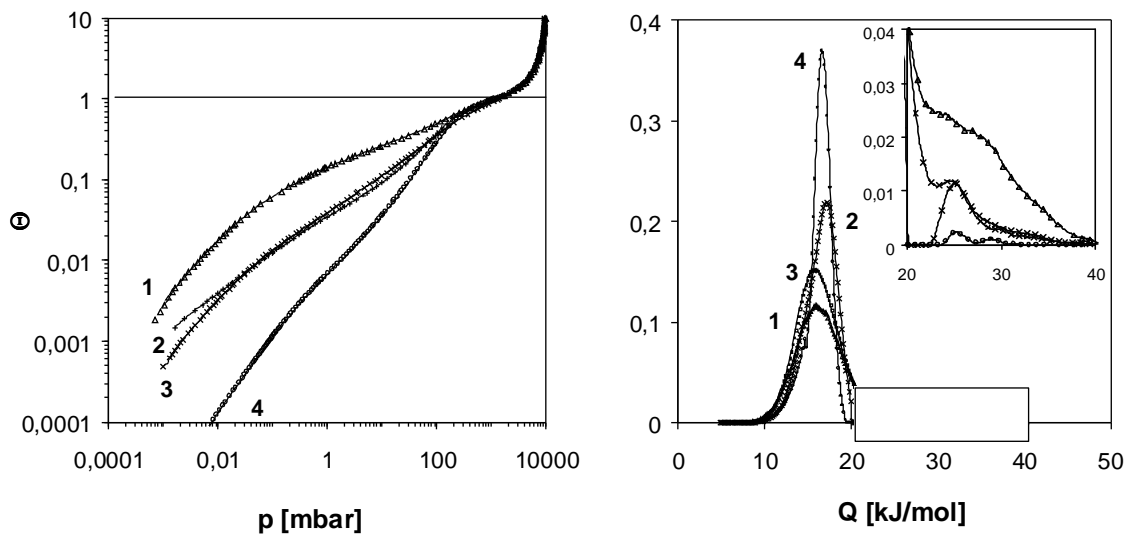
Fig. 15: Adsorption isotherms and evaluated energy distribution functions of ethylene on four different colloidal fillers at T=223 K; (1) channel gas black; (2) graphitic powder; (3) N220; (4) graphitized N220g.

A comparison of the adsorption isotherms and the resulting energy distribution functions of three different furnace blacks is shown in Fig. 16. Corresponding to the difference in level and shape of the isotherms the amount of highly energetic sites varies significantly. The black N115 has a large fraction of highly energetic sites, while the N550 shows a small fraction of highly energetic sites. The results of the peak analysis for the examined blacks and the graphitic powder are quantified in Table 2. A more detailed representation of energetic surface heterogeneity is found in Refs. 20, 79 and 82.

Summarizing we can conclude from the analysis of the surface energy distribution of carbon blacks that four different energetic sites can be distinguished. The fraction of highly energetic sites decreases significantly with grade number and disappear almost completely during graphitization. It indicates that the reinforcing potential of carbon black is closely related to the amount of highly energetic sites that can be well quantified by the applied gas adsorption technique. Theoretical

investigations on the effect of morphological as well as energetic surface roughness on the polymer-filler interaction strength confirm this finding [64,65,106,107]. The combination of two types of disorder, given by the pronounced morphological roughness (d_s=2.6) and the inhomogeneous energetic surface structure of carbon blacks, enhances the polymer filler coupling, significantly. It represents an important reinforcing mechanism on atomic length scales associated with the required strong phase binding in high performance elastomer composites.
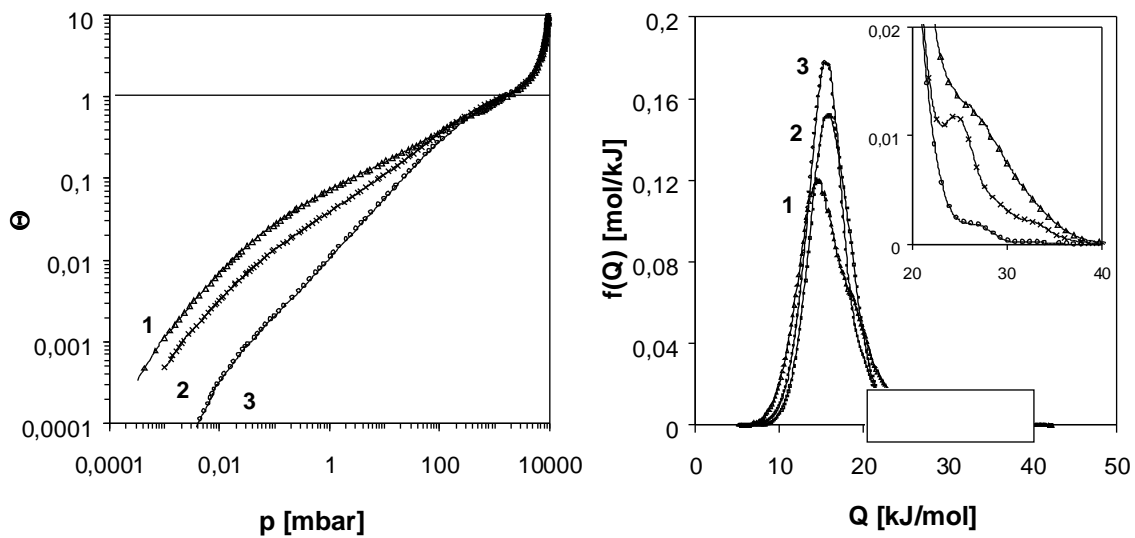
Fig. 16: Adsorption isotherms and evaluated energy distribution functions of ethylene on three different furnace blacks at T=223 K; (1) N115; (2) N220; (3) N550.

	I	II	III	IV
channel-gas-black	61	2	31	6
N115	69	13	15	3
N220	84	7	7	2
N550	93	6	1	< 1
graphitic powder	94	0	4	2
graphitized N220g	99	0	< 1	< 1

Tab. 2: Estimated fraction [%] of the four different types of energetic sites (I - IV) for adsorption of ethylene on various colloids.

3.2 Morphology of carbon black aggregates on nanoscales

Carbon blacks for the rubber industry are produced in a variety of classes and types, depending on the required performance of the final product. In general, they consist of a randomly ramified composition of primary particles that are bonded together by strong sinter bridges. Significant effects of the different grades of carbon blacks in elastomer composites result from variations in the specific surface and/or "structure" of the primary aggregates [26,27]. The specific surface depends strongly on the size of the primary particles and differs from about 10 m^2/g for the very coarse blacks up to almost 200 m^2/g for the fine blacks. The "structure" of the primary aggregates describes the amount of void volume and is measured e. g. by oil (DBP) absorption. It typically varies between 0.3 cm^3/g and 1.7 cm^3/g for furnace blacks.

The characteristic shape of carbon black aggregates is illustrated in Fig. 17, where transmission electron micro-graphs (TEM) of three different grades of furnace blacks (N220, N330, N550) are shown. The variation in size of the primary particles, increasing from top to bottom, becomes apparent. It implies a decline of the specific surface from 116 m^2/g for N220, 81 m^2/g for N330 up to 41 m^2/g for N550 (Tab.1).
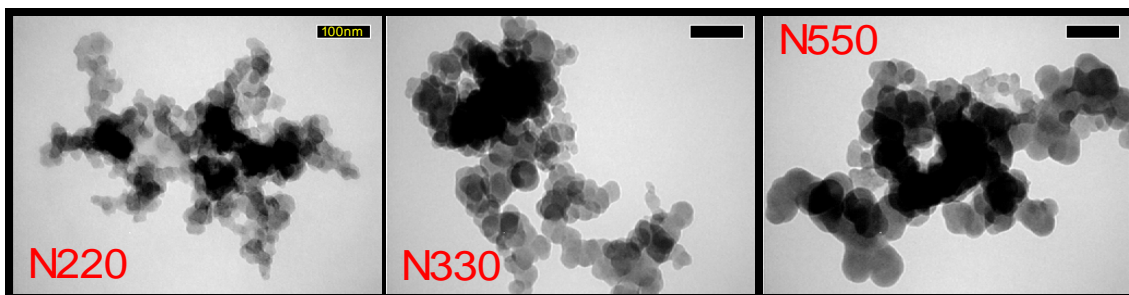
Fig. 17: Transmission electron micro-graphs (TEM) of three different grades of furnace blacks N220, N330 and N550 (dry state). (Bar length: 100 nm)

The "structure" or amount of specific voids of the three grades is almost the same and differs between 1 cm^3/g and 1.2 cm^3/g, only. Since the specific weight of carbon black is almost twice of that for DBP, this corresponds to a factor two for the void volume as compared to the solid volume of the aggregates. It means that about 2/3 of the aggregate volume is empty space, i. e. the solid fraction Φ_p of the primary aggregates is relative small ($\Phi_p \approx 0.33$). It is shown in Section 3.2 that Φ_p fulfills a scaling relation which involves the size and mass fractal dimension of the primary aggregates. Due to significant deviations of the solid fraction Φ_p from one, the filler volume fraction Φ of carbon black in rubber composites has to be treated as an effective one in most applications, i. e. $\Phi_{eff} = \Phi / \Phi_p$ (compare Appendix C).

3.2.1 Fractal analysis of primary carbon black aggregates

For a quantitative analysis of the structure of carbon blacks as shown in Fig. 17 it is useful to consider the solid volume V_p or the number of primary particles N_p per aggregate in dependence of aggregate size d. In the case of fractal objects one expects the scaling behavior [1,2]:

$$V_p \sim N_p \sim d^{\,d_f} \qquad (11)$$

The exponent d_f is denoted mass fractal dimension or simply fractal dimension. It characterizes the mass distribution in three dimensional space and can vary between $1 < d_f < 3$. This kind of fractal analysis of furnace blacks was performed e. g. by Herd et al. [108] or Gerspacher et al. [109,110]. The solid volume V_p of primary aggregates is normally determined (ASTM: 3849) from the cross-section area A and the perimeter P of the single carbon black aggregates by referring to a simple Euklidean relation[108]:

$$V_p = \frac{8\,A^2}{3\,P} \qquad (12)$$

However, it is not quite clear whether this relation can be applied for non-Euklidean, ramified structures. Simulation results of carbon black formation under ballistic conditions by Meakin et al. [14] indicate that a scaling equation is fulfilled, approximately, between the number of particles N_p in a primary aggregate and the relative cross section area A/A_p:

$$N_p = 1.51\,(A/A_p)^{1.08} \qquad (13)$$

Here, A_p is the cross section area of a single primary particle. Dependent on the application of Equ. (12) or (13), respectively, significantly different values for the mass fractal dimension are obtained.

This discrepancy is demonstrated in Figs. 18 and 19, by considering an example of a fractal analysis of primary carbon black aggregates. Fig. 18 shows a TEM-micro-graph of the furnace black N339 prepared from a ready mixed composite of S-SBR after removing of the unbounded polymer as explained in the experimental section (in-rubber state). A double logarithmic plot of the solid volume V_p and the particle number N_p, estimated from Equ. (12) and (13), vs. aggregate diameter d is shown in Figs. 19a and 19b, respectively. The aggregate average diameter d is estimated as the mean value from 16 measurements on a single aggregate with a

15% variation in the angle of rotation. The obtained fractal dimensions differ significantly for the two evaluation procedures. From the slope of the two regression lines one finds $d_f = 2.45$ and $d_f = 1.94$, respectively.
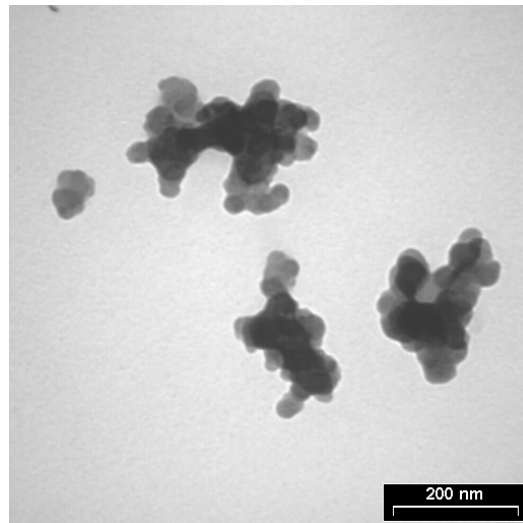

Fig.18: TEM-micro-graph of carbon black aggregates (N339) prepared from ready mixed S-SBR-composites with 60 phr filler (in-rubber state).
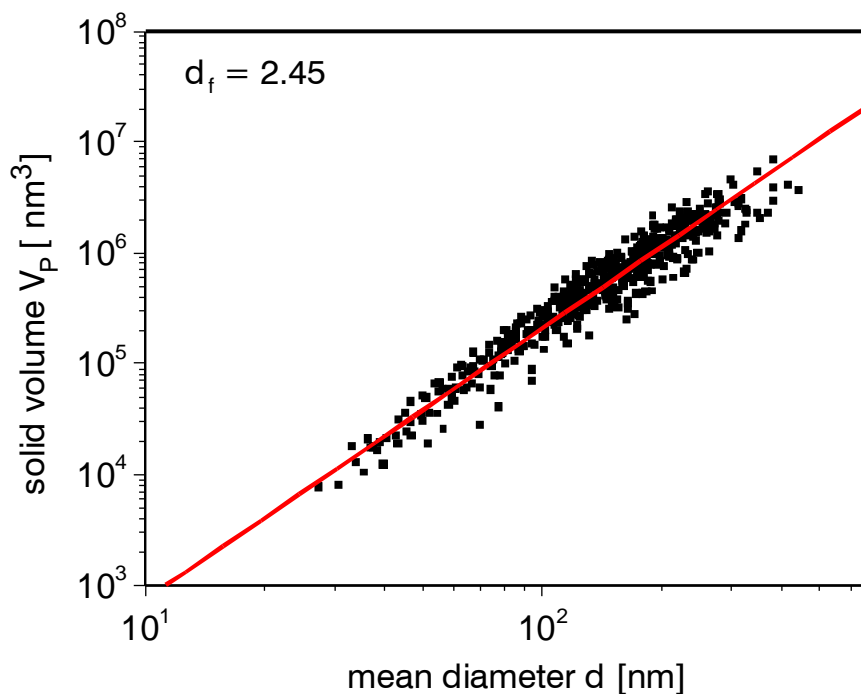

Fig. 19a: Fractal analysis according to Equ. (11) of primary carbon black aggregates (N339) prepared from S-SBR-composites with 60 phr filler (in-rubber state). V_p is evaluated from Equ. (12).
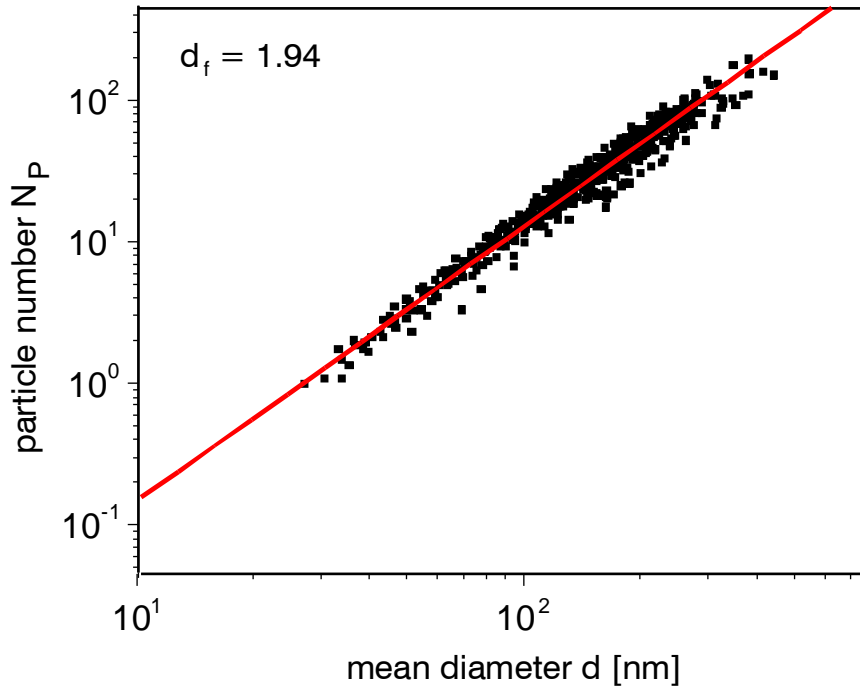
$d_f = 1.94$

particle number N_P

mean diameter d [nm]

Fig. 19b: Fractal analysis according to Equ. (11) of the same set of primary carbon black aggregates (N339) as shown in Fig. 19a. N_p is evaluated by using Equ. (13).

In view of a discussion of this discrepancy, we consider the conditions of primary aggregate growth during carbon black processing in some detail. Fig. 20 shows a schematic representation of carbon black formation in a furnace reactor, where a jet of gas and oil is combusted and quenched, afterwards. Beside the aggregate growth, resulting from the collision of neighboring aggregates, surface growth due to the deposition of carbon nuclei on the aggregates takes place during the formation of primary carbon black aggregates. The surface growth leads to the universal surface roughness, analyzed by gas adsorption technique in Section 3.1.1 and investigated from a theoretical point of view in Appendix A. Obviously, the surface growth is also responsible for the strength of the primary aggregates, since it proceeds in the contact range of the collided aggregates implying a strong bonding by sinter bridges (Fig. 20).

Due to the high temperature in the reactor, aggregate as well as surface growth take place under ballistic conditions, i. e. the mean free path length of both growth mechanisms is large compared to the characteristic size of the resulting structures [14-16]. Then the trajectories of colliding aggregates (or nuclei) can considered to be linear. Numerical simulations of ballistic cluster-cluster aggregation yield a mass fractal dimension $d_f \approx 1.9 - 1.95$ [11,12,17]. This compares to the above TEM-result $d_f \approx 1.94$ evaluated with Equ. (13). It means that the assumption of ballistic cluster-cluster aggregation during carbon black processing, used already in

the derivation of Equ. (13), is confirmed by the TEM-data of the relatively fine black N339. For the more coarse blacks, with a typically small primary particle number, finite size effects can lead to a more compact morphology that differs from the scaling prediction of ballistic cluster aggregation. A further deviation can result from electrostatic repulsion effects due to the application of processing agents (alkali metal ions) for designing the coarse blacks (compare Appendix C). Note that a similar relation as Equ. (13) was derived in the 60th by Medalia and Heckman [111,112]. The value $d_f = 1.94$ also agrees fairly well with other estimates obtained e. g. by electric force microscopy [113], TEM [114] or SAXS [95,96].

Therefore, it appears likely that the approach considering the solid volume of primary aggregates, as evaluated from the two dimensional cross-section area by Equ. (12), leads to an overestimation of the mass fractal dimension. A more realistic estimate is obtained with Equ. (13). By referring to Equ. (12), the data obtained by Herd et al. [108] show a successively increasing value of the mass fractal dimension from $d_f \approx 2.3$ to $d_f \approx 2.8$ with increasing grade number (or particle size) of the furnace blacks. As expected, they fit quite well to the above estimate $d_f \approx 2.45$ for the black N339. A summary of these data and a discussion including other fractal parameters is found in Appendix C.
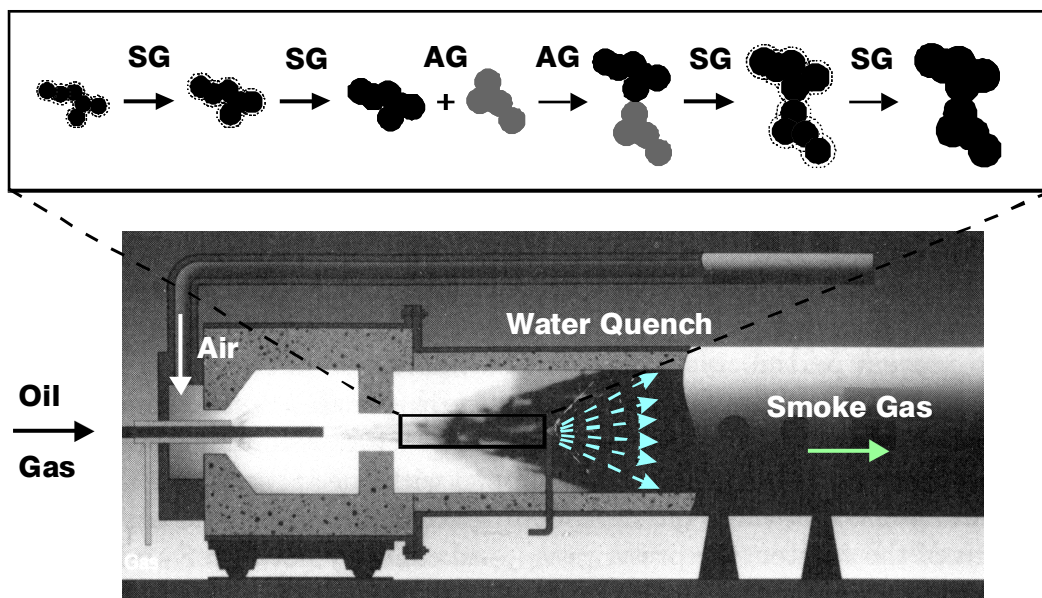

Fig. 20: Schematic view of carbon black processing in a furnace reactor. Primary aggregates are built by two simultaneous growth processes: (i) surface growth (SG) and (ii) aggregate growth (AG).

35

3.2.2 Effect of mixing on in-rubber morphology of primary aggregates

It is well established that the specific properties of carbon black filled elastomers, e. g. viscoelasticity or electrical conductivity, are strongly affected by the disordered, ramified structure of the primary aggregates [26,27]. On the one side, this structure is characterized by the mass fractal dimension considered above. On the other side, it is determined by a lower and upper cut-off length, i. e. primary particle size and aggregate size, respectively. In the following we will focus on the upper cut-off length or, more precisely, on the size distribution of primary aggregates in ready mixed composites. We will see that this quantity depends on the conditions of sample preparation, since aggregate rupture can take place if high shear stresses are applied during the mixing procedure.

In the literature it has been found that during mixing aggregate breakdown occurs for a number of carbon blacks in highly viscous rubbers [115-118]. Recently, the aggregate breakdown was also attributed to classes of specific shapes of individual carbon blacks [108]. The opinion about the mechanical consequences of this process are quite different. On the one side, no obvious relationship to reinforcement is conjectured [116]. On the other side, improvements of the mechanical performance, due to the creation of new, active carbon surface, is assumed, which participates in formation of a strong filler-rubber coupling [118].
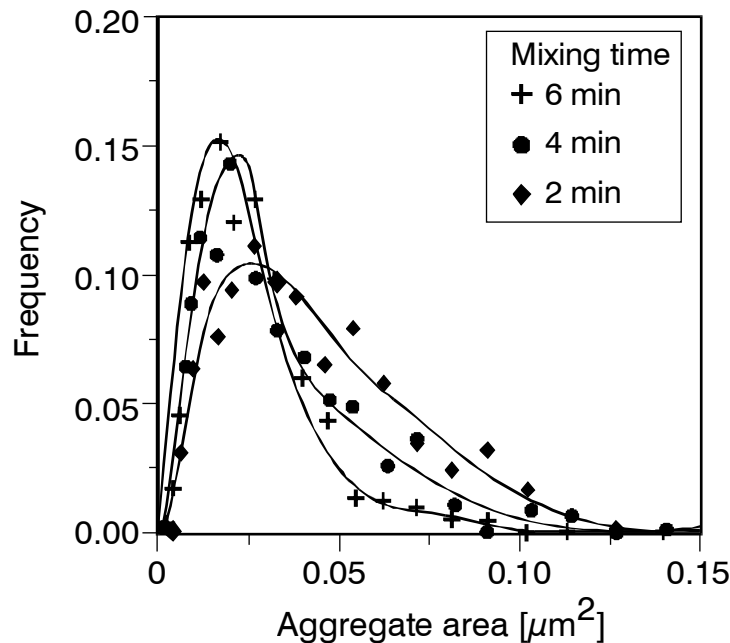

Fig. 21: Aggregate size distribution obtained from TEM-analysis (in-rubber state) of E-SBR-samples filled with 50 phr N330 at various mixing times, as indicated [115].

Fig. 21 shows results obtained from TEM-analysis of primary aggregate size distribution of E-SBR/N330-samples at various mixing levels. With increasing mixing time, a shift in aggregate size distribution to smaller values is observed. The maximum of the distribution of aggregate cross section area shifts from about 0.03 μm^2 to about 0.02 μm^2. The shift of the maximum can be related to a breakdown of aggregates into smaller pieces as mixing time increases. It can also be referred to an improved micro-dispersion with specific influences on the mechanical property spectrum [85]. A characteristic effect of increasing mixing time on aggregate size is the reduction in the shoulder, occurring in the case of aggregate cross section areas greater than 0.05 to 0.15 μm^2, in favor of smaller aggregates. This is indicative for the rupture of single aggregates into two pieces.

The observed aggregate breakdown during mixing can be understood on a more fundamental level, if the above discussed two simultaneous growth mechanisms, surface- and aggregate growth, during carbon black processing are considered, again (Fig. 20). Obviously, the surface growth implies a strong bonding between adjacent primary particles by rigid sinter bridges that keep the primary aggregates together. However, this process goes on during the aggregate growth leading to a hierarchy of bonding strengths: The bonds formed in the beginning of aggregate growth become stronger than the final ones, because the time for stabilization by sinter bridges decreases with increasing time in the reaction zone. The bonds formed between collided aggregates just at the end of the reaction zone, before the quenching process takes place, remain relatively weak. This becomes also apparent in the upper scheme of Fig. 20.

For that reason we expect that increasing mixing severity during compounding with highly viscous polymer melts leads to aggregate breakdown and changes in aggregate size distributions. According to Fig. 22, this is also observed for an increased filler loading.
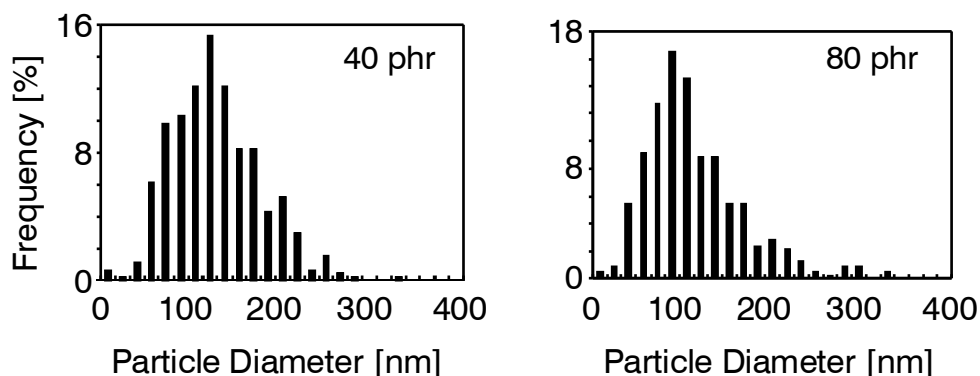

Fig. 22: Aggregate size distribution obtained from TEM-analysis (in-rubber state) of E-SBR-samples filled with 40 and 80 phr N339, respectively, at fixed mixing time of 4 minutes.

As shown in Fig. 22, the maximum of the size distribution is shifted to smaller values with rising filler concentration from 40 phr N339 to 80 phr N339 in E-SBR-composites. This results from the increased viscosity, since shear forces during mixing are enhanced with rising viscosity of the composite. A comparison of the morphology of N339 in E-SBR- and S-SBR-composites with increasing carbon black concentration is summarized in Table 3. It emphasizes the successive decrease of the mean primary aggregate size with increasing filler loading for both systems. The composites with E-SBR have a slightly larger aggregate size in the range of higher filler concentrations compared to those with S-SBR. On the one side, this can assumed to result from a lower viscosity, especially under elongation deformations, which is of high relevance for filler dispersion during mixing. On the other side, it may also be related to a weaker polymer-filler coupling between the carbon black surface and the E-SBR-chains [119].

N339 [phr]	$<A>$ [nm^2]	$<P>$ [nm]	$<V_P>$ [nm^3]
E-SBR			
20	21,600	777	1,750,230
40	14,570	600	1,009,400
60	12,090	534	838,779
80	12,170	516	780,592
S-SBR			
20	22,900	857	1,711,680
40	15,820	639	1,113,475
60	12,580	539	839,255
80	8,060	399	482,050

Tab. 3: Characteristic parameters from TEM-analysis for primary aggregates of N339 in E-SBR- and S-SBR-composites, respectively, at various filler concentrations and fixed mixing time (4 minutes). $<A>$: mean cross section area; $<P>$: mean perimeter; $<V_p>$: mean solid volume (Equ. (12))

The observed effect of mixing on aggregate size distribution has a pronounced influence on the mechanical properties of the composites. This can be quantified by considering the solid fraction Φ_p of primary aggregates that represents a measure for the "structure" of carbon blacks. It is given by the ratio between the solid volume and the overall aggregate volume. Then, with Equ. (11) one find the following scaling relation with respect to the average diameter d of the aggregates:

$$\Phi_p = \frac{V_p}{\frac{\pi}{6} d^3} \sim d^{\,d_f - 3} \tag{14}$$

A fractal analysis according to Equ. (14) of carbon black aggregates (N339) in ready mixed E-SBR-composites is depicted in Fig. 23. The predicted scaling behavior of the aggregate solid fraction with diameter can be observed, though there is a larger scattering of the data as compared to those in Fig. 19. The slope of the solid regression line yields $d_f \approx 2.33$. Note that this differs significantly from the above estimate (Fig. 19a), which is mainly due to the different averaging procedures: An analysis of the solid fraction Φ_P, calculated according to Equ. (14), indicates that for a constant aggregate diameter d there is a distribution of Φ_P as well as for a constant Φ_P there is a scatter of the average diameter. The limiting value of the solid fraction $\Phi_p = 1$, corresponding to spherical particles, fits very well to the size of the primary particles of the carbon black N339 given by about 30 nm (dashed lines).
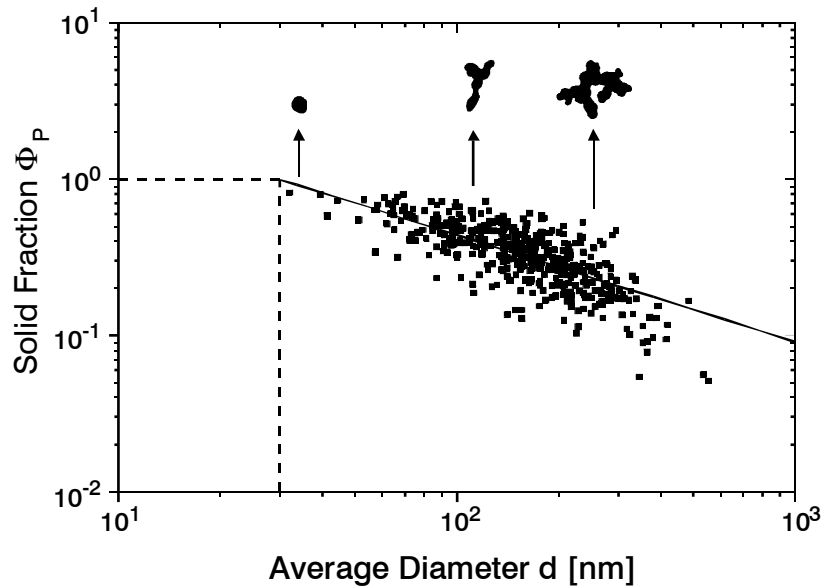
Fig. 23: Fractal analysis according to Equ. (14) of primary carbon black aggregates (N339) prepared from E-SBR-composites with 60 phr filler (in-rubber state). V_p is evaluated from Equ. (12).

As argued above, aggregates are efficiently diminished in size and partly broken due to the higher shear forces with increasing carbon black loading. This is emphasized in Fig. 24 by the increasing value of the mean solid fraction $<\Phi_P>$ as the carbon black loading changes from 0.1 to 0.3 volume fraction. The different extent of aggregate breakdown in E-SBR- and S-SBR composites, summarized in Tab. 3, becomes again apparent. It is indicated by the two regression lines that show a slightly steeper increase in the case of S-SBR-composites (dashed line).
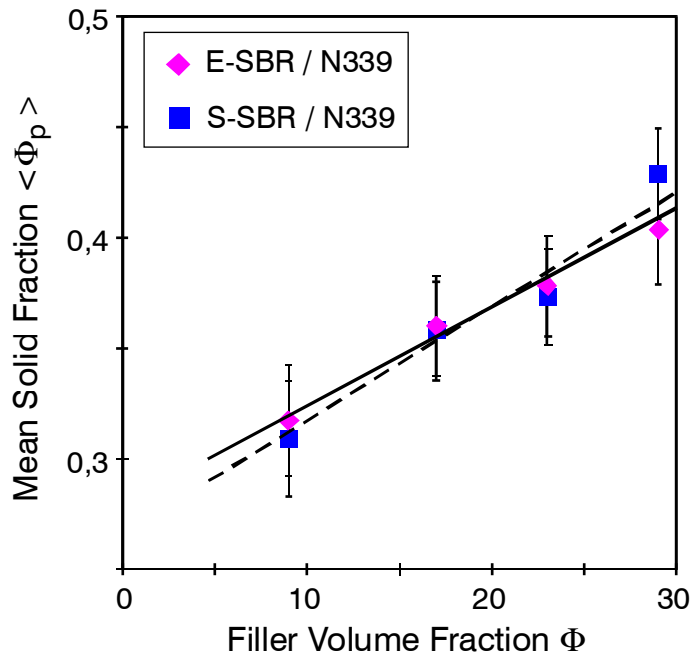
Fig. 24: Mean aggregate solid fraction vs. filler volume fraction of N339 in E-SBR-
and S-SBR-composites, respectively, as obtained from TEM-analysis (in-
rubber state).

A technologically important advantage of a high primary aggregate "structure"
(low solid fraction) is the improved dispersion behavior of the "high structure" blacks
[26,119]. In particular, the very fine blacks can hardly be dispersed by mechanical
mixing due to the large number of attractive contacts between adjacent primary
aggregates in a more or less close packing before mixing, e. g. in the pelletized
state. With increasing "structure" (decreasing solid fraction), the number of attractive
contacts per unit volume decreases and the force, necessary to separate the
aggregates in a pellet, is reduced. In comparison, for the coarse blacks the number
density of contacts between neighboring aggregates in a pellet is relatively small
and therefore also "low structure" grades are quite easily dispersed.

Summarizing we conclude that the primary aggregate "structure" can be well
analyzed by TEM-techniques. It is readily described by a fractal approach that refers
to a cluster-cluster aggregation mechanism of primary particles during carbon black
processing. During compounding of carbon blacks with highly viscous rubbers,
rupture of primary aggregates takes place depending on the mixing severity. This
leads to a reduced aggregate size and an increased solid fraction with increasing
mixing time or filler loading, which has a significant influence on the mechanical
properties of the composites. This will be considered in a micro-mechanical model
of rubber reinforcement in Section 5.

4. Carbon black networking on mesoscopic length scales

4.1 Microscopic and scattering analysis

A key factor for a deeper understanding of structure-property relationships of high performance elastomers is the morphological arrangement of filler particles on mesoscopic length scales due to secondary aggregation, also referred to as filler flocculation, cluster formation or networking. Even though the presence of such secondary network structures is often used in discussing filler specific mechanisms as the Payne effect, its morphology, as depicted in Fig. 25, is rarely studied on a quantitative level in comparison to that of the primary aggregates.
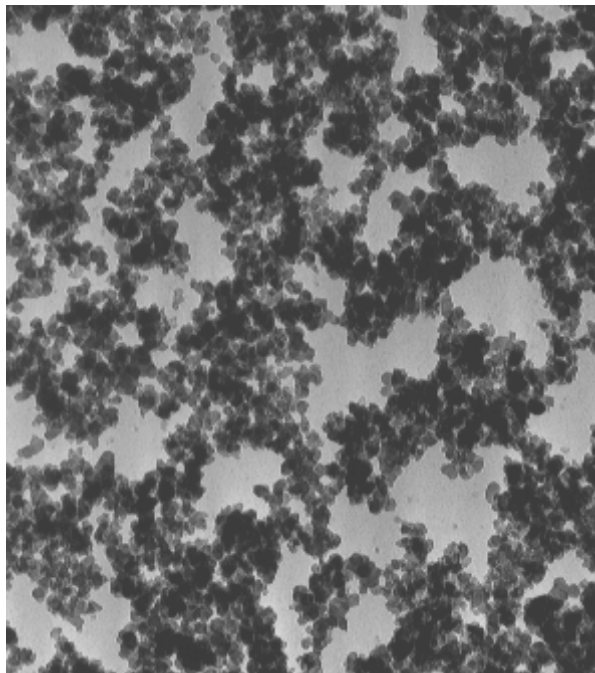
Fig. 25: TEM-micro-graph of a carbon black network obtained from an ultra-thin cut of a filled rubber sample.

In particular, the morphology of secondary filler networks is of high relevance for micro-mechanical models of rubber reinforcement, involving the original relaxed network structure as well as its stress-induced breakdown during deformations. Such models have been developed by assuming e. g. a percolation structure for the filler network [56] with a characteristic mass fractal dimension $d_f = 2.5$ [6,7]. Investigations of carbon black network structure in polyethylene (HDPE) by electric force microscopy seem to confirm this value, approximately, delivering $d_f = 2.6$ on length scales between 0.8 and 2 μm [113]. However, recent studies of carbon black (N330) network structure in rubber (EPDM) by scanning electron microscopy found

significantly smaller values for the mass fractal dimension in the intermediate length scale range between about 200 nm and 2 μm, increasing from $d_f = 1.9$ to $d_f = 2.4$ with increasing filler concentration [120]. The variation of the fractal dimension was referred to a spatial inter-penetration of spanning cluster arms in three-dimensional space that does not allow for a proper estimation of d_f. The value $d_f = 1.9$ for low filler concentrations was conjectured to lie close to the characteristic value $d_f = 1.8$ expected for cluster-cluster aggregation (CCA) [6,7]. The CCA-morphology has been considered by Witten et al. in modeling the quasi-static stress-strain behavior of filler reinforced rubbers [21]. Furthermore, based on the assumption of a CCA-filler network, the scaling behavior of the small strain elastic modulus with filler concentration could be well described [22,23,48,85], though there is no unique experimental evidence for this particulate morphology (see below).

So far, also scattering techniques fail to provide reliable information on the connectivity of the filler network on larger length scales. This is again due to the spatial inter-penetration of the filler network in three-dimensional space, since labeling techniques, as considered e. g. for polymer networks, can not be applied. SAXS-studies on carbon black (N330) filled polyethylene have demonstrated that inter-penetration of primary aggregates in dense pellets causes the fractal domain to vanish due to a loss of correlation between primary particles [95]. A well defined scaling behavior of the scattering curves could only be obtained if a vanishing inter-penetration of neighboring aggregates was insured, i. e. spatially well separated aggregates, obtained from de-pelletized or fluffy black at sufficiently low filler concentrations, were realized. The same effect of inter-cluster correlation causes difficulties in obtaining information on the structure and connectivity of filler networks in elastomers, since inter-penetration can not be avoided. This is also obvious in the TEM-micro-graph shown in Fig. 25, where the three-dimensional, inter-penetrating connectivity of the carbon black network structure becomes apparent.

4.2   Investigations of electrical properties

4.2.1 Percolation behavior of the dc-conductivity

An important tool for analyzing the structure of carbon black networks in elastomers is provided by investigations of the electrical percolation behavior and the dielectric properties in a broad frequency range [22,23,121-139]. This is evident from the fact that, in an isolating polymer matrix, the charge carriers follow the conducting paths given by the connectivity of the filler network. In particular, the electrical percolation threshold decreases with increasing specific surface and/or "structure" of carbon black primary aggregates and decreasing compatibility between polymer and filler [121-125]. This emphasizes the role of mean aggregate

distance or gap size between primary aggregates or clusters. It refers to a thermally activated hopping or tunneling of charge carriers across the gaps that governs the conductivity of carbon black filled polymers above the percolation threshold. The non-universal value of the percolation exponent of the dc-conductivity gives a further hint on the role of charge carrier tunneling in the conduction mechanism of filled polymer composites [126,127].

The electrical percolation behavior for a series of carbon black filled rubbers is depicted in Figs. 26 and 27. The inserted solid lines are least square fits to the predicted critical behavior of percolation theory, where only the filled symbols are considered that are assumed to lie above the percolation threshold. According to percolation theory, the dc-conductivity σ_{dc} increases with the net concentration $\Phi-\Phi_c$ of carbon black according to a power law [6,128]:

$$\sigma_{dc} = \sigma_o \left(\frac{\Phi - \Phi_c}{1 - \Phi_c} \right)^{\mu} \qquad \text{for } \Phi > \Phi_c \qquad (15)$$

The critical concentration Φ_c denotes the percolation threshold, σ_o is the limiting dc-conductivity for $\Phi=1$ and the exponent μ is called percolation exponent. As outlined in Appendix D, percolation theory predicts an universal value $\mu \approx 2$ for all types of 3d-lattices. However, the fitted lines in Figs. 26 and 27 yield a non-universal behavior of μ, i. e. significantly larger values that depend on the carbon black grade and on the type of rubber. This is apparent from the data shown in Table 4, where the fitting parameters Φ_c, μ and σ_0 are listed together with the correlation coefficients r^2 for all sample series. Obviously, there is a clear trend that the critical concentration Φ_c as well as the percolation exponent μ increase with increasing grade number of carbon black, and, apart from the very coarse blacks, the limiting conductivity σ_o decreases. Furthermore, these parameters are found to be highly affected by the microstructure of the rubber matrix.

This behavior can be understood, if a superimposed kinetic aggregation process of primary carbon black aggregates in the rubber matrix is considered that alters the local structure of the percolation network. A corresponding model for the percolation behavior of carbon black filled rubbers that includes kinetic aggregation effects is developed in Appendix C, where the filler concentrations Φ and Φ_c are replaced by effective concentrations. In a simplified approach, not considering dispersion effects, the effective filler concentration is given by:

$$\Phi_{eff} = \frac{\Phi}{\Phi_p} \left\{ 1 + \beta \left(\frac{\Phi - \Phi^+}{\Phi_p} \right)^{B} \right\} \qquad (16)$$

Fig. 26: DC-conductivity vs. carbon black volume fraction of E-SBR samples filled with various furnace blacks. The solid lines are least square fits according to Equ. (15). Experimental data are taken from Ref. 124.
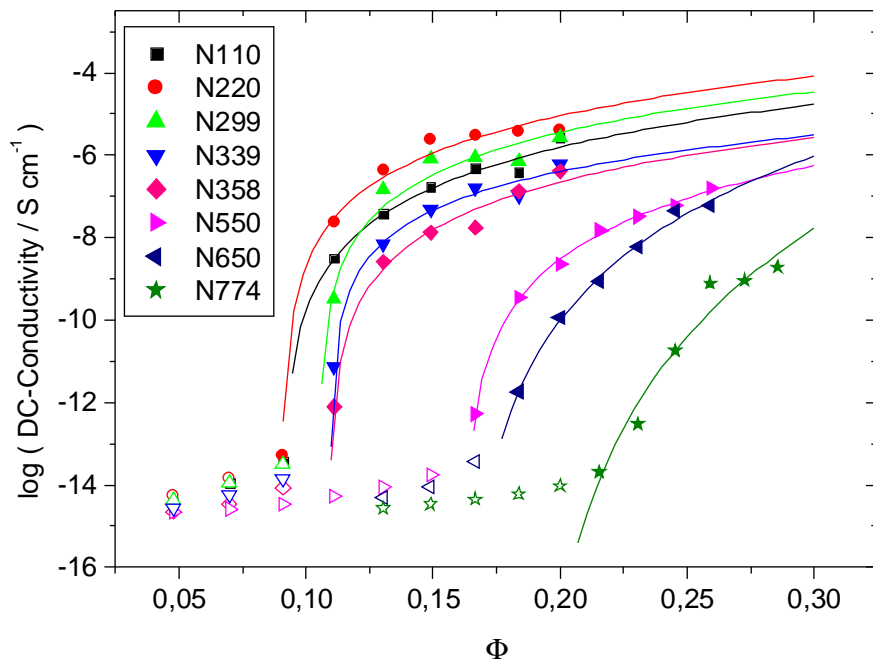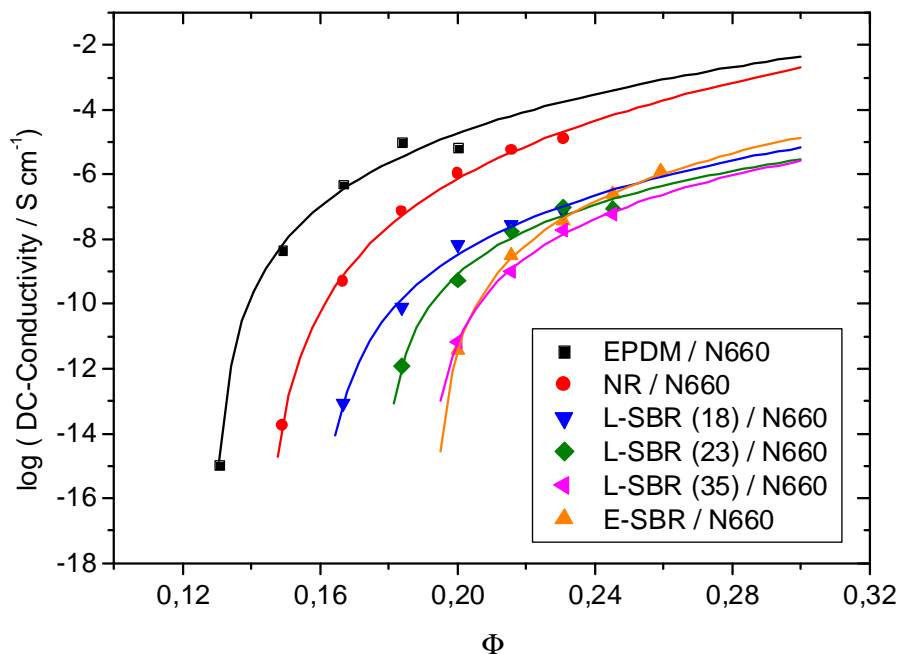

Fig. 27: DC-conductivity vs. carbon black volume fraction of various rubber samples filled with the furnace black N660. The solid lines are least square fits according to Equ. (15). Experimental data are taken from Ref. 124.

Sample Series	N_2SA [m^2/g]	Φ_P(CDBP)	Φ_c	μ	σ_o [S/cm]	r^2
E-SBR/N110	138	0.36	0.091	3.7	$3.9 \cdot 10^{-3}$	0.966
E-SBR/N220	116	0.36	0.090	3.4	$1.3 \cdot 10^{-2}$	0.920
E-SBR/N299	106	0.35	0.105	3.2	$4.2 \cdot 10^{-3}$	0.938
E-SBR/N339	95	0.35	0.110	2.7	$2.0 \cdot 10^{-4}$	0.989
E-SBR/N358	85	0.34	0.109	3.4	$4.8 \cdot 10^{-4}$	0.985
E-SBR/N550	41	0.41	0.162	4.0	$8.0 \cdot 10^{-4}$	0.998
E-SBR/N650	38	0.40	0.162	7.1	0.36	0.994
E-SBR/N774	29	0.45	0.185	10.6	17.2	0.960
EPDM/N660	36	0.43	0.129	6.3	122	0.994
NR/N660	36	0.43	0.143	7.8	1078	0.998
L-SBR(18)/N660	36	0.43	0.159	6.2	0.43	0.992
L-SBR(23)/N660	36	0.43	0.178	4.6	0.026	0.986
L-SBR(35)/N660	36	0.43	0.191	5.2	0.093	0.997
E-SBR/N660	36	0.43	0.193	5.5	1.02	0.999

Tab. 4: Fitting parameters of Equ. (10) for the data shown in Figs. 26 and 27. (N_2SA: Nitrogen surface area; Φ_P(CDBP): Primary aggregate solid fraction from CDBP-absorption with data from Ref. 26)

In Equ. (16), Φ_P is the solid fraction of the primary aggregates, which takes into account that carbon blacks are "structured" (compare Section 3.2.). Φ^+ is a critical concentration (aggregation limit), where secondary aggregation starts and β and B are characteristic growth exponents of secondary aggregation. These three parameters are governed by the mean primary aggregate distance and their mobility in the rubber matrix, i. e. they depend on the specific surface and "structure" of carbon black grade and on the type of rubber. In particular, it is demonstrated in Appendix C that the cluster growth function Equ. (16) allows for a quantitative description of the dependence of the Young modulus on filler concentration in the case of spherical, mono-disperse model fillers (micro-gels). In Appendix E it is demonstrated that the ability of secondary aggregation of filler particles in highly viscous polymers is reduced with increasing polymer-filler interaction. The same effect is described in the literature for the case of surface modified as well as graphitized carbon blacks [61,129,130].

The consideration of kinetic aggregation of "structured" filler particles by an effective filler concentration Φ_{eff}, as given by Equ. (16), instead of Φ and Φ_c in the percolation model Equ. (15), allows for a consistent interpretation of the observed

variation of fitting parameters listed in Tab. 4. A first effect on Φ_c results from the "structure", as described by Φ_P, that generally tends to larger values for the coarse blacks with large grade number. Since TEM-data for Φ_P, shown e. g. in Figs. 23 and 24, are not available for all sample series, the values $\Phi_P(CDBP) = (1 + \rho_{CB} \, CDBP/100)^{-1}$ are inserted in Tab. 4. They are given by the amount of di-butylphtalat absorption per 100 gram of carbon black after mechanical treatment (compressed DBP number (CDBP) according to ASTM D3493-90) and the mass density $\rho_{CB} = 1.8$ g/cm^3 of carbon black. Obviously, a single factor, e. g. the numerically estimated value of the percolation threshold in a simple cubic lattice, $\Phi_{c,eff} \approx 0.31$ [6], gives no correlation between $\Phi_P(CDBP)$ and the experimental values of Φ_c, indicating that the external bracket term of Equ. (16) differs from one. It means that the power law term, considering kinetic aggregation, must be significant. Accordingly, the percolation threshold Φ_c increases with increasing grade number mainly due to the restriction of mobility with decreasing specific surface of the primary aggregates.

The impact of rubber type on Φ_c (Fig. 27) can also be related to the variation of particle mobility, since a strong polymer-filler coupling in a more compatible polymer matrix reduces the particle mobility. Accordingly, beside the effect of "structure" considered by $\Phi_P(CDBP)$, the enhanced polymer-filler interaction in the series from EPDM via NR to the SBRs [124] as well as the decreasing specific surface area (N$_2$SA) with rising carbon black grade number lead to an increase of the percolation threshold Φ_c, since both effects hinder the kinetic aggregation process. A reduced aggregation corresponds to higher values of the growth exponent B in Equ. (16), which can be related to the increase of the percolation exponent μ with increasing grade number observed in Tab. 4. This is realized on a qualitative level, when the percolation Equ. (15) is rewritten with effective volume fractions by referring to Equ. (16). Then, for sufficient large filler concentrations the one in the external bracket term of Equ. (16) can be neglected. If furthermore Φ^+ is approximated by Φ_c, one obtains a simple scaling equation for the conductivity with respect to the net concentration $\Phi-\Phi_c$ with an effective exponent $\mu(B+1)$ that can be significantly larger than μ. This explains the non-universal value of the conductivity exponent that increases with the cluster growth exponent B.

Consequently, the consideration of a superimposed kinetic aggregation in the framework of percolation theory allows for a qualitative understanding of the variation of Φ_c and μ for the different sample series. We finally note that for a proper quantitative description of the percolation behavior of carbon black composites it is also necessary to consider the effect of primary aggregate breakdown more closely, i. e. the dependence of Φ_P on filler concentration and mixing conditions entering Equ. (16) (compare Section 3.2.2). This is beyond the scope of the present work. A quantitative description of percolation including a full characterization of in-rubber morphology of primary carbon black aggregates will be a task of future work.

4.2.2 Dielectric analysis of carbon black networks

The dielectric properties of carbon black filled rubbers are closely related to the morphological structure of filler networks, providing an important analysis tool on mesoscopic length scales. On the one side, the tunneling or hopping of charge carriers over conductive gaps provide information on the specific morphology of filler-filler bonds on nanoscopic length scales [121,122,131-134]. On the other side, the scaling behavior of the conductivity in the high frequency regime is indicative for anomalous diffusion of charge carriers on fractal carbon black clusters on mesoscopic length scales [23,134-139]. In the following, both of these effects will be analyzed by referring to exemplary results.

Fig. 28 shows the real part of the ac-conductivity σ' of a highly filled NR/N339 sample in the frequency- and temperature range 10^{-1} to 10^7 Hz and -100 to 150 °C, respectively. At low frequencies, below around 10^5 Hz, the conductivity is almost independent of frequency but show a pronounced temperature dependence. At high frequencies, a relaxation transition is observed leading to a step-like increase of the conductivity. In the low frequency regime, the conductivity first decreases slightly with increasing temperature, when the glass transition temperature, $T_g \approx$ -60 °C, is exceeded. This can be related to an enhanced thermal expansion of the rubber above T_g. It increases the size of conducting gaps between adjacent, highly conducting carbon black aggregates somewhat, implying that the gap size is the dominating factor for the conductivity. Since no thermal activation of the conductivity is observed at low temperatures, the conduction mechanism can concluded to be due to tunneling across gaps. Consequently, the gap size is of order 1 nm, i. e. the typical tunnel distance of quantum particles [121,122]. It can be related to the presence of a thin polymer film in the contact area between flocculated primary carbon black aggregates.

With rising temperature, above around 0 °C, the conductivity shown in Fig. 28 increases significantly. A closer analysis indicates a characteristic Arrhenius behavior in the temperature regime between 20 °C to 60 °C. Recently, such behavior has also been observed for other carbon black filled elastomers [133]. Obviously, the conduction mechanism in this temperature regime changes, implying a thermally activated hopping of charge carriers across the gaps between adjacent carbon black aggregates [121,122]. For temperatures larger than about 60 °C the conductivity levels out. This can be related to the impact of an increasing gap size on the conductivity, i. e. the strong exponential decrease of the conductivity with increasing gap size due to a more pronounced thermal expansion. Investigations of highly filled composites with various rubbers show that a qualitative similar behavior of the temperature dependence of the conductivity as in Fig. 28 is realized, but the temperature where the conductivity levels out seems to be roughly correlated with

the glass transition temperature of the polymer. In particular, for BR-composites with a relatively low glass transition temperature, the conductivity levels out around room temperature and shows a pronounced drop by orders of magnitude at higher temperatures. For these systems a conductor-isolator transition is observed at about 130 °C, which must be related to a strong increase of the gaps beyond a distance where hopping or tunneling of charge carriers can take place.
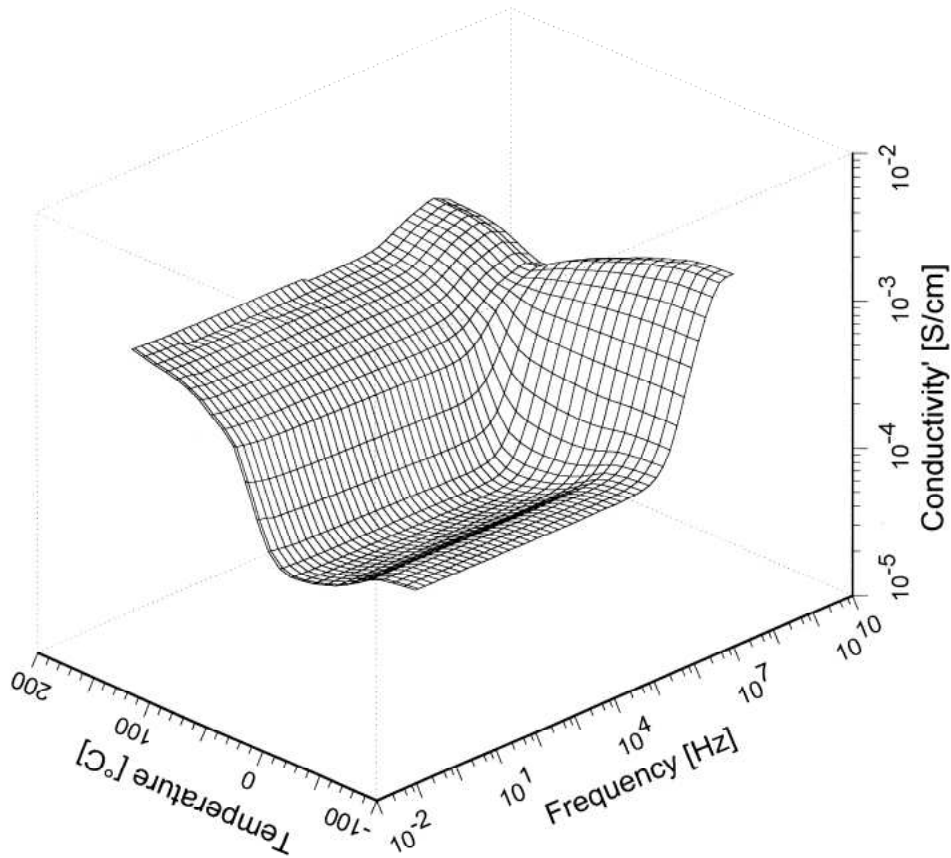
Fig. 28: AC-conductivity σ' vs. frequency and temperature of a NR-sample filled with 80 phr carbon black (N339).

For a deeper understanding of structure-property relationships it is useful to consider the effect of carbon black grade and concentration as well as polymer type on the dielectric properties more closely. In Fig. 29 the real part of the ac-conductivity σ' at 20 °C of a series of rubber composites, consisting of the more polar statistical co-polymer NBR and the fine black N220, is depicted for various filler concentrations in the high frequency regime up to 1 GHz. For the lower carbon black concentrations, a power law behavior with exponent around 0.6 is observed, while the highly filled composite exhibits a cross-over from a plateau value to a power law behavior. Obviously, the characteristic cross-over frequency increases with rising filler concentration.

This behavior becomes more transparent in Figs. 30a and 30b, where the ac-conductivity σ' and relative dielectric constant (permittivity ε'), respectively, for a series of less polar S-SBR-samples filled with various amounts of the coarse black N550 are show at 20 °C in a broader frequency range up to 10^7 Hz. For filler concentrations below the percolation threshold ($\Phi \leq 0.15$), the conductivity behaves essentially as that of an isolator and increases almost linear with frequency. Above the percolation threshold ($\Phi \geq 0.2$), it shows a characteristic conductivity plateau in the small frequency regime. Since at low frequencies the value of the conductivity σ' agrees fairly well with the dc-conductivity, the plateau value exhibits the characteristic percolation behavior considered above. In the high frequency regime the conductivity depicted in Fig. 30a behaves similar to that of the NBR/N220-samples shown in Fig. 29, i. e. above a critical frequency ω_ξ it increases according to a power law with an exponent n significantly smaller than one. In particular, just below the percolation threshold for $\Phi = 0.15$ the slope of the regression line in Fig. 30a equals 0.98, while above the percolation threshold for $\Phi = 0.2$ it yields n = 0.65. This transition of the scaling behavior of the ac-conductivity at the percolation threshold results from the formation of a conducting carbon black network with a self-similar structure on mesoscopic length scales.
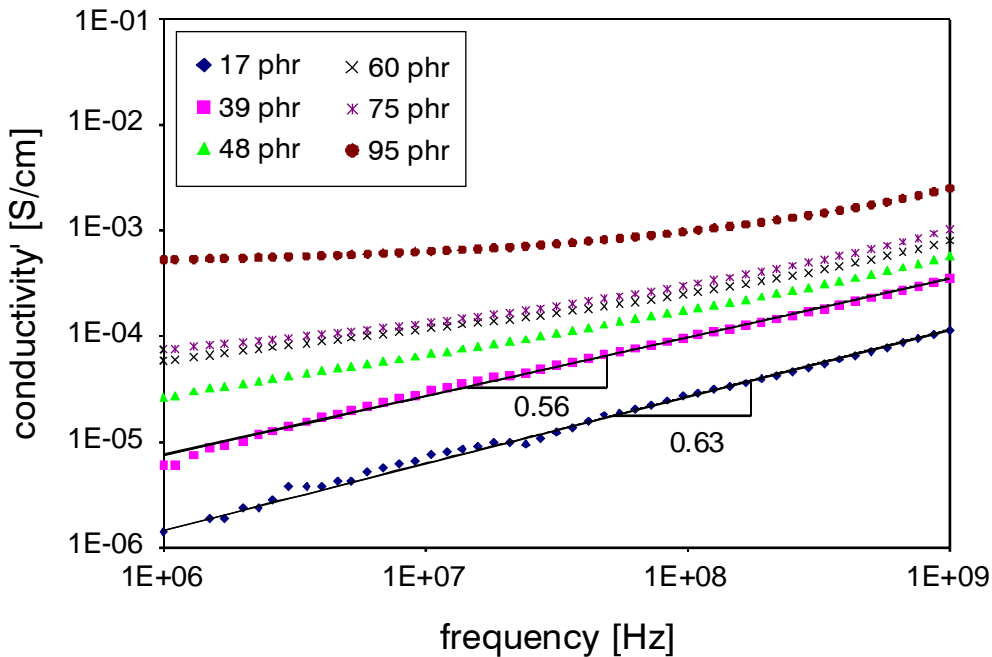
Fig. 29: AC-conductivity σ' vs. frequency at 20 °C of NBR-samples filled with various amounts of N220, as indicated. The solid lines correspond to the scaling behavior Equ. (17), obtained in the high frequency range up to 1 GHz.

The reduced value of the scaling exponent, observed in Figs. 29 and 30a for filler concentrations above the percolation threshold, can be related to anomalous

diffusion of charge carriers on fractal carbon black clusters. It appears above a characteristic frequency ω_ξ, when the charge carriers move on parts of the fractal clusters during one period of time. Accordingly, the characteristic frequency ω_ξ for the cross-over of the conductivity from the plateau to the power law regime scales with the correlation length ξ of the filler network.
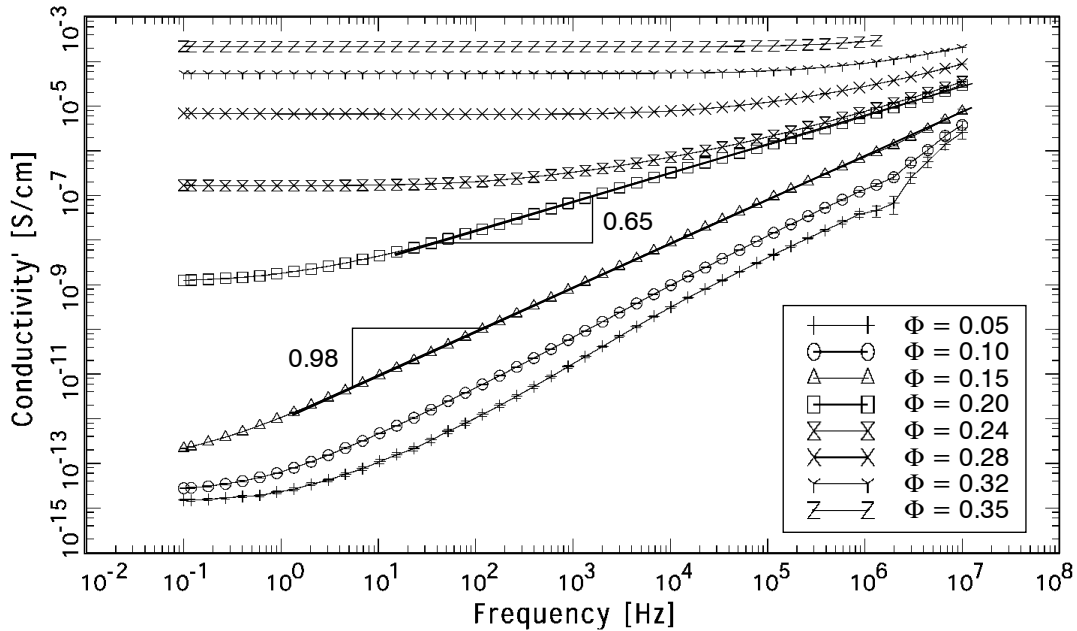

Fig. 30a: Conductivity σ' vs. frequency at 20 °C of S-SBR-samples filled with various amounts of N550, as indicated.
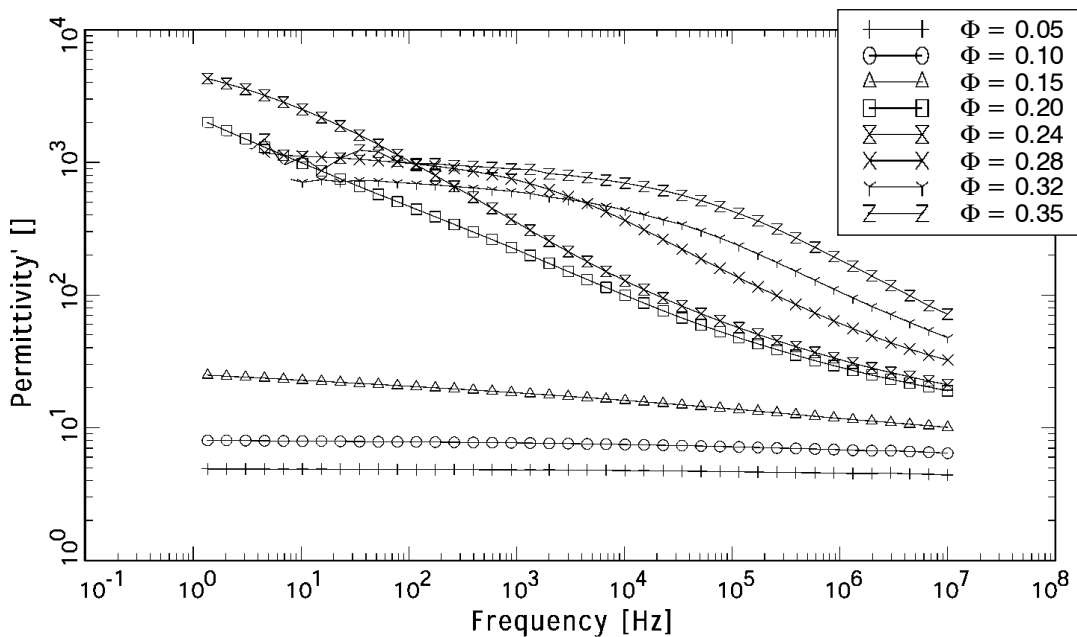

Fig. 30b: Permittivity ε' vs. frequency at 20 °C of the S-SBR-samples of Fig. 30a.

For a quantitative analysis of the scaling and cross-over behavior of the ac-conductivity above the percolation threshold we refer to the predictions of percolation theory [128,136,137]:

$$\sigma'(\omega) \sim \omega^n \qquad \text{for } \omega > \omega_\xi \qquad (17)$$

and

$$\omega_\xi(\Phi) \cong \omega_{\xi,o}\left(\frac{\xi}{d_o}\right)^{-d_w} \cong \omega_{\xi,o}\left(\frac{\Phi-\Phi_c}{1-\Phi_c}\right)^m \qquad (18)$$

For the evaluation of the front factor the Einstein equation for the conductivity σ_o can be used. It yields:

$$\omega_{\xi,o} = \tau_{\xi,o}^{-1} = \frac{6\sigma_o k_B T}{e^2 n_o d_o^2} \qquad (19)$$

Here, e is the electron electric charge, n_o is the charge carrier density and d_o is the size of the lattice units, i. e. the primary aggregates. The two critical exponents $n = (d_w-d_f+1)/d_w \approx 0.6$ and $m = \nu d_w \approx 3.3$ are given by the characteristic structure parameters of percolation in 3 dimensions, i. e. the fractal dimension $d_f \approx 2.5$, the anomalous diffusion exponent $d_w \approx 3.8$ and the correlation length exponent $\nu \approx 0.87$ [128,137]. The experimental value $n = 0.65$ found in Fig. 30a is in fair agreement with this prediction, indicating that for sufficient high carbon black concentrations a percolation structure of the filler network is realized in the systems. However, the experimental value $n = 0.65$ lies also not far away from the predicted value $n \approx 0.74$ for a kinetically aggregated CCA-network structure, obtained with a fractal dimension $d_f \approx 1.8$ and an anomalous diffusion exponent $d_w \approx 3.1$. A more detailed discussion of the scaling behavior of the conductivity in the framework of the two models, percolation and kinetic aggregation, is presented in Appendix D.

The permittivity shown in Fig. 30b characterizes the polarization of the samples in an alternating field. At low carbon black concentrations, the permittivity is relatively small ($\varepsilon' \cong 10$) and almost independent of frequency. At higher carbon black concentrations, above the percolation threshold ($\Phi \geq 0.2$), relatively high values of the permittivity ($\varepsilon' \cong 10^3$) are found in the low frequency regime, but with increasing frequency a relaxation transition takes place and the permittivity ε' falls off drastically. The location of the relaxation transition on the frequency scale, ω_R, is shifted to higher frequencies with rising carbon black concentration. Note that the corresponding relaxation current leads to the step-like increase of the conductivity in

the high frequency regime, observed for the system NR/N339 in Fig. 28. For the present sample series S-SBR/N550, shown in Figs. 30a and 30b, this relaxation current is not significant on the chosen logarithmic scale. Obviously, it is hidden by the relatively high conduction plateau. In this sense, conductivity and permittivity are de-coupled, allowing for a proper analysis of the anomalous diffusion- and polarization transitions, separately.

An explanation of the observed relaxation transition of the permittivity in carbon black filled composites above the percolation threshold is again provided by percolation theory. Two different polarization mechanisms can be considered: (i) polarization of the filler clusters that are assumed to be located in a non polar medium, and (ii) polarization of the polymer matrix between conducting filler clusters. Both concepts predict a critical behavior of the characteristic frequency ω_R similar to Equ. (18). In the case (i) it holds $\omega_R \cong \omega_\xi$, since both transitions are related to the diffusion behavior of the charge carriers on fractal clusters and are controlled by the correlation length ξ of the clusters. Hence, ω_R corresponds to the anomalous diffusion transition, i. e. the cross-over frequency of the conductivity as observed in Fig. 30a. In the case (ii), also referred to as random resistor-capacitor model, the polarization transition is affected by the polarization behavior of the polymer matrix and it holds [128,136,137]:

$$\omega_R(\Phi) \cong \frac{1}{R_o C_o} \left(\frac{\Phi - \Phi_c}{1 - \Phi_c} \right)^q \qquad (20)$$

Here, R_o is the resistance of the occupied lattice units and C_o is the capacitance of the non-occupied lattice units. In a first attempt, not considering anomalous diffusion effects, the exponent has been evaluated as $q = \mu + s \approx 2.7$, where $s \approx 0.7$ and $\mu \approx 2.0$ are the conductivity exponents (in 3 dimensions) below and above the percolation threshold, respectively. However, by including anomalous diffusion effects one obtains $q = m = \nu d_w \approx 3.3$ [136,137].

For a quantitative analysis of the percolation behavior of ω_R, considered in Equ. (20), the permittivity data shown in Fig. 30b have been adapted with an empirical Cole-Cole function [131,132]. The fits are quite good, yielding relatively small broadness parameters between 0.36 and 0.5. The obtained relaxation times $\tau_R = \omega_R^{-1}$ are depicted in Fig. 31 in dependence of filler concentration Φ. Furthermore, the cross-over times $\tau_\xi = \omega_\xi^{-1}$ and the limiting low frequency plateau values of the conductivity σ' ($\omega \rightarrow 0$), obtained from the data in Fig. 30a, are represented in Fig. 31. They have been evaluated by a simple shifting procedure for constructing a conductivity master curve, as applied e. g. in Ref. 135. The solid lines depicted in Fig. 31 are fitted curves for the characteristic composite parameters σ' ($\omega \rightarrow 0$) = σ_{DC},

τ_ξ and τ_R according to Equs. (15), (18) and (20), respectively. Thereby, a common exponent q = m = 10.1 and a single value of the percolation threshold Φ_c = 0.165 have been assumed, providing best fits to the experimental data with correlation coefficients r^2 between 0.978 and 0.996. The conductivity exponent corresponding to Equ. (15) is found as μ = 7.4 and the limiting conductivity for Φ = 1 yields σ_o = 12.4 S/cm. For the two front factors of Equs. (18) and (20) one obtains $\tau_{\xi,o}$ = 1.4 10^{-14} s and $\tau_{R,o}$ = 6.3 10^{-13} s.
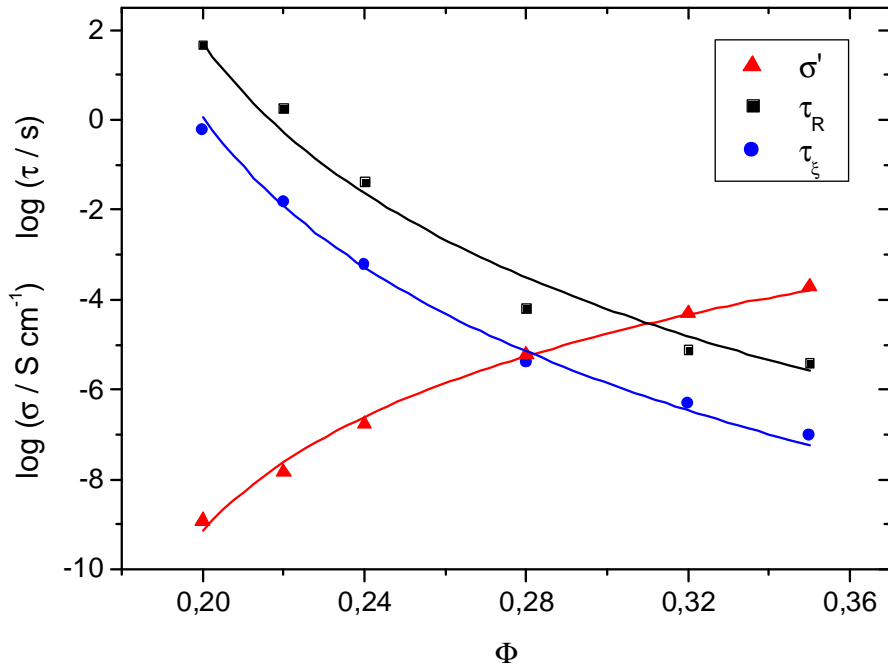
Fig. 31: Characteristic parameters of the S-SBR/N550 composites, σ' ($\omega{\rightarrow}0$), τ_ξ and τ_R, for various carbon black concentrations Φ obtained from Figs. 30a and 30b. The solid lines are adapted to Equs. (15), (18) and (20), respectively.

If the estimated fitting parameters are compared to the predicted values of percolation theory, one finds that all three exponents are much larger than expected. The value of the conductivity exponent μ =7.4 is in line with the data obtained in Section 3.3.2, confirming the non-universal percolation behavior of the conductivity of carbon black filled rubber composites. However, also the values of the critical exponents q = m = 10.1 seem to be influenced by the same mechanism, i. e. the superimposed kinetic aggregation process considered above (Equ. (16)). This is not surprising, since both characteristic time scales of the system depend on the diffusion of the charge carriers characterized by the conductivity.

The front factors obtained from the fittings in Fig. 31 can be used for a dielectric characterization of the network units, e. g. for an evaluation of the charge carrier density n_o of the primary carbon black aggregates as given by Equ. (19).

Therefore, the electric charge $e^2 = 2.3 \ 10^{-28}$ Jm and the conductivity $\sigma_o = 1.1 \ 10^{13} \ s^{-1}$ have to be inserted with respect to Gaussian units. The mean diameter of primary aggregates in S-SBR composites (50 phr N550) has been obtained from TEM analysis as $d_o = 157$ nm. With T = 293 K and $k_B = 1.38 \ 10^{-23}$ J/K this yields for the reduced charge carrier density $n_o \ d_o^3 = 2.6$, i. e. the number of charge carriers per primary aggregate is of order one. This relative small number of charge carriers can be related to the tunneling or hopping conductivity mechanism between conducting nanoscopic islands (primary aggregates) with a high Coulomb exclusion energy. The exclusion energy for a single electron can be roughly estimated from the limiting relaxation time $\tau_{R,o} = R_o \ C_o$, if the resistance R_o of the lattice units is expressed by the conductivity σ_o via $R_o \cong (\sigma_o \ d_o)^{-1} = 5.1 \ 10^3 \ \Omega$. This yields for the capacitance of the lattice units $C_o = 1.2 \ 10^{-16}$ F, or in Gaussian units $C_o = 1.1 \ 10^{-6}$ m. Hence, the exclusion energy of a single electron results as $E_C = e^2/2C_o = 10^{-22}$ J. This value is more than one order of magnitude smaller than the thermal energy $k_B \ T = 4 \ 10^{-21}$ J, which has to be exceeded for insuring the dominance of the Coulomb exclusion energy. Accordingly, from this estimates it appears that the charge carrier density is not limited by the exclusion energy but governed by thermal fluctuations. However, note that this calculation is not very precise, since the local geometrical structure of the lattice units is not considered properly. A more fundamental study of charge transport mechanisms in carbon black filled rubbers should take into account that the lattice units are fractal objects (primary carbon black aggregates), which are separated by small gaps not larger than a few nanometers.

4.3 Flocculation dynamics and the nature of filler-filler bonds

For a deeper understanding of filler networking in elastomers it is useful to monitor structural relaxation phenomena during heat treatment (annealing) of the uncross-linked composites. This can be achieved by investigations of the time development of the small strain storage modulus G'_0 that provides information about the flocculation dynamics [140-142]. Fig. 32a shows the time development of G'_0 of S-SBR melts of variable molar mass filled with 50 phr carbon black (N234), when a step-like increase of the temperature from room temperature to 160 °C is applied. Fig. 32b shows a strain sweep of the same systems after 60 minutes annealing time. Dependent on the molar mass M_w, as indicated, a pronounced increase of G'_0 is observed in the first minutes that levels out more or less to a plateau value at larger annealing times. In agreement with recent studies of Wang et al. [143], the largest plateau value is observed for the lowest molar mass, indicating that the increase of the modulus results from flocculation of primary aggregates to form secondary aggregates (clusters) and finally a filler network. It appears that a weekly bonded superstructure develops in the systems during heat treatment that stiffens the polymer matrix. With increasing dynamic strain amplitude, as depicted in Fig. 32b, a stress-induced breakdown of the filler clusters takes place and the storage modulus
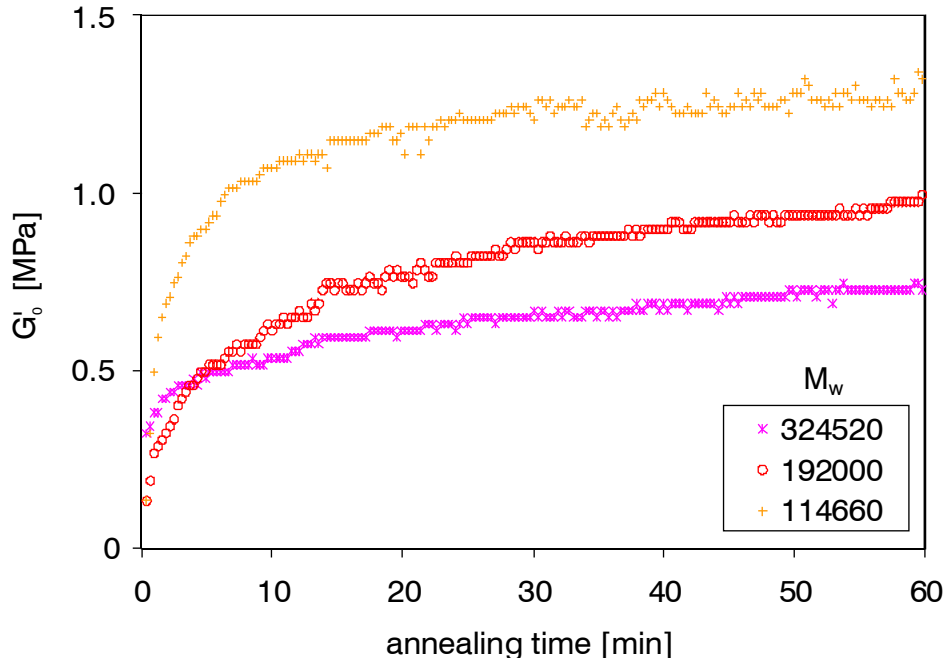

Fig. 32a: Time development of the small strain storage modulus of uncross-linked S-SBR composites with 50 phr N234 during heat treatment at 160 °C for various molar masses, as indicated (0.28 % strain, 1 Hz).
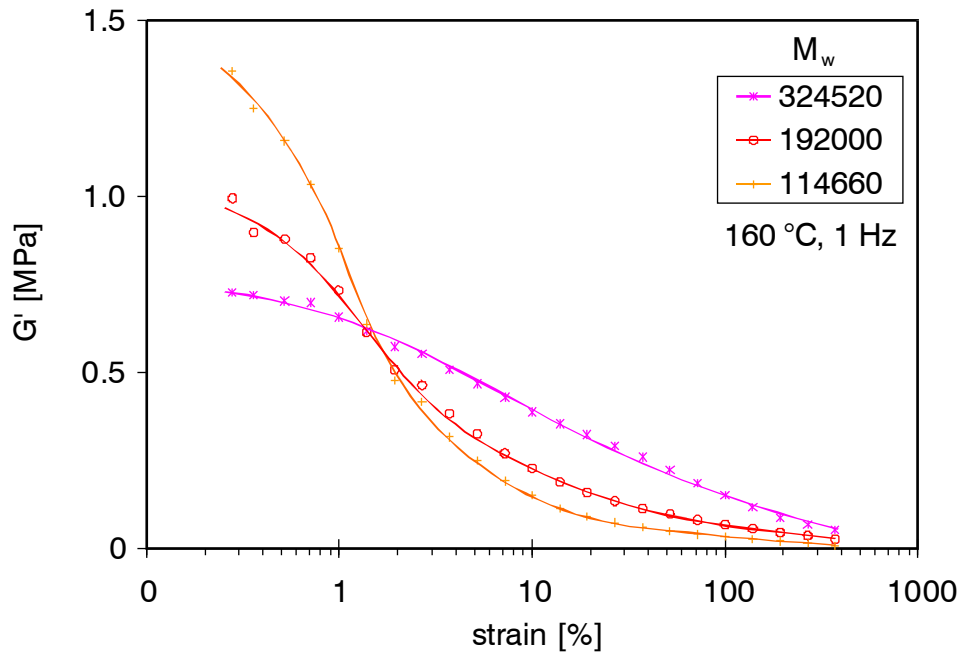
55

Fig. 32b: Strain dependency of the storage modulus of the samples depicted in Fig. 32a after heat treatment for 60 minutes at 160 °C.

decreases by about one order of magnitude (Payne effect). With respect to the variable molar mass of the systems, Fig. 32b shows a cross-over of the moduli with increasing strain, indicating that a larger molar mass stabilizes the filler-filler bonds more effectively. This can be related to the overlapping action of tightly bound polymer chains in the contact area between adjacent filler particles.

Inspired by the above flocculation analysis and the dielectric investigations described before, a model concerning the structure-property relationships of filler-filler bonds in a bulk rubber matrix can be developed as illustrated in Fig. 33. According to this model, the stiffness of filler-filler bonds is governed by the remaining gap size between contacting particles. This, in turn, depends on the ability to squeeze out the bound polymer chains from the contact area under the attractive action of the van der Waals force between the filler particles. This process leads to a stiffening of filler-filler bonds. It is favored by several factors, e. g. a high ambient temperature, low molar mass, small particle size, weak polymer-filler- and strong filler-filler interaction.

The mechanical connectivity between the filler particles is provided by a flexible, nanoscopic bridge of glassy polymer, resulting from the immobilization of the rubber chains in the confining geometry close to the gap. Since the stiffness of the bonds transfers to the stiffness of the whole filler network, the small strain elastic modulus of highly filled composites is expected to reflect the specific properties of the filler-filler bonds. In particular, the small strain modulus increases with decreasing gap size during heat treatment as observed in Fig. 32a. Furthermore, it

exhibits the same temperature dependence as that of the bonds, i. e. the characteristic Arrhenius behavior typical for glassy polymers. Note however that the stiffness of the filler network is also strongly affected by its global structure on mesoscopic length scales. This will be considered in some more detail in the next section.
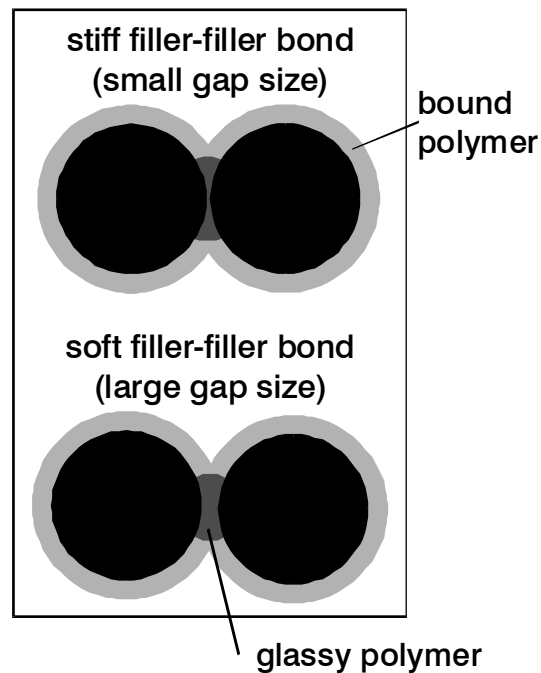
Fig. 33: Schematic view considering the structure of filler-filler bonds in a bulk rubber matrix. The impact of gap size on the stiffness of filler-filler bonds becomes apparent.

In the case of carbon black filled diene-rubber composites the polymer-filler interaction is generally quite strong due to the high affinity between the π-electrons at the carbon surface and those in the double bonds of the chains. According to the site energy distribution function estimated in Section 3.1.2, the typical interaction energy between carbon black and ethylene, representing a single double bond, lies between 10 and 35 kJ/mol and depends on the grade number. A more practical procedure for characterizing the polymer-filler interaction in elastomer composites is the estimation of bound rubber i.e. the amount of polymer tightly bound to the filler surface after mixing [144]. It is well known that this amount increases with the molar mass of the polymer and the specific surface area of the filler particles, but is also affected significantly by the surface activity, given e.g. by the site energy distribution function of the filler obtained with polymer analogous gases [144-147]. A further effect comes in from the preparation conditions of the composites, e.g. mixing time [148], since the formation of bound rubber is a slow dynamical process that requires time.

Fig. 34: Results of bound rubber estimates at room temperature for various carbon black filled S-SBR composites, as indicated.

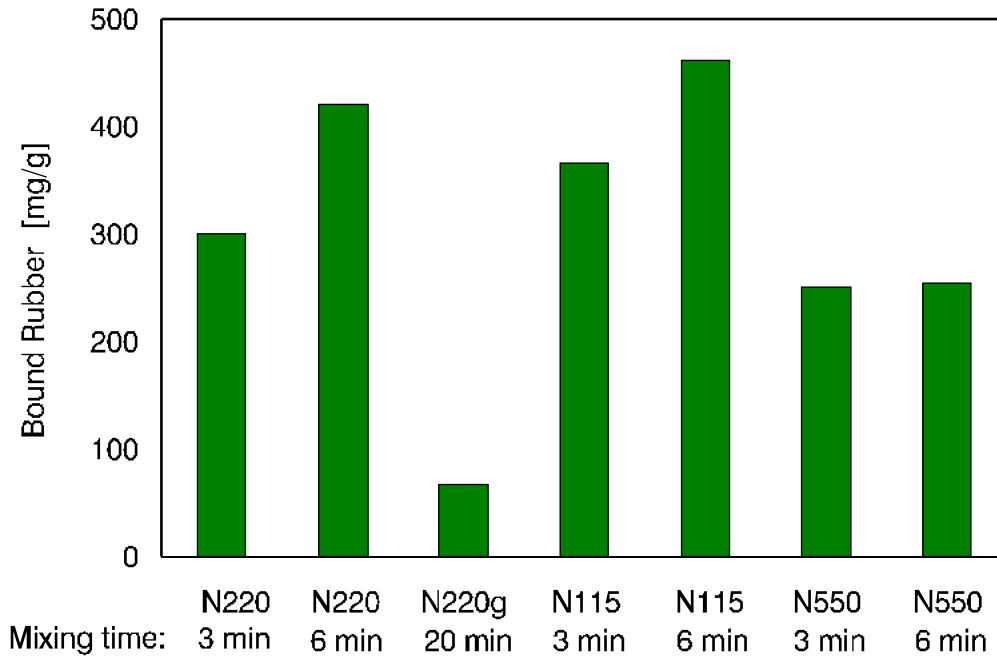Fig. 34 shows the result of bound rubber estimates at room temperature for variously mixed S-SBR composites filled with 50 phr of four different carbon blacks. The furnace blacks were mixed for 3 and 6 minutes in an internal mixer, respectively, while the graphitized black N220g was mixed for 20 minutes on a roller mill. The dispersion rating was found to be larger than 90% for all systems. It becomes obvious that the amount of bound rubber increases with increasing mixing time from 3 to 6 minutes. This results from an exchange of shorter chains, already bound to the filler surface, by longer chains during the ongoing mixing process. The longer chains are bound more tightly to the surface due to a higher number of adhesive contact spots per chain [144-146]. Beside the effect of mixing time the estimated bound rubber reflects the difference in specific surface of the furnace blacks that increases from N550 (41 m^2/g) via N220 (116 m^2/g) to N115 (143 m^2/g). A deviation from this correlation is observed for the graphitized black N220g that shows a significantly smaller amount of bound rubber as compared to its relatively large specific surface (88 m^2/g). This effect can be attributed to the lower surface activity of the graphitized black that results from the marked reduction of highly energetic sites during graphitization. (compare Fig. 15 and Tab. 2). From this observation it appears that the highly energetic sites are the dominating factor for strong polymer-filler couplings.

The different interaction strength between polymer and filler leads to characteristic implications for the structural relaxation behavior (flocculation) of filler particles in highly entangled polymer melts. Fig. 35 shows the strain dependency of

the storage modulus G' for the two composites S-SBR/N220g and S-SBR/N220 (mixing time: 6 minutes) before and after heat treatment (annealing) of the samples for 20 minutes at 160 °C. Obviously, a significant increase of the small strain modulus of both systems results during heat treatment, referring to the flocculation of filler particles. With increasing strain the moduli decrease significantly due to a stress-induced successive breakdown of filler clusters. A comparison of the two systems filled with the furnace black N220 and the graphitized black N220g shows a stronger increase of the moduli for the system with the graphitized black, indicating a more pronounced flocculation during heat treatment. According to the model of filler-filler bonds considered in Fig. 33, the lower amount of tightly bound polymer around the graphitized black N220g supports the flocculation. It implies smaller contact gaps, because the polymer between the contacting particles can be squeezed out more readily by the attractive van der Waals forces. This leads to stiffer filler-filler bonds and hence to a higher modulus of the filler network. From principal reasons it is also possible that the global structure of the filler network of the two systems prepared with the furnace and graphitized black after heat treatment is generally different, e. g. the arrangement of the graphitized carbon particles is more compact. However, we will argue below that the formation of the filler network is governed by a diffusion controlled cluster-cluster aggregation (CCA)-process that leads to a universal CCA-network structure. Under this condition the difference in stiffness of the two systems has to be related to a change of the local stiffness of the filler-filler bonds.
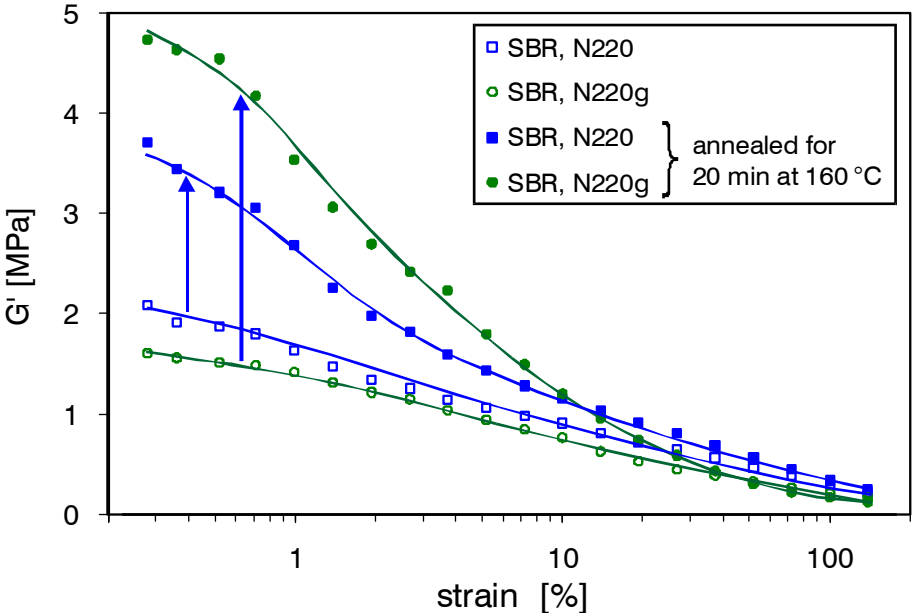

Fig. 35: Strain dependency of the storage modulus (G' at 60 °C) of uncross-linked S-SBR composites filled with 50 phr N220 and N220g, respectively, before and after heat treatment for 20 minutes at 160 °C.

The impact of bound rubber on the spacing of filler-filler contact gaps during annealing of carbon black composites at elevated temperature is affected by the amount of bound rubber estimated at this particular temperature. In so far, the values listed in Fig. 34, obtained at room temperature, may not be representative, because the amount of bound rubber depends on the extraction temperature. In general, the amount of bound rubber is also affected by the solvent used for extraction and decreases with increasing extraction temperature [150-153]. In earlier studies a linear decrease in bound rubber with temperature was observed, extrapolating to zero at 375 °C [150]. Other authors found a much more dramatic decrease with minimum bound rubber at about 100 °C [151]. Subsequent studies of Chapman et al [152], comparing extraction in vacuo, nitrogen and air, respectively, found a moderate decrease of bound rubber of about 30 % at 100 °C in vacuo as compared to room temperature and a much more pronounced decrease in air and also in nitrogen atmosphere. They concluded that oxidative chain scission reduces the bound rubber content at elevated temperature if determined in air and also in nitrogen. Similar results were obtained by Kida et al. [153]. They concluded from NMR-relaxation measurements that only the content of the outer, most mobile rubber phase is reduced while the highly immobilized phase close to the carbon black surface remains almost constant up to 113 °C. From these results we can expect that for an annealing temperature of about 160 °C, which is also applied during vulcanization, bound rubber is still present at the carbon black surface and hinders the aggregation of neighboring particles. Note that this is also expected from simple energetic arguments, since the above estimated adsorption energy of ethylene on N220, $Q \approx 10 - 35$ kJ/mol, is almost one order of magnitude larger that the thermal energy $RT = 3.6$ kJ/mol at 160 °C.

The effect of bound rubber on the stiffness of filler-filler bonds is essential for the small strain modulus G'_0. It allows for a qualitative explanation of various well known phenomena described e. g. in the pioneering papers of Payne [28-35]. In particular, the observed decrease of G'_0 with increasing mixing time [33,148] can be related to a softening of the bonds due to a successive increase of bound rubber. Furthermore, the variation of G'_0 with polymer type [30, 154] can be related to the impact of bound rubber on the spacing of filler-filler bonds, implying that a strong polymer-filler coupling or high molar mass lowers the value of G'_0. Note that this interpretation can also explain the more or less significant correlation between the small strain modulus and the electrical conductivity level obtained e. g. in Ref. 154. This kind of correlation is also found, if composites with graphitized and non-graphitized carbon blacks of the same grade number are compared. The higher stiffness of composites with graphitized blacks is typically accompanied by a higher conductivity level [121]. Both effects refer to a smaller gap size between contacting primary aggregates in the case of graphitized blacks.

Beside the stiffness of filler-filler bonds, the amount of bound rubber impacts also the strength of the bonds between interacting filler particles. Due to the overlapping action of the tightly bound polymer chains close to the contact area of neighboring filler particles, the mechanical stability of filler-filler bonds increases with increasing amount of bound rubber. This explains the cross-over behavior of the moduli (after heat treatment) as observed in Figs. 32 and 35: The systems with the lower amount of bound rubber, i. e. the composites with graphitized blacks and the low molar mass of the polymer, respectively, show the largest values of the small strain modulus G'_0, but the drop of the moduli with increasing strain appears at significantly smaller strain amplitudes. The stabilizing bound rubber layer can be considered to act like a spanning net around the filler clusters, implying a high flexibility of the filler network. We will see that this kind of reinforcing action is responsible for the pronounced hysteresis and high strength of reinforced rubbers in the dynamic strain regime up to around 100 %. Further significant effects of the bound rubber layer result in the quasi-static high strain regime. This will be considered in the next section.

In conclusion, the investigations of electrical properties of carbon black filled rubbers, presented in Section 4.2 and Appendix C and D, indicate that a percolation structure for the filler network is realized on mesoscopic length scales, if a critical filler concentration is exceeded. This structure seems to be modified by a superimposed kinetic aggregation process that refers to the non-universal value of the percolation exponent and the impact of specific surface on the percolation threshold. Further experimental evidence for a kinetic aggregation mechanism of colloidal particles dispersed in a rubber matrix is given by the mechanical response of the uncross-linked composites during heat treatment (annealing), demonstrating that a relative movement (flocculation) of the particles takes place that depends on particle size, molar mass of the polymer as well as polymer-filler and filler-filler interaction. It has been argued that the mechanical stiffness of filler-filler bonds is governed by the remaining gap size between adjacent filler particles that develops during annealing (and cross-linking) of filled rubbers. Based on the model of filler-filler bonds depicted in Fig. 33, a qualitative explanation of the observed flocculation effects is possible by referring to the amount of bound rubber and it is impact on the stiffness and strength of filler-filler bonds.

5.   Rubber reinforcement by kinetically aggregated filler networks

In the last decades, remarkable progress has been obtained in understanding filler networking and its implications on the mechanical response of dynamically excited and highly strained rubber composites. This is summarized in a recent review of Heinrich and Klüppel [24], which is reprinted in Appendix B. According to this paper, two fundamental micro-mechanical concepts of non-linear viscoelasticity, which are based on fractal approaches of filler networking, have been developed: the (L-N-B)-model [56] and the cluster-cluster-aggregation (CCA)-model [21-23,85]. They consider the arrangement of filler particles in clusters with well defined fractal structure and the elasticity or fracture of such clusters under external strain. The two models refer to different geometrical arrangements of filler particles in particulate fractal network structures, described by percolation theory or kinetic cluster-cluster aggregation, respectively.

We will focus here on the CCA-model of filler networking, since the investigations of flocculation and electrical properties considered in the last section provide strong evidence for a kinetic aggregation mechanism of filler particles in elastomers. A further strong indication for the CCA-mechanism is given by the predicted scaling behavior of the small strain modulus considered below. We will see that this scaling behavior is well fulfilled for different elastomer systems with various fillers. On the contrary, the corresponding scaling prediction of percolation theory clearly fails if applied for filler reinforced rubbers, since experimental data result in much smaller exponents than the predicted one (Appendix B).

5.1   Structure and elasticity of filler networks at small strain

5.1.1 Cluster-cluster aggregation (CCA) in elastomers

The kinetic cluster-cluster-aggregation (CCA)-model is based upon the assumption that nanoscopic filler particles, like carbon blacks, are not fixed in space but can perform random movements, i. e. the particles are allowed to fluctuate around their mean position in a polymer matrix. Upon contact of neighboring particles or clusters they stick together, irreversibly. This refers to the fact that the thermal energy of colloidal particles is in general much smaller than their interaction energy. Due to the high viscosity of the polymer, the mobility of the particles is restricted, but it increases significantly with decreasing particle size and increasing temperature because the viscosity decreases. For sufficient high temperature, small filler particles and high filler concentrations, above the gel point ($\Phi > \Phi^*$), the mean distance of the particles becomes smaller than the fluctuation length, implying that the aggregation mechanism is no longer influenced by the restricted mobility of the

particles. Under this condition, diffusion limited cluster by cluster aggregation leads to a space-filling configuration of CCA-clusters, similar to colloid aggregation in low viscosity media [21-25,85]. A schematic view of this situation above the gel point Φ^* is shown in Fig. 36 (c). For filler concentrations below the gel point, an irregular configuration of partly separated clusters results as shown in Fig. 36 (b). Note that the global connectivity of such systems, as experienced e. g. by the electrical conductivity measurements in Section 4.2, is similar to a percolation structure, since the clusters are "randomly connected" by small conducting gaps. This reflects the fact that the mechanical gel point is generally larger than the electrical percolation threshold ($\Phi^* > \Phi_c$). A discussion of this point is found in Appendix C.
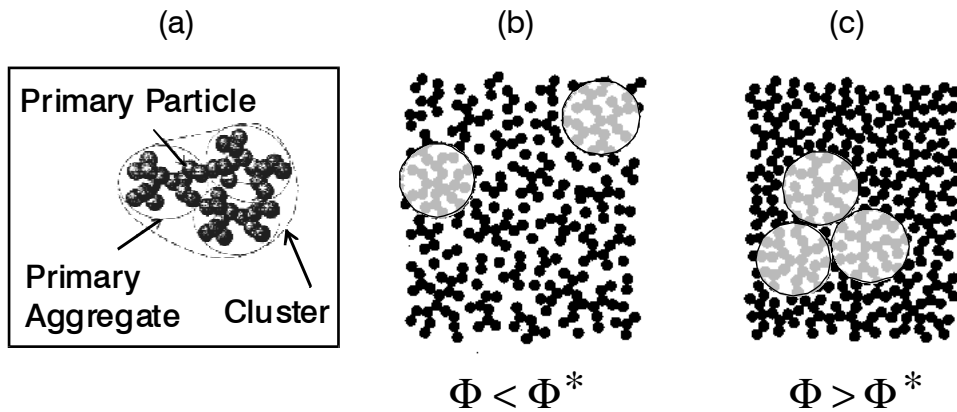
Fig. 36: Schematic view of kinetically aggregated filler clusters in rubber below and above the gel point Φ^*. The left side (a) characterizes the local structure of carbon black clusters, build by primary particles and primary aggregates. Accordingly, every black disc in (b) or (c) represents a primary aggregate.

Due to the characteristic self-similar structure of the CCA-clusters with fractal dimension $d_f \approx 1.8$ [3-8,12], the cluster growth in a space-filling configuration above the gel point Φ^* is limited by the solid fraction Φ_A of the clusters. The cluster size is determined by a space-filling condition, stating that, up to a geometrical factor, the local solid fraction Φ_A equals the overall solid concentration Φ:

$$\Phi_A (\Phi) = N_F^{-1} \Phi \qquad \text{for } \Phi > \Phi^* \qquad (21)$$

The proportionality constant N_F in Equ. (16) is a generalized Flory-Number of order one ($N_F \cong 1$) that considers a possible interpenetrating of neighboring clusters [22]. For an estimation of cluster size in dependence of filler concentration we take into account that the solid fraction of fractal CCA-clusters fulfils a scaling law similar to Equ. (14). It follow directly from the definition of the mass fractal dimension d_f given by $N_A \cong (\xi/d)^{d_f}$, which implies:

$$\Phi_A(\xi) \equiv \frac{V_A}{(\pi/6)\xi^3} = \frac{N_A(\xi)d^3\Phi_p}{\xi^3} \cong \left(\frac{d}{\xi}\right)^{3-d_f}\Phi_p \tag{22}$$

Here, V_A is the solid volume and N_A is the number of particles or primary aggregates of size d in the clusters of size ξ. Φ_p is the solid fraction of primary aggregates considered in Section 3.2.2. For spherical filler particles, as shown in Fig. 36 (b) and (c), it equals $\Phi_p = 1$.

From a combination of Equs. (21) and (22) one finds that the cluster size ξ decreases with increasing filler concentration Φ according to a power law. This reflects the fact that smaller clusters occupy less empty space than larger clusters (space-filling condition). It means that the correlation length of the CCA filler network, i. e. the size of the fractal heterogeneity, decreases with increasing filler concentration. This is similar as in percolation theory, though the scaling behavior is generally different.

5.1.2 Elasticity of flexible chains of filler particles

In view of a micro-mechanical characterization of the elasticity of fractal CCA-filler networks it is sufficient to consider the elastic properties of a single unit cell, because the system is homogeneous on length scales larger than the correlation length ξ. This implies that the elastic modulus G_A of a single CCA-cluster is representative for the whole network. It can be evaluated by referring to Kantor and Webman's model of flexible chains of filler particles that is based on a vectorial Born-lattice model with a tension- and bending energy term between contacting particles [155]. Thereby, we use an approximation of the CCA-cluster backbone as a single spanning arm, i. e. we describe it as a tender, curved rod [21-24]. This is possible, because the CCA-cluster backbone has almost no branches [3,12], implying that the energy of a strained cluster is primary stored in filler-filler bonds along the connecting path between the backbone particles. A schematic representation of this approach is depicted in Fig. 37.

According to this model, the clusters act as molecular springs with end to end distance ξ, consisting of N_B backbone units of length d. The connectivity of the backbone units is characterized by the backbone fractal dimension $d_{f,B}$. Due to the fractal nature of CCA-clusters it holds:

$$N_B \cong \left(\frac{\xi}{d}\right)^{d_{f,B}} \tag{23}$$

In the present approximation, $d_{f,B}$ is identified with the minimum- (or chemical) fractal dimension, i. e. $d_{f,B} = d_{min} \approx 1.3$ for CCA-clusters [3,12].
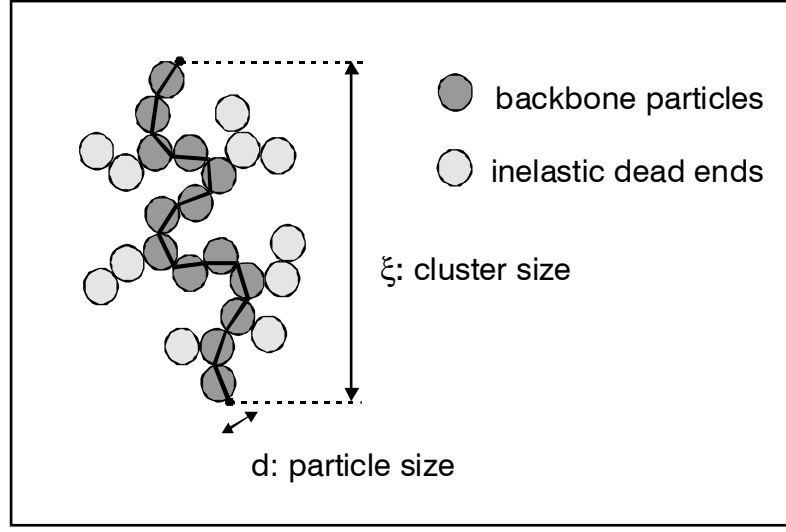
Fig. 37: Schematic view of the decomposition of a CCA-cluster in elastically active backbone particles and inelastic dead ends. Energy is stored along the connecting path of the backbone particles, indicated as curved line.

Following the line of Kantor and Webman's two dimensional model, the strain energy H of a chain composed of a set of N_B singly connected units $\{b_i\}$ of length d under an applied force **F** at the two ends of the chain is given by [155]:

$$H = \frac{F^2 N_B S_\perp{}^2}{2\,G} + \frac{F^2 L_{\parallel}\,d}{2\,Q} \qquad (24)$$

where

$$S_\perp{}^2 = \frac{1}{F^2 N_B} \sum_{i=1}^{N_B} \left[(\boldsymbol{F} \times \boldsymbol{z})\left(\boldsymbol{R}_{i-1} - \boldsymbol{R}_{N_B}\right) \right]^2 \qquad (25)$$

is the squared radius of gyration of the projection of the chain on a two dimensional plane and

$$L_{\parallel} = \frac{1}{F^2 d} \sum_{i=1}^{N_B} \left(\boldsymbol{F} \cdot \boldsymbol{b}_i \right)^2 \qquad (26)$$

Here, G and Q are local elastic constants corresponding to the changes of angles between singly connected bonds and longitudinal deformation of single bonds, respectively. The vector **z** is a unit vector perpendicular to the plane. For long chains the second term in Equ. (24) can be neglected and the major part of the

strain energy H results from the first term, i. e. the bending term of the chain. Then, the force constant k of the chain, relating the elastic energy to the displacement squared of the end of the chain, is well approximated by the bending force constant k_S [155]:

$$k \approx k_S = G / (N_B S_\perp^2) \tag{27}$$

The mathematical treatment of a three dimensional generalization of this linear elastic model is more complex. In this case the angular deformation is not limited to the on-plane bending, but also off-plane twisting takes place. This model is depicted schematically in Fig. 38.
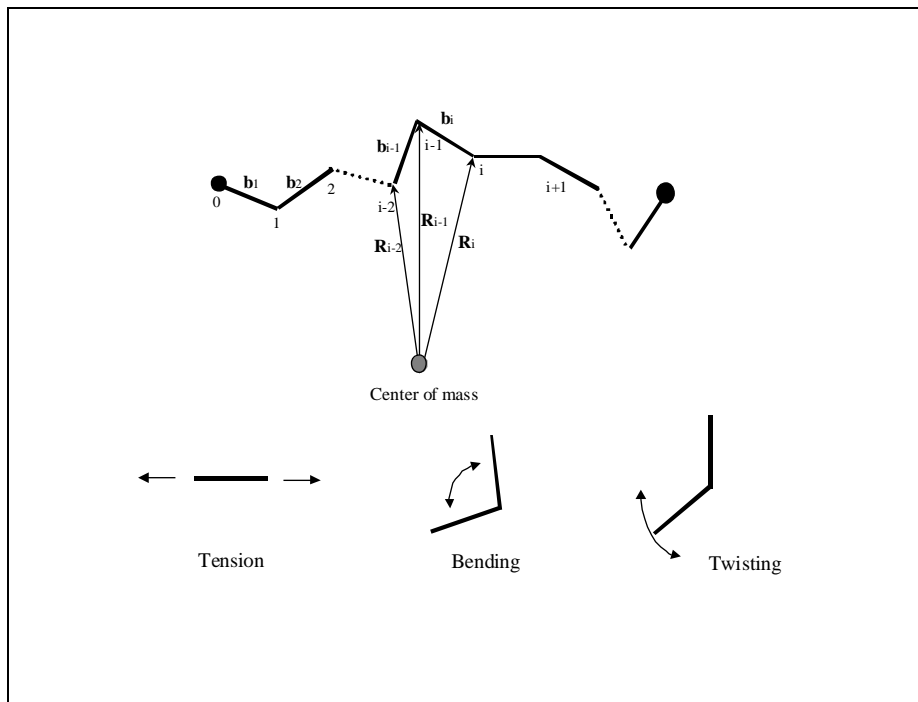
Fig. 38: Illustration of Kantor and Webman's model of flexible chains with tension-, bending- and twisting energy terms [155].

In a simplified approach introduced by Lin and Lee [56], the contributions from the two different kinds of angular deformation, bending and twisting, have been taken into account by an averaged bending-twisting deformation. This is obtained by replacing the elastic constant G, in the first term of Equ. (24), through an averaged elastic constant $\overline{G}$ of different kinds of angular deformations. Then, by using the relation $S_\perp \cong \xi$ and Equ. (23), one obtains for the force constant $k \approx k_S$ of the cluster backbone:

$$k_S = \frac{\kappa \, \overline{G}}{d^2} \left(\frac{d}{\xi}\right)^{2+d_{f,B}} \tag{28}$$

where κ is a geometrical factor of order one. The elastic modulus of the cluster backbone is then found as:

$$G_A \equiv \xi^{-1} k_S = \frac{\kappa \overline{G}}{d^3} \left(\frac{d}{\xi}\right)^{3+d_{f,B}} \tag{29}$$

Equ. (29) describes the modulus G_A of the clusters as a local elastic bending-twisting energy term $\overline{G}$ times a scaling function that involves the size and geometrical structure of the clusters. Note that in the case of a linear cluster backbone with $d_{f,B} = 1$, Equs. (28), (29) correspond to the well know elastic behavior of linear, flexible rods, where the bending modulus falls off with the 4th power of the length ξ. The above approach represents a generalization of this behavior to the case of flexible, curved rods. Experimental evidence for the elastic response of filler clusters of nano-particle chain aggregates is given by Friedlander et al. [156,157], who showed by TEM analysis that aggregates of inorganic metal oxides stretch under tension and contract when the tension is relaxed.

5.1.3. Scaling behavior of the small strain modulus

The small strain viscoelastic behavior of filler reinforced rubbers is well known to be strongly affected by the properties of the filler network. This refers to the fact that the elastic modulus G_A of the filler network units, i. e. the CCA clusters, is generally much larger than the elastic modulus G_R of the rubber and a rigidity condition $G_A >> G_R$ is fulfilled. However, from Equ. (29) it is clear that the rigidity condition can not be fulfilled in all cases, because the modulus G_A of the clusters decreases rapidly with increasing size of the clusters. It means that only relatively small filler clusters can reinforce a rubber matrix with $G_R \cong 0.1$ MPa, since large clusters are to soft. In the present linear viscoelastic model of the small strain behavior of elastomer composites, only this case is considered, i.e. the rigidity condition $G_A >> G_R$ is assumed to be fulfilled.

For filler concentrations above the gel point Φ^*, where a through-going filler network is formed, stress between the (closely packed) CCA-clusters is transmitted directly between the spanning arms of the clusters that bend substantially. In this case, the strain of the rubber is almost equal to the strain of the spanning arms of the clusters ($\varepsilon_R \approx \varepsilon_A$). It means that, due to the rigidity condition, $G_A >> G_R$, the overwhelming part of the elastic energy is stored in the bending arms of the clusters

and the contribution of the rubber to the small strain modulus G'_0 of the sample can be neglected, i.e. $G'_0 \approx G_A$. Accordingly, the stored energy density (per unit strain) of highly filled elastomers can be approximated by that of the filler network. This in turn equals the stored energy density of a single CCA-cluster, due to the homogeneity of the filler network on length scales above the cluster size ξ.

In the framework of the approximation given by the rigidity condition, a simple power law relation can be derived for the dependency of the small strain modulus G'_0 of the composite on filler concentration Φ. It is obtained, if G_A in Equ. (29) is expressed by the solid fraction Equ.(22) and the space-filling condition Equ. (21) is used:

$$ G'_o \cong \frac{\overline{G}}{d^3} \left(\frac{\Phi_A}{\Phi_p} \right)^{(3+d_{f,B})/(3-d_f)} \cong \frac{\overline{G}}{d^3} \left(\frac{\Phi}{\Phi_p} \right)^{(3+d_{f,B})/(3-d_f)} \tag{30} $$

Accordingly, we expect a power law behavior $G'_0 \sim (\Phi/\Phi_p)^{3.5}$ of the small strain elastic modulus for $\Phi > \Phi^*$. Thereby, the exponent $(3+d_{f,B})/(3-d_f) \approx 3.5$ reflects the characteristic structure of the fractal heterogeneity of the filler network, i.e. the CCA-clusters. The strong dependency of G'_0 on the solid fraction Φ_p of primary aggregates reflects the effect of "structure" on the storage modulus.

The predicted power law behavior $G'_0 \sim \Phi^{3.5}$ for filler concentrations above the gel point is confirmed by the experimental results depicted in Figs. 39 and 40, where the small strain storage modulus of a variety of filled rubbers is plotted against filler loading in a double logarithmic manner. Fig. 39 shows the scaling properties for carbon black composites, i. e. for the low structure black N326 in NR and S-SBR, respectively, and the classical butyl/N330-data of Payne [28], already depicted in Fig. 2a. Within the framework of experimental errors, Equ. (30) is found to be fairly well fulfilled for all systems. Note however that the 3.5-power law is in general not fulfilled for high structure blacks, since for such systems Φ_p can not considered to be independent of filler concentration, but increases due to an enhanced aggregate fracture with increasing filler loading (compare Section 3.2.2).

Fig. 40 demonstrates that the 3.5-power law also holds for NR composites with inorganic- and polymeric fillers. Beside a technical silica filler, polystyrene (PS)- and poly-methoxy-styrene (PMS) microgels are applied as model fillers of definite size (d = 100 nm) with a very narrow distribution width. Since these model fillers consist of spherical particles with $\Phi_p = 1$, no disturbing influence of mixing severity on Φ_p, as found e. g. for the SBR/N339 composites in Section 3.2.2, can appear. The scaling factors of the solid lines allow for an approximate estimation of the front factors of Equ. (30). It yields a typical apparent energy density $\overline{G}/d^3$ of filler-filler bonds of the order of 1 GPa, corresponding to an energy $\overline{G} \cong 10^{-12}$ J.

Fig. 39: Double logarithmic plot of the small strain storage modulus vs. filler volume fraction for a variety of carbon black filled composites, as indicated. The solid lines with slope 3.5 correspond to the prediction of Equ. (30). Data of butyl/N330 composites are taken from Ref. 28 (compare Fig. 2a).

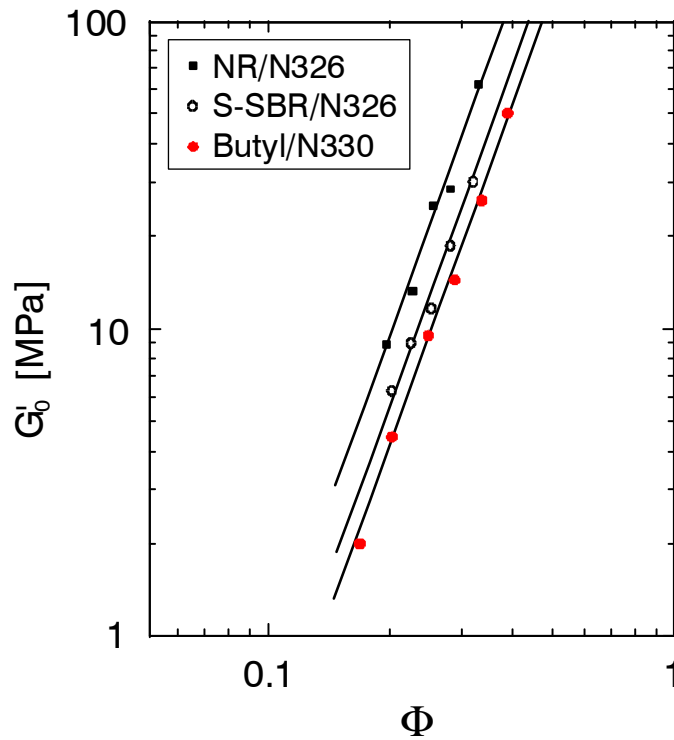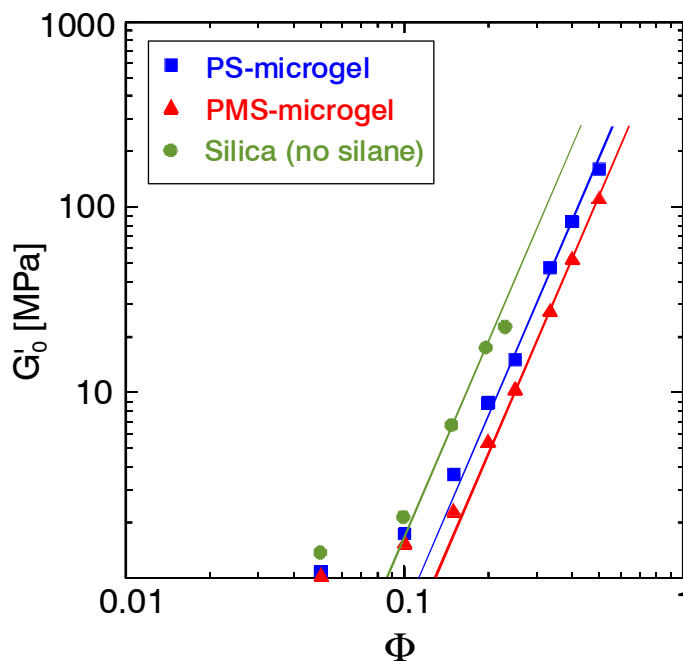**Fig. 40:** Double logarithmic plot of the small strain storage modulus vs. filler volume fraction for a variety of NR composites, as indicated. The solid lines with slope 3.5 correspond to the prediction of Equ. (30) [158,159].

The predicted scaling behavior Equ. (30) is also found to be well fulfilled for carbon black suspensions in ethylene-vinyl-acetate copolymers [51]. Furthermore, it is confirmed by viscoelastic data obtained for S-SBR composites with highly cross-linked BR-microgels of various size (compare Appendix B).

Equ. (30) describes the small strain modulus G'_0 as product of a local elastic constant $\overline{G}/d^3$ of filler-filler bonds and a geometrical factor, considering the structure of the filler network. Accordingly, the temperature- or frequency dependency of G'_0 is determined by the bending-twisting energy $\overline{G}$ of the filler-filler bonds, which is controlled by the bound rubber phase around the filler clusters. Coming back to the model of filler-filler bonds developed in Section 4.3 and depicted in Fig. 33, the energy in a strained bond is primary stored in a nanoscopic bridge of immobilized, glassy polymer between the filler particles, implying that the temperature- or frequency dependence of G'_0 is given by that of the glassy polymer. Consequently, for highly filled rubbers above the glass transition temperature, we expect an Arrhenius temperature behavior typical for polymers in the glassy state. This is in agreement with experimental findings [26-28].

We finally note that the decomposition of G'_0 into an local elastic constant and a geometrical factor implies that the same form as Equ. (30) must hold also for the loss modulus G''_0. This follows from the fact that in the linear viscoelastic regime any geometrical factor must act on the real and imaginary part of the complex modulus in the same way. Otherwise, the Kramers-Kronig relations, indicative for linear systems, can not be fulfilled [160]. From experimental data this is not always obvious, since the relatively small phase angle at small strain amplitudes can not be estimated as accurate as the norm of the modulus. In particular, the viscoelastic data of Payne [28] on butyl/N330-composites, depicted in Fig. 2b, show that the tan δ at small strain is almost independent of filler loading, implying that in the linear regime storage and loss modulus transform with the same geometrical factor.

5.2. Stress softening and filler-induced hysteresis

5.2.1 Strength and fracture of filler clusters in elastomers

So far, we have considered the elasticity of filler networks in elastomers and its reinforcing action at small strain amplitudes, where no fracture of filler-filler bonds appears. With increasing strain, a successive breakdown of the filler network takes place and the elastic modulus decreases rapidly if a critical strain amplitude is exceeded (Fig. 42). For a theoretical description of this behavior, the ultimate properties and fracture mechanics of CCA-filler clusters in elastomers have to be evaluated. This will be a basic tool for a quantitative understanding of stress softening phenomena and the role of fillers in internal friction of reinforced rubbers.

The failure- or yield strain ε_F of filler clusters in elastomers can be estimated by referring to the elasticity model of flexible chains with tension- and bending-twisting energy terms, as introduced above. According to this model, a single cluster corresponds to a series of two molecular springs: a soft one, representing the bending-twisting mode, and a stiff one, representing the tension mode. This mechanical equivalence is illustrated in Fig. 41.
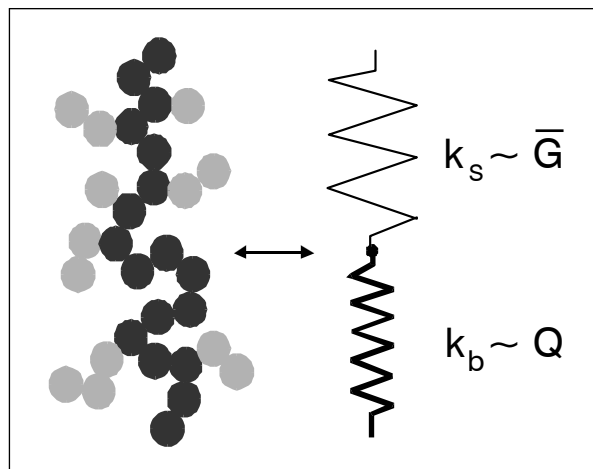
Fig. 41: Schematic view demonstrating the mechanical equivalence between a filler cluster and a series of soft and stiff molecular springs, representing bending-twisting- and tension deformation of filler-filler bonds, respectively.

On the one side, the soft spring with force constant $k_s \sim \overline{G}$ governs the elasticity of the whole system, provided that the deformation of the stiff spring can be neglected. On the other side, the stiff spring impacts the fracture behavior of the system, since it considers the longitudinal deformation and hence, separation of filler-filler bonds. The cluster breaks down, when a critical separation of bonded filler

particles is exceeded, i. e. if the failure strain ε_b of filler-filler bonds is reached. The failure strain ε_F of the filler cluster is then determined by the stress equilibrium between the two springs, which reads in the case of large clusters with $k_b \gg k_S$:

$$\varepsilon_F = \left(1 + \frac{k_b}{k_s}\right)\varepsilon_b \approx \frac{Q\varepsilon_b}{\kappa \overline{\overline{G}}}\left(\frac{\xi}{d}\right)^{2+d_{f,B}} \tag{31}$$

Here, $k_b = Q/d^2$ is the force constant of longitudinal deformations of filler-filler bonds and k_S is the bending-twisting force constant of the cluster, which is given by Equ. (28). From Equ. (31) one finds that the yield strain of a filler cluster depends on the ratio between the elastic constants $Q/\overline{G}$ and increases with the cluster size ξ according to a power law. Consequently, larger clusters show a higher extensibility than smaller ones, due to the ability to bend and twist around the bonds. This kind of elastic behavior of filler clusters and the dependence of strength on cluster size implies a high flexibility of filler clusters in strained rubbers. It plays a crucial role in rubber reinforcement even up to large strains. In particular, the Payne effect, shown e. g. in Figs. 2 and 42, can be modeled by referring to a specific size distribution of clusters in the filler network and assuming a successive breakdown of filler clusters with increasing strain [56]. Then, the broadness of the transition regime of the storage modulus (about three decades of strain) reflects the width of the size distribution of clusters in the filler network.
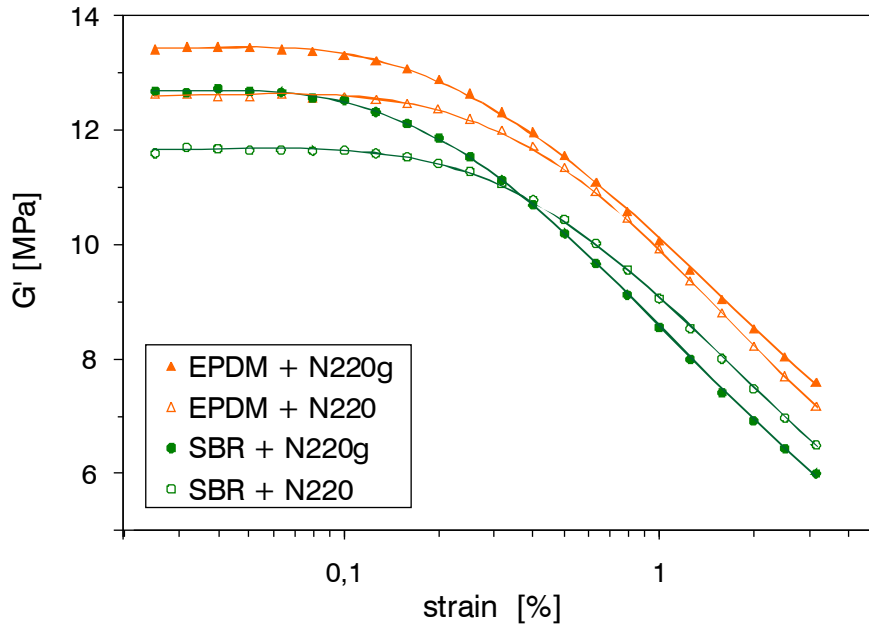

Fig. 42: Strain dependency of the storage modulus at 20 °C of cross-linked S-SBR- and EPDM composites filled with 50 phr N220 and graphitized N220g, respectively.

Equs. (29) - (31) allow for a qualitative analysis of the transition of the elastic modulus from the small strain plateau value to the high strain non-linear behavior. This transition becomes apparent in Fig. 42, showing the strain dependent storage modulus of EPDM- and S-SBR composites filled with the same amount of graphitized and non-graphitized N220, respectively. Since in first approximation the morphology of primary carbon black aggregates can considered to be not much different, i. e. d = constant and Φ_p = constant, Equs. (29) and (30) imply that the cluster size ξ is roughly the same for all four systems. Hence, the differences observed in the critical strain amplitude ε_{app}, where non-linearity appears, and those in the small strain modulus G'_0 have to be related to differences in the elastic constants Q and $\overline{G}$. Due to Equ. (29), the higher values of G'_0 for the EPDM-composites and the systems with the graphitized black, respectively, indicate stiffer filler-filler bonds with larger values of the bending-twisting constant $\overline{G}$. Equ. (31) implies that the lower values of ε_{app} for the systems with the graphitized black can partly be related to the same effect, i. e. larger values of $\overline{G}$, provided $\varepsilon_{app} \sim \varepsilon_F$ is assumed. However, a closer analysis shows that the shift factor describing the variation of ε_{app} is significantly larger than that of G'_0. This emphasizes that the systems with the graphitized black exhibit smaller values of the tension energy Q of filler-filler bonds, reflecting a lower interaction strength between the particles.

These results can be well understood, if the model of filler-filler bonds developed in Section 4.3 is considered, again. It implies that the local elastic constants Q and $\overline{G}$ are controlled by the rubber phase around fillers, i. e. they are attributed to the amount of bound rubber and its influence on the spacing of contact gaps. The elastic constant Q is also affected by the van der Waals force between contacting filler particles, representing the driving force of filler aggregation. A comparison of the S-SBR-systems shown in Fig. 42 and the annealed systems in Fig. 35 makes clear that cross-linking has no pronounced effect on the vicoelastic data, though the difference between both filler types decreases during cross-linking and the cross-over point is shifted to somewhat smaller strain amplitudes. Note that apart from cross-linking, the systems have been prepared with respect to the same procedure, but the measurement temperature is different.

For analyzing the fracture behavior of filler clusters in strained rubbers, it is necessary to estimate the strain of the clusters in dependence of the external strain of the samples. In the case of small and medium strains, considered above, both strain amplitudes in spatial direction μ are equal ($\varepsilon_{A,\mu} = \varepsilon_\mu$), because the stress is transmitted directly between neighboring clusters of the filler network. For strain amplitudes larger than about 1 %, this is no longer the case, since a gel-sol transition of the filler network takes place with increasing strain and the stress of the filler clusters is transmitted by the rubber matrix (compare Appendix B and Ref. 154). At large strains, the local strain $\varepsilon_{A,\mu}$ of a filler cluster in a strained rubber matrix can

be determined with respect to the external strain ε_μ, if a stress equilibrium between the strained cluster and the rubber matrix is assumed ($\varepsilon_{A,\mu} G_A(\xi_\mu) = \hat{\sigma}_{R,\mu}(\varepsilon_\mu)$). With Equ. (29) this implies:

$$\varepsilon_{A,\mu}(\varepsilon_\mu) = \frac{d^3}{\kappa \overline{\overline{G}}} \left(\frac{\xi_\mu}{d}\right)^{3+d_{f,B}} \hat{\sigma}_{R,\mu}(\varepsilon_\mu) \tag{32}$$

Here, ξ_μ denotes the cluster size in spatial direction μ of the main axis system and $\hat{\sigma}_{R,\mu}(\varepsilon_\mu)$ is the norm of the relative stress of the rubber with respect to the initial stress at the beginning of each strain cycle, where $\partial \varepsilon_\mu / \partial t = 0$:

$$\hat{\sigma}_{R,\mu}(\varepsilon_\mu) \equiv \left| \sigma_{R,\mu}(\varepsilon_\mu) - \sigma_{R,\mu}(\partial \varepsilon_\mu / \partial t = 0) \right| \tag{33}$$

The application of this normalized, relative stress in Equ. (32) is essential for a constitutive formulation of cyclic cluster breakdown and re-aggregation during stress-strain cycles. It implies that the clusters are stretched in spatial directions with $\partial \varepsilon_\mu / \partial t > 0$, only, since $\varepsilon_{A,\mu} \geq 0$ holds due to the norm in Equ. (33). In the compression directions with $\partial \varepsilon_\mu / \partial t < 0$ re-aggregation of the filler particles takes place and the clusters are not deformed. An analytical model for the large strain non-linear behavior of the nominal stress $\sigma_{R,\mu}(\varepsilon_\mu)$ of the rubber matrix will be considered in the next section.

A comparison of Equs. (31) and (32) makes clear that for large deformations, when the stress of the clusters is transmitted by the rubber matrix, the strain $\varepsilon_{A,\mu}$ of the clusters increases faster with their size ξ_μ then the failure strain $\varepsilon_{F,\mu}$. Accordingly, with increasing strain the large clusters in the system break first followed by the smaller ones. The maximum size ξ_μ of clusters surviving at exposed external strain ε_μ is estimated by the stress equilibrium between the rubber matrix and the failure stress $\sigma_{F,\mu} = \varepsilon_{F,\mu} G_A(\xi_\mu)$ of the clusters:

$$\xi_\mu(\varepsilon_\mu) = \frac{Q \varepsilon_b}{d^2 \hat{\sigma}_{R,\mu}(\varepsilon_\mu)} \tag{34}$$

This allows for an evaluation of the stress contribution of the stretched filler clusters if the size distribution of the clusters in the system is known. Note that for small deformations, where $\varepsilon_{A,\mu} = \varepsilon_\mu$ holds, the situation is different, since $\varepsilon_{A,\mu}$ is independent of cluster size. Then, the small clusters break first followed by the larger ones.

5.2.2 Free energy density of reinforced rubbers

Starting from a particular size distribution of kinetically aggregated filler clusters in a rubber matrix, we can now formulate the free energy density of a highly strained sample by assuming the following microscopic scenario. With increasing strain of a virgin sample, a successive breakdown of filler clusters takes place under the exposed stress of the bulk rubber. This process begins with the largest clusters and continues up to a minimum cluster size $\xi_{\mu,min}$ in spatial direction μ, which is given by Equ. (34) evaluated for the maximum stress of the rubber matrix $\hat{\sigma}_{R,\mu}(\varepsilon_{\mu,max})$ reached at maximum external strain $\varepsilon_{\mu,max}$. During the back-cycle, complete re-aggregation takes place, but the filler-filler bonds that are formed after once being broken are significantly weaker and softer than the original annealed ones. For subsequent stress-strain cycles of a pre-conditioned sample, two micro-mechanical mechanisms of rubber reinforcement are distinguished:

(i) Hydrodynamic reinforcement of the rubber matrix by the fraction of rigid filler clusters with strong filler-filler bonds that have not been broken during previous deformations.

(ii) Cyclic breakdown and re-aggregation of the residual fraction of more fragile filler clusters with weaker filler-filler bonds.

The fraction of rigid filler clusters decreases with increasing pre-strain, while the fraction of fragile filler clusters increases. The decomposition into rigid and fragile filler cluster units is illustrated in Fig. 43.
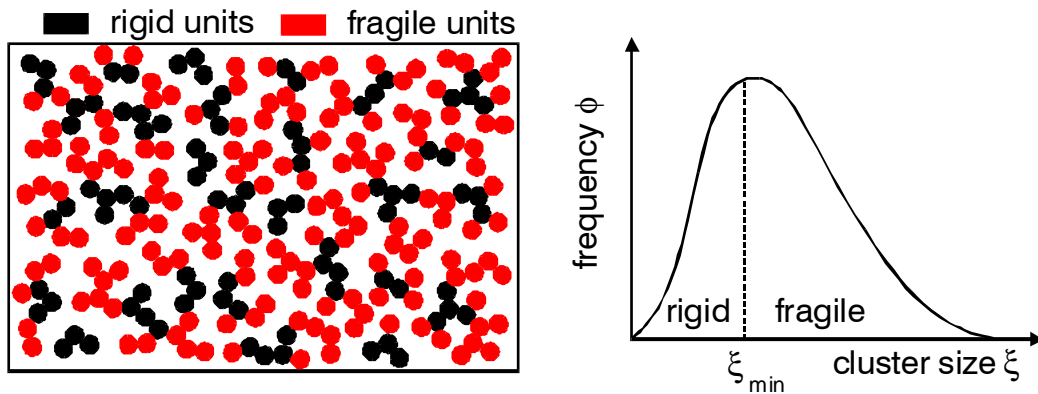
Fig. 43: Schematic view of the decomposition of filler clusters in rigid and fragile units for pre-conditioned samples. The right side shows the cluster size distribution with the pre-strain dependent boundary size ξ_{min}.

The fragile filler clusters with soft bonds bend substantially in the stress field of the rubber, implying that their contribution to hydrodynamic reinforcement is relatively small. The mechanical action of the fragile filler clusters refers primary to a viscoelastic effect, since any type of cluster that is stretched in the stress field of the

rubber stores energy that is dissipated when the cluster breaks. This mechanism leads to a filler-induced viscoelastic contribution to the total stress that impacts the internal friction of filler rubber samples, significantly. Note that this kind of viscoelastic response is present also in the limit of quasi-static deformations, where no explicit time dependency of the stress-strain cycles is taken into account.

According to these considerations, we propose the following dynamic flocculation model of rubber reinforcement. For quasi-static, cyclic deformations of filler reinforced rubbers the total free energy density consists of two contributions:

$$W(\varepsilon_\mu) = W_R(\varepsilon_\mu) + W_A(\varepsilon_\mu) \tag{35}$$

The first addend is the equilibrium energy density stored in the extensively strained rubber matrix, which includes hydrodynamic reinforcement by a fraction of rigid filler clusters (see below). The second addend considers the energy stored in the substantially strained fragile, soft filler clusters:

$$W_A(\varepsilon_\mu) = \sum_\mu^{\partial\varepsilon_\mu/\partial t > 0} \frac{1}{2d} \int_{\xi_{\mu,min}}^{\xi_\mu(\varepsilon_\mu)} G_A(\xi_\mu') \, \varepsilon_{A,\mu}^2(\xi_\mu', \varepsilon_\mu) \, \phi(\xi_\mu') \, d\xi_\mu' \tag{36}$$

Here, $\phi(\xi_\mu)$ is the normalized size distribution of the CCA-clusters in spatial direction μ of the main axis system. It can be evaluated by referring to Smoluchowski's equation for the kinetics of irreversible cluster-cluster aggregation of colloids [8,161,162]. In the case of large clusters (and large times), one can obtain a reduced form of the size distribution function [8]:

$$\phi(\xi_\mu) = \frac{4d}{<\xi_\mu>} \left(\frac{\xi_\mu}{<\xi_\mu>}\right)^{-2\Omega} \exp-\left(\frac{(1-2\Omega)\xi_\mu}{<\xi_\mu>}\right) \quad \text{for } \mu = 1, 2, 3 \tag{37}$$

For $\Omega < 0$, this distribution function is peaked around a maximum cluster size $(2\Omega/(2\Omega-1))<\xi_\mu>$, where $<\xi_\mu>$ is the mean cluster size. $2\Omega = \alpha' + d_f^{-1}$ is a parameter describing details of the aggregation mechanism, where α' is an exponent considering the dependency of the diffusion constant Δ of the clusters on its particle number, i. e. $\Delta \sim N_A^{\alpha'}$. This exponent is in general not very well known. In a simple approach, the particles in the cluster can assumed to diffusion independent from each other, as e. g. in the Rouse model of linear polymer chains. Then, the diffusion constant varies inversely with the number of particles in the cluster ($\Delta \sim N_A^{-1}$), implying $2\Omega = -0.44$ for CCA-clusters with fractal dimension $d_f = 1.8$.

The sum in Equ. (36) is taken over the stretching directions with $\partial\varepsilon_\mu/\partial t > 0$, only. This corresponds to the assumption that clusters are strained and successively broken in stretching directions, while healing of the clusters takes place in the compression directions. It insures that a cyclic breakdown and re-aggregation of clusters can be described. The integration in Equ. (36) is performed over the fraction of fragile filler clusters that are not broken at exposed strain ε_μ of the actual cycle (Equ. 34). The clusters smaller than $\xi_{\mu,min}$, representing the fraction that survived the first deformation cycle, are not considered in Equ. (36). Due to the stiff nature of their filler-filler bonds, referring to the bonds in the virgin state of the sample, these clusters behave rigid and give no contribution to the stored energy. Instead, they dominate the hydrodynamic reinforcement of the rubber matrix. This is specified by the strain amplification factor X, which relates the external strain ε_μ of the sample to the internal strain ratio λ_μ of the rubber matrix:

$$\lambda_\mu = 1 + X\,\varepsilon_\mu \tag{38}$$

In the case of a pre-conditioned sample and for strains smaller than the previous straining ($\varepsilon_\mu < \varepsilon_{\mu,max}$), the strain amplification factor is constant in stretching directions with $\partial\varepsilon_\mu/\partial t > 0$ and determined by $\varepsilon_{\mu,max}$ ($X = X(\varepsilon_{\mu,max})$). For the compression directions with $\partial\varepsilon_\mu/\partial t < 0$, the strain dependency of X is determined by the condition of constant volume. This will be specified in Section 5.2.4.

By applying a relation derived by Huber and Vilgis [64,65] for the strain amplification factor of overlapping fractal clusters at large filler concentrations, $X(\varepsilon_{\mu,max})$ can be evaluated by averaging over the size distribution of rigid clusters in all space directions. In the case of pre-conditioned samples this yields:

$$X(\varepsilon_{\mu,max}) = 1 + c\left(\frac{\Phi}{\Phi_p}\right)^{\frac{2}{3-d_f}} \sum_{\mu=1}^{3} \frac{1}{d}\left(\int_0^{\xi_{\mu,min}}\left(\frac{\xi'_\mu}{d}\right)^{d_w-d_f}\phi\left(\xi'_\mu\right)d\xi'_\mu + \int_{\xi_{\mu,min}}^{\infty}\phi\left(\xi'_\mu\right)d\xi'_\mu\right) \tag{39}$$

Here, c is a universal scaling factor of order one and $d_w \approx 3.1$ [23] is the anomalous diffusion exponent on fractal CCA-clusters. The first addend in Equ. (39) considers the contribution of the rigid clusters. The second addend takes into account the hydrodynamic amplification of the primary aggregates of the fragile, soft clusters that contribute to the strain amplification factor, even if all rigid clusters are broken. In the limit of large strain values $\varepsilon_{\mu,max}$, where all clusters are broken and ξ_μ approaches the primary aggregate size d, the sum in Equ. (39) takes the fixed value three. Then, the amplification factor depends on the effective volume fraction Φ/Φ_p of primary aggregates, only, similar as in the Guth-Gold approach [63].

For the first deformation of virgin samples X depends on the external strain ε_μ, since $\varepsilon_\mu \equiv \varepsilon_{\mu,max}$ in that case. Accordingly, $X(\varepsilon_{\mu,max})$ is considered to be a variable in that case, which is obtained by performing the integration from zero up to the pre-strain dependent cluster size $\xi_{\mu,min}(\varepsilon_{\mu,max})$ as determined by Equ. (34). However, note that the elastic constant Q' and yield strain ε_b' of virgin filler-filler bonds have to be used in this evaluations that differ from the corresponding quantities Q and ε_b of damaged bonds introduced in the previous section. From the basic principles of the developed model we expect the strength of virgin filler-filler bonds to be larger than the strength of damaged bonds, i. e. the yield stress fulfills $Q\,\varepsilon_b/d^3 < Q'\,\varepsilon_b'/d^3$.

An important role in the present model is played by the strongly non-linear elastic response of the rubber matrix that transmits the stress between the filler clusters. We refer here to an extended tube model of rubber elasticity, which is based on the following fundamental assumptions: The network chains in a highly entangled polymer network are heavily restricted in their fluctuations due to packing effects. This restriction is described by virtual tubes around the network chains that hinder the fluctuation. When the network elongates, these tubes deform non-affinely with a deformation exponent $\nu = \frac{1}{2}$. The tube radius d_μ in spatial direction μ of the main axis system depends on the deformation ratio λ_μ as follows:

$$d_\mu = d_o\,\lambda_\mu^{\,\nu} \tag{40}$$

where d_o is the tube radius in the non-deformed state. The assumption of the non-affine tube deformation ($\nu = \frac{1}{2}$) is essential. It was initially derived based upon fundamental molecular statistical calculations [57,163,164] and later on confirmed by applying scaling arguments [77,78,165]. Experimental evidence of non-affine tube deformations according to Equ. (40) is provided by neutron scattering of strained rubbers [166] or stress-strain measurements at swollen networks [167].

An extension of the non-affine tube model for applications up to large strains is obtained by considering that the network chains have a finite length and the stress in the network becomes infinitely large, when the chain sections between two subsequent trapped entanglements are stretched fully. The trapping of chain entanglements by two cross-link points prevents the sliding of the chains across each other under extension, implying that the entanglement becomes an elastically effective network junction. The free energy density of the extended, non-Gaussian tube model with non-affine tube deformation is then as follows [75-78,168]:

$$W_R(\varepsilon_\mu) = \frac{G_c}{2} \left\{ \frac{\left(\sum_{\mu=1}^{3} \lambda_\mu^2 - 3\right)\left(1 - \frac{T_e}{n_e}\right)}{1 - \frac{T_e}{n_e}\left(\sum_{\mu=1}^{3} \lambda_\mu^2 - 3\right)} + \ln\left[1 - \frac{T_e}{n_e}\left(\sum_{\mu=1}^{3} \lambda_\mu^2 - 3\right)\right]\right\} +$$

$$+ 2G_e\left(\sum_{\mu=1}^{3} \lambda_\mu^{-1} - 3\right) \tag{41}$$

Here, n_e is the number of statistical chain segments between two successive entanglements and T_e is the trapping factor ($0<T_e<1$), which characterizes the portion of elastically active entanglements. The first bracket term of Equ. (41) considers the constraints due to inter-chain junctions, with an elastic modulus G_c proportional to the density of network junctions. The second addend is the result of tube constraints, whereby G_e is proportional to the entanglement density μ_e of the rubber. The parenthetical expression in the first addend takes into account the finite chain extensibility by referring to a proposal of Edwards and Vilgis [169]. For the limiting case $n_e/T_e = \sum \lambda_\mu^2 - 3$, a singularity is obtained for W_R. This happens when the chains between successive trapped entanglements are fully stretched out. It makes clear that the approach in Equ. (41) characterizes trapped entanglements as some kind of physical cross-links (slip-links) that dominate the extensibility of the network due to the larger number of entanglements as compared to chemical cross-links. In the limit $n_e \to \infty$ the original Gaussian formulation of the non-affine tube model, derived by Heinrich et al. [57] for infinite long chains, is recovered.

The trapping factor T_e increases as the cross-link density increases, whereas n_e and G_e - as terms that are specific to the polymer - are to a great extent independent of cross-link density. For the cross-link and tube constraint moduli, the following relations to molecular network parameters hold:

$$G_c = A_c \, \nu_{mech} \, k_B T \tag{42}$$

$$G_e = \frac{\rho \, N_a \, l_s^2 \, k_B T}{4\sqrt{6} \, M_s \, d_o^2} \tag{43}$$

Here, ν_{mech} is the mechanically effective chain density, $A_c \approx 0.67$ [170] is a microstructure factor describing fluctuations of network junctions, N_a is Avogadros number, ρ mass density, M_s and l_s molar mass and length of statistical segments, respectively, k_B the Boltzmann constant and T absolute temperature.

From Equ. (41) the nominal stress $\sigma_{R,\mu}$ that relates the force F_μ in spatial direction μ to the initial cross section $A_{o,\mu}$ is found by differentiation, $\sigma_{R,\mu} = \partial W_R / \partial \lambda_\mu$. For uniaxial extensions of unfilled rubbers ($X = 1$) with $\lambda_1 = \lambda$, $\lambda_2 = \lambda_3 = \lambda^{-1/2}$ the following relation can be derived:

$$\sigma_{R,1} = G_c\left(\lambda - \lambda^{-2}\right)\left\{\frac{1 - T_e/n_e}{\left(1 - \dfrac{T_e}{n_e}(\lambda^2 + 2/\lambda - 3)\right)^2} - \right.$$

$$\left. - \frac{T_e/n_e}{1 - \dfrac{T_e}{n_e}(\lambda^2 + 2/\lambda - 3)}\right\} + 2G_e(\lambda^{-1/2} - \lambda^{-2}) \tag{44}$$

For equi-biaxial extensions with $\lambda_1 = \lambda_2 = \lambda$, $\lambda_3 = \lambda^{-2}$ one finds for the nominal stress:

$$\sigma_{R,1} = G_c\left(\lambda - \lambda^{-5}\right)\left\{\frac{1 - T_e/n_e}{\left(1 - \dfrac{T_e}{n_e}(2\lambda^2 + \lambda^{-4} - 3)\right)^2} - \right.$$

$$\left. - \frac{T_e/n_e}{1 - \dfrac{T_e}{n_e}(2\lambda^2 + \lambda^{-4} - 3)}\right\} + 2G_e(\lambda - \lambda^{-2}) \tag{45}$$

In the case of a pure-shear deformation with $\lambda_1 = \lambda$, $\lambda_2 = 1$ and $\lambda_3 = \lambda^{-1}$ one obtains:

$$\sigma_{R,1} = G_c\left(\lambda - \lambda^{-3}\right)\left\{\frac{1 - T_e/n_e}{\left(1 - \dfrac{T_e}{n_e}(\lambda^2 + \lambda^{-2} - 2)\right)^2} - \right.$$

$$\left. - \frac{T_e/n_e}{1 - \dfrac{T_e}{n_e}(\lambda^2 + \lambda^{-2} - 2)}\right\} + 2G_e(1 - \lambda^{-2}) \tag{46}$$

By fitting experimental data for different deformation modes to these functions, the three model parameters of unfilled polymer networks G_c, G_e and n_e/T_e can be determined. The validity of the concept can be tested if the estimated fitting parameters for the different deformation modes are compared. A "plausibility criterion" for the proposed model is formulated by demanding that all deformation modes can be described by a single set of network parameters. The result of this plausibility test is depicted in Fig. 44, where stress-strain data of unfilled NR-samples are shown for the three different deformation modes considered above. Obviously, the material parameters found from the fit to the uniaxial data provide a rather good prediction for the two other modes. The observed deviations are within the range of experimental errors.
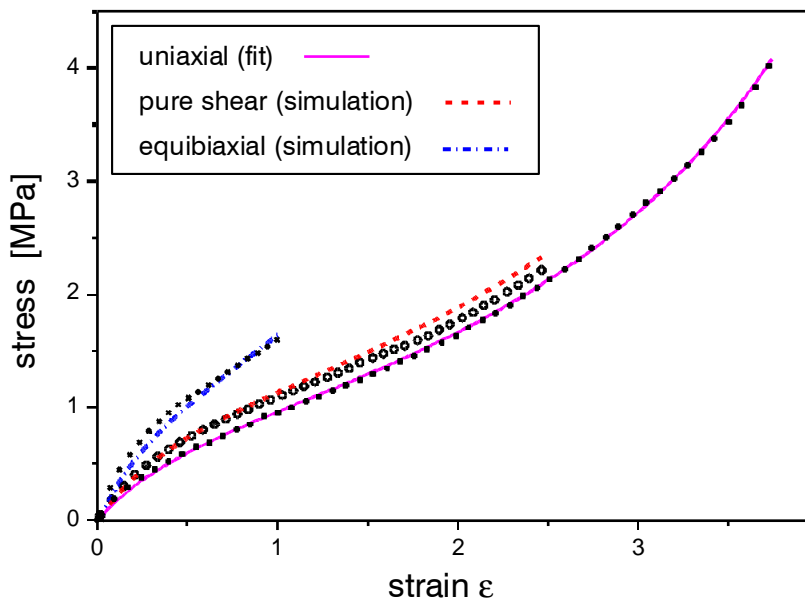

Fig. 44: Quasi-static stress-strain data (symbols) and simulation curves (Equs. (44)-(46)) of an unfilled NR for three deformation modes. The model parameters are found from a fit to the uniaxial data ($G_c = 0.43$ MPa, $G_e = 0.2$ MPa, $n_e/T_e = 68$).

It should be pointed out that the material parameter G_e can be determined in principle more precisely by means of equi-biaxial measurements than by uniaxial measurements. This is due to the fact that the first addend of the G_e-term in Equ. (45) increases linear with λ. This behavior results from the high lateral contraction on the equi-biaxial extension ($\lambda_3 = \lambda^{-2}$). It postulates a close dependency of the equi-biaxial stress on the tube constraint modulus, since G_c and G_e contribute nearly equally to stress, also at larger extensions. For the uniaxial extensions described in Equ. (44) this is not the case. Here, the tube constraints lead to significant effects only in the region of lower extensions, since the G_e-term in Equ. (44) approaches

zero as the λ values increase. Nevertheless, the experiments can be carried out more easily in the uniaxial case, and as a result, more reliable experimental data can be obtained.

For practical applications, the parameter G_e can also be determined from the value of the plateau modulus G_N, since the relationship $G_e \approx \frac{1}{2} G_N$ applies in accordance with the tube model. This implies that the parameter G_e is not necessary a fit parameter but rather it is specified by the microstructure of the rubber used. Note that the fit value $G_e = 0.2$ MPa obtained in Fig. 44 is in fair agreement with the above relation, since $G_N \approx 0.58$ MPa is found for uncross-linked NR-melts [171].

A comparison of the predictions of the extended tube model to stress-strain data of unfilled rubbers offered good agreement for various polymers and cross-linking systems [75-78,167,170,172,173]. Further confirmation of the non-affine tube approach was obtained in recent investigations considering mechanical stress-strain data and a transversal NMR-relaxation analysis of differently prepared NR-networks [168]. A brief review of the molecular statistical foundations of tube-like topological constraints in strained polymer networks is found in Appendix F, where the path integral formulation of rubber elasticity is briefly reviewed. In the second part of Appendix F, a first attempt for considering stress softening phenomena of filled rubbers on the basis of the extended tube model is formulated. Subsequent investigations have shown that a constitutive formulation of stress softening fulfilling the "plausibility criterion" can not be achieved in this simplified approach [89]. In the following section we will see that the present extended model, as developed above, passes the "plausibility test" fairly well also for filled rubbers. The important point lies in the determination of the topological tube constraint modulus G_e according to its physical value $G_e \approx \frac{1}{2} G_N$.

5.2.3 Stress-strain cycles at large strain - The Mullins effect

For filler reinforced rubbers, both contributions of the free energy density Equ. (35) have to be considered and the strain amplification factor X, given by Equ. (39), differs from one. The nominal stress contributions of the cluster deformation are determined by $\sigma_{A,\mu} = \partial W_A / \partial \varepsilon_{A,\mu}$, where the sum over all stretching directions, that differ for the up- and down cycle, have to be considered. For uniaxial deformations $\varepsilon_1 = \varepsilon$, $\varepsilon_2 = \varepsilon_3 = (1+\varepsilon)^{-1/2}-1$ one obtains a positive contribution to the total nominal stress in stretching direction for the up-cycle if Equs. (29) through (36) are used:

$$\sigma_{0,1}^{up}(\varepsilon) = \sigma_{R,1}(\varepsilon) + \hat{\sigma}_{R,1}(\varepsilon) \int\limits_{\frac{Q\,\varepsilon_b}{d^3\hat{\sigma}_{R,1}(\varepsilon_{max})}}^{\frac{Q\,\varepsilon_b}{d^3\hat{\sigma}_{R,1}(\varepsilon)}} \phi(x_1)\, dx_1 \qquad (47)$$

with the abbreviations:

$$\hat{\sigma}_{R,1}(\varepsilon) = \left| \sigma_{R,1}(\varepsilon) - \sigma_{R,1}(\varepsilon_{min}) \right| \tag{48}$$

and $x_1 = \xi_1/d$. For the down-cycle in the same direction one finds a negative contribution to the total stress:

$$\sigma_{0,1}^{down}(\varepsilon) = \sigma_{R,1}(\varepsilon) - 2\tilde{\sigma}_{R,1}(\varepsilon) \int_{\frac{Q\varepsilon_b(1+\varepsilon_{min})^{-3/2}}{2d^3\tilde{\sigma}_{R,1}(\varepsilon_{min})}}^{\frac{Q\varepsilon_b(1+\varepsilon)^{-3/2}}{2d^3\tilde{\sigma}_{R,1}(\varepsilon)}} \phi(x_1)dx_1 \tag{49}$$

with the abbreviation:

$$\tilde{\sigma}_{R,1}(\varepsilon) = \left| \sigma_{R,1}(\varepsilon) - \left(\frac{1+\varepsilon_{max}}{1+\varepsilon}\right)^{3/2} \sigma_{R,1}(\varepsilon_{max}) \right| \tag{50}$$

The negative sign in Equ. (49) results from the norm, implying e. g. for the relative nominal stresses in direction 1 and 2:

$$\hat{\sigma}_{R,2}(\varepsilon) = 2(1+\varepsilon)^{3/2}\,\tilde{\sigma}_{R,1}(\varepsilon) \tag{51}$$

This is in contrast to the transformation behavior of the nominal stresses of the rubber matrix with a negative sign:

$$\sigma_{R,2}(\varepsilon) = -2(1+\varepsilon)^{3/2}\sigma_{R,1}(\varepsilon) \tag{52}$$

Note that the different choice of the extrema with $\partial\varepsilon_\mu/\partial t = 0$ in Equ. (48) and (50) are due to the fact that an up-cycle begins at $\varepsilon = \varepsilon_{min}$, but a down-cycle begins at $\varepsilon = \varepsilon_{max}$. As a rule, the relative stresses in the lower boundaries of the integrals in Equs. (47) and (49) have to be chosen in a way that they reach their maximum values, implying that all fragile clusters are broken and $\xi_\mu = \xi_{\mu,min}$. In deriving Equ. (49) we assumed an isotropic cluster size distribution, i. e. $\phi(x_1) = \phi(x_2) = \phi(x_3)$. This appears reasonable, since $\phi(x_\mu)$ refers to the size distribution of clusters in the virgin, unstrained state. However, from the basic concept of cluster breakdown in the stretching direction and re-aggregation in the compression direction, respectively, it is clear that the size distribution of the filler clusters during the deformation cycles is strongly anisotropic. It leads to the characteristic hysteresis of a pre-strained sample,

as given by Equs. (47) through (50), even in the case of a quasi-static deformation at infinite slow strain rates.

Figs. 45a through 45c show an adaptation of the developed model to uniaxial stress-strain data of a pre-conditioned S-SBR-sample filled with 40 phr N220. The fits are obtained for the third stretching cycles at various pre-strains by referring to Equs. (38), (44) and (47) with different but constant strain amplification factors $X = X_{max}$ for every pre-strain. For these fits the permanent set of the samples has been compensated by shifting all experimental stress-strain curves to the origin. In so far we consider an "idealized Mullins effect" here, which does not include the permanent set of the samples. For illustrating the fitting procedure, the adaptation is performed in three steps. Since the evaluation of the nominal stress contribution of the strained filler clusters by the integral in Equ. (47) requires the nominal stress $\sigma_{R,1}$ of the rubber matrix, this quantity is developed in the first step shown in Fig. 45a. It is obtained by demanding an intersection of the simulated curves according to Equs. (38) and (44) with the measured ones at maximum strain of each strain cycle, where all fragile filler clusters are broken and hence the stress contribution of the strained filler clusters vanishes. The adapted polymer parameters are $G_c = 0.176$ MPa and $n_e/T_e = 100$, independent of pre-strain. According to the considerations at the end of Section 5.2.2, the tube constraint modulus is kept fixed at the rubber specific value $G_e = 0.2$
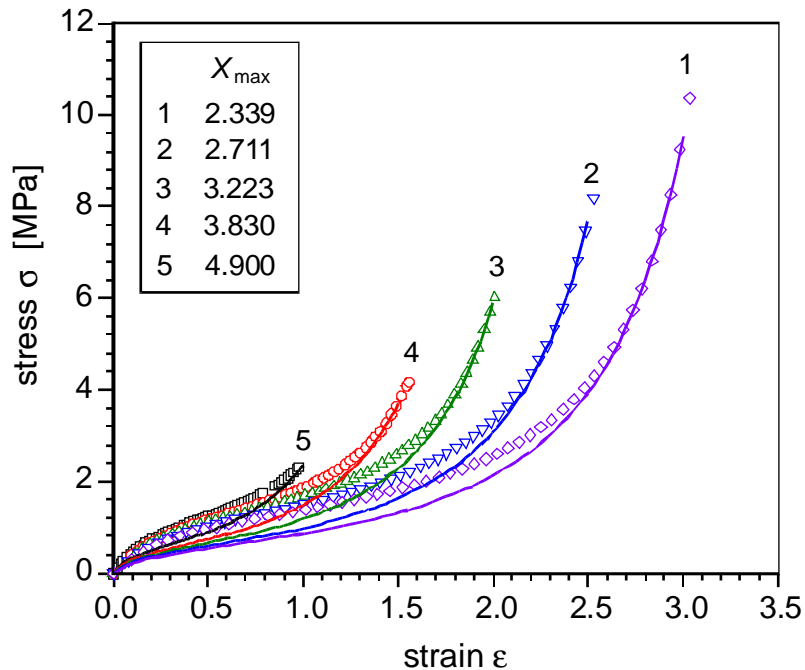

Fig. 45a: Quasi-static, uniaxial stress-strain data (symbols) of S-SBR samples (Buna VSL 2525-0) filled with 40 phr N220 at various pre-strains ε_{max} and simulation curves (lines) of the polymer contribution according to Equs. (38) and (44). The set of polymer parameters is found as $G_c = 0.176$ MPa, $G_e = 0.2$ MPa and $n_e/T_e = 100$.

MPa, determined by the plateau modulus $G_N \approx 0.4$ MPa [174,175] of the uncross-linked S-SBR-melt ($G_e = \frac{1}{2} G_N$). The adapted amplification factors X_{max} for the different pre-strains ($\varepsilon_{max} = 1, 1.5, 2, 2.5, 3$) are listed in the insert of Fig. 45a.

Fig. 45b (upper part) shows the residual stress contribution of the strained filler clusters for the different pre-strains, obtained by subtracting the polymer contributions (solid lines) from the experimental stress-strain data (symbols) of Fig. 45a. The resulting data (symbols) are fitted to the second addend of Equ. (47) (solid lines), whereby the size distribution of filler clusters Equ. (37), shown in the lower part of Fig. 45b, has been used.
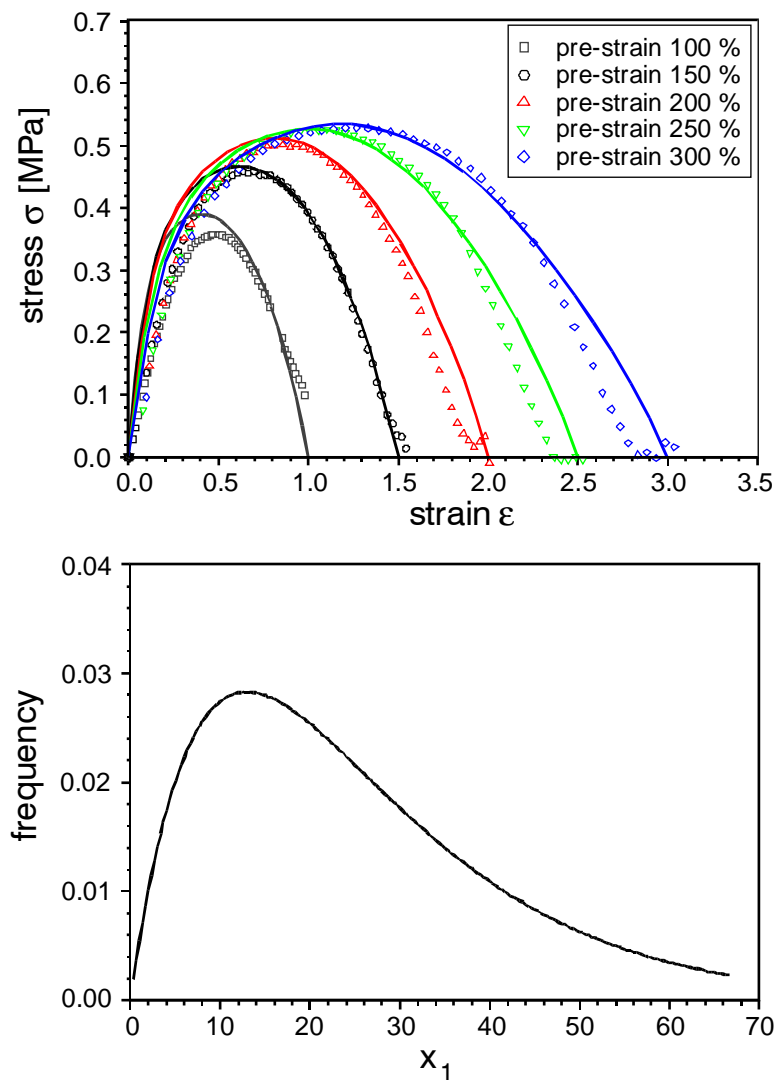

Fig. 45b: Stress contributions of the strained filler clusters for the different pre-strains (upper part), obtained by subtracting the polymer contributions from the experimental stress-strain data of Fig. 45a. The solid lines are adaptations with the integral term of Equ. (47) and the cluster size distribution Equ. (37), shown in the lower part. The obtained parameters of the filler clusters are $Q\varepsilon_b/d^3 = 24$ MPa, $<x_1> = 26$ and $\Omega = -0.5$.

85

The size distribution $\phi(x_1)$ is determined by the adapted mean cluster size $<x_1> \equiv <\xi_1/d> = 26$ and the pre-chosen distribution width $\Omega = -0.5$, which allows for an analytical solution of the integral in Equ. (47). The yield stress of damaged filler-filler bonds is found as $Q\varepsilon_b/d^3 = 24$ MPa. The different fit lines result from the different stress-strain curves $\sigma_{R,1}(\varepsilon)$ that enter the upper boundary of the integral in Equ. (47). Note that this integral, representing the contribution of the strained filler clusters to the total stress, becomes zero at $\varepsilon = \varepsilon_{max}$ for every pre-strain.

Fig. 45c shows the complete adaptation with Equ. (47) of the uniaxial stress-strain data, i. e. the sum of the two contributions shown in Figs. 45a and 45b. The fits for all pre-strained samples are very good in the large as well as the small strain regime, which is separately shown up to 150 % strain in the insert of Fig. 45c. Furthermore, beside the third stretching cycles at various pre-strains, the first stretching of the virgin sample is shown. It is compared to a simulation curve given by Equ. (47) with the above specified material parameters and a strain dependent amplification factors $X = X(\varepsilon_{max})$.
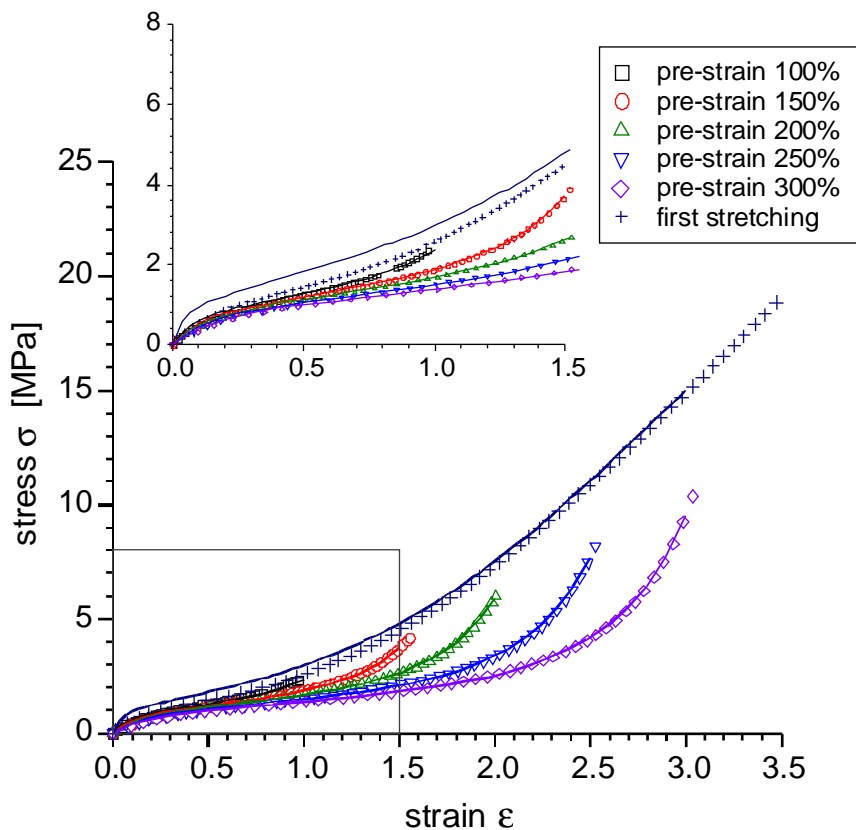

Fig. 45c: Quasi-static, uniaxial stress-strain data (symbols) of the S-SBR samples (Buna VSL 2525-0) with 40 phr N220 at various pre-strains ε_{max} and for the first stretching of the virgin sample, as indicated. The insert shows a magnification for the smaller strains. The lines are simulation curves with parameters specified in Figs. 45a and 45b.

Unfortunately, Equ. (39) can not simply be applied for an estimation of $X(\varepsilon_{max})$, since the upper boundary of the integral $\xi_\mu(\varepsilon)$ depends on $X(\varepsilon_{max})$ itself (Equ. (34)) and a general analytic solution of the integral is difficult to obtain. An iterative numerical procedure for the estimation of $X(\varepsilon_{max})$ according to Equ. (39) will be applied in the next section. Alternatively, as a first empirical approach, a power law dependency of the amplification factor X on a scalar strain variable E, involving the first deformation invariant $I_1(\varepsilon_\mu)$, is chosen here (compare Appendix F):

$$X(E) = X_\infty + (X_o - X_\infty)(1+E)^{-y} \tag{53}$$

with

$$E(\varepsilon_\mu) \equiv \left(\sum_{\mu=1}^{3} (1+\varepsilon_\mu)^2 - 3 \right)^{1/2} \tag{54}$$

Here, X_∞ and X_o are the strain amplification factors at infinite and zero strain, respectively, and y is an empirical exponent. An adaptation of this empirical function, Equ. (53), to the X_{max}-values obtained for the pre-strained samples shown in Fig. 45a delivers the parameters $X_o = 11.5$, $X_\infty = -1.21$ and $y = 0.8$, which are used for the simulation of the first stretching cycle shown in Fig. 45c.

A comparison of the experimental data for the first stretching cycle of the samples to the simulation curve in Fig. 45c shows no good agreement. Significant deviations are observed especially in the low strain regime, shown in the insert, where an extrapolation of the function X(E) is used. The reason for the deviations may partly lie in the application of the power law approximation Equ. (53) for X(E), instead of the micro-mechanically motivated Equ. (39). This may also lead to the unphysical negative value of X at extrapolated infinite strain ($X_\infty = -1.21$).

A better fit between simulation and experimental data of the first extension of the virgin sample is obtained if the same model as above is used, but an empirical cluster size distribution is chosen instead of the physically motivated distribution function Equ. (37). This is demonstrated in Figs. 46a and 46b, where the adaptation of the same experimental data as above is made with a logarithmic normal form of the cluster size distribution function $\phi(x_1)$ with $x_1 = \xi_1/d$:

$$\phi(x_1) = \frac{\exp\left(-\dfrac{\ln(x_1 / <x_1>)^2}{2b^2} \right)}{\sqrt{\pi/2}\, b\, x_1} \tag{55}$$

Fig 46a demonstrates that a reasonable adaptation of the stress contribution of the clusters can be obtained, if the distribution function Equ. (55) with mean cluster size

$<x_1>$ = 25 and distribution width b = 0.8 is used. Obviously, the form of the distribution function is roughly the same as the one in Fig. 45b.
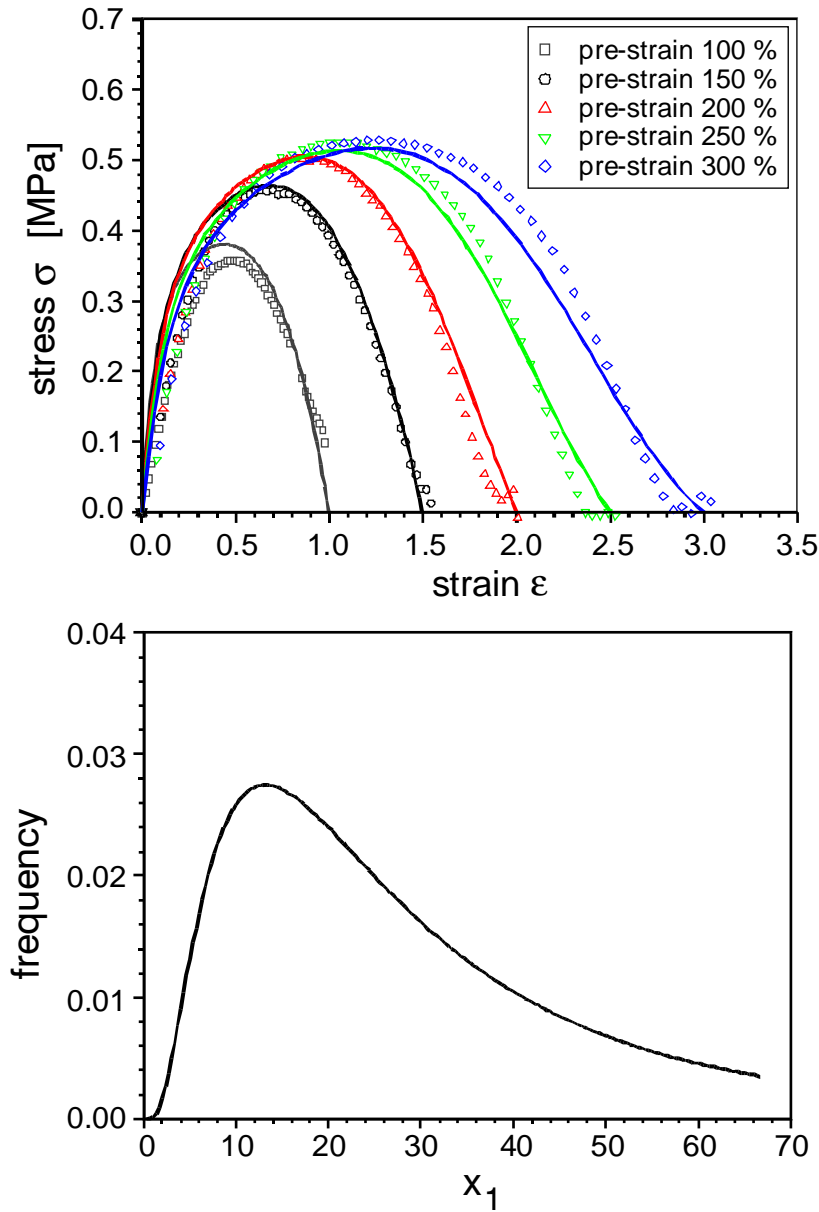

Fig. 46a: Stress contributions of the strained filler clusters for the different pre-strains (upper part), obtained as in Fig. 45b. The solid lines are adapted with the integral term of Equ. (47) and the log-normal cluster size distribution Equ. (55), shown in the lower part. The obtained parameters of the filler clusters are $Q\varepsilon_b/d^3$ = 26 MPa, $<x_1>$ = 25 and b = 0.8.

The simulation curve of the first uniaxial stretching cycle is shown in Fig. 46b. It now fits much better to the experimental data than in Fig. 45c. Furthermore, a fair simulation is also obtained for the equi-biaxial measurement data, implying that the "plausibility criterion", discussed at the end of Section 5.2.2, is also fulfilled for the

extended model of filler reinforced rubbers. Note that for the simulation of the equi-biaxial stress-strain curve, Equ. (42) is used together with Equs. (45) and (38). The strain amplification factor $X(E)$ is evaluated by referring to Equs. (53) and (54) with the boundary condition $\varepsilon_1 = \varepsilon_2 = \varepsilon$ and $\varepsilon_3 = (1+\varepsilon)^{-2} - 1$.
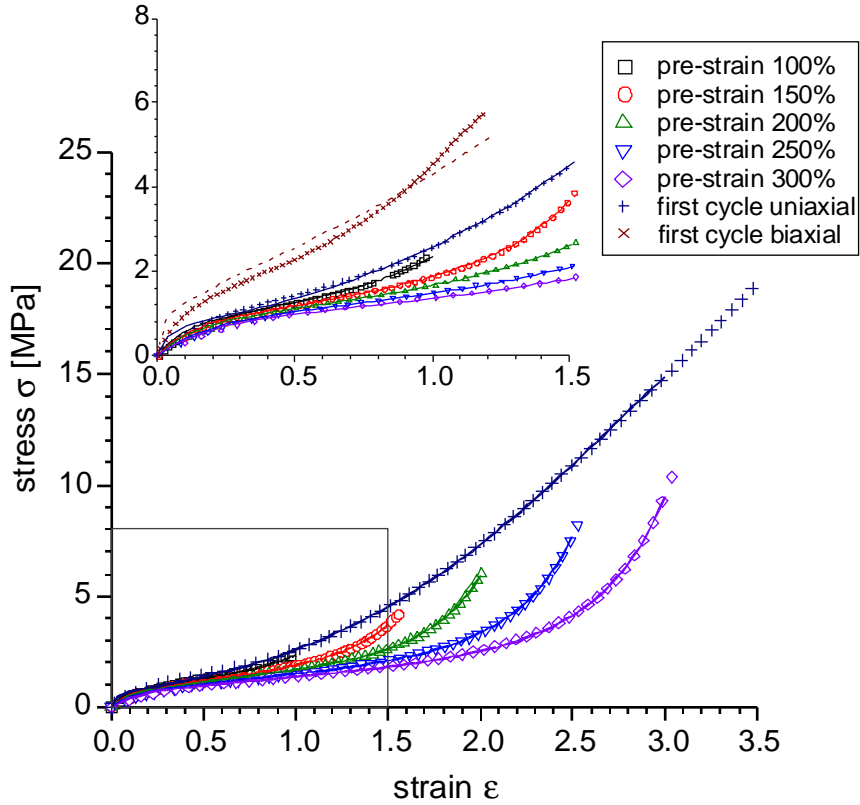

Fig. 46b: Quasi-static, uniaxial stress-strain data (symbols) as in Fig. 45c. The insert shows a magnification of the smaller strains, which also includes equi-biaxial data for the first stretching cycle. The lines are simulation curves with the log-normal cluster size distribution Equ. (55) and material parameters as specified in the insert of Fig. 45a and Tab. 5, sample type C40.

Similar fair agreement between simulation curves and experimental stress-strain data as that shown in Fig. 46b can also be obtained for higher filler concentrations and silica instead of carbon black. In all cases, the log-normal distribution Equ. (55) gives a better prediction for the first stretching cycle of the virgin samples than the distribution function Equ. (37). Nevertheless, adaptations of stress-strain curves of the pre-strained samples are excellent for both cluster size distributions, similar as in Figs. 45c and 46b. The obtained material parameters of four variously filled S-SBR composites used for testing the model are summarized in Tab. 5, whereby both cluster size distributions, Equ. (37) and Equ. (55), have been considered. The obtained fit parameters for the polymer network, filler cluster

morphology and bond fracture mechanics appear physically reasonable. In particular, the value of the cross-link modulus G_c increases with filler concentration due to the attachment of polymer chains at the filler surface, implying an increased effective cross-link density with rising filler loading. The G_c-values of the silica filled systems are found to be somewhat smaller than the carbon black filled systems, indicating that a higher fraction of curatives is deactivated by adsorption at the silica surface as compared to the carbon black surface. The estimated mean cluster size, found between $<\xi_1> \approx 20$ to 30 times the particle diameter d, appears reasonable. Since $d \approx 100$ nm one finds $<\xi_1>$ on the length scale of a few micro meters.

sample type	G_c [MPa]	cluster distribution Equ. (55)			cluster distribution Equ. (37)			X(E) Equ. (53)		
		$<x_1>$	b	$Q\varepsilon_b/d^3$ [MPa]	$<x_1>$	Ω	$Q\varepsilon_b/d^3$ [MPa]	X_∞	X_o	y
C40	0.176	25	0.8	26	26	-0,5	24	-1.209	11.52	0.803
C60	0.190	18	0.8	26	20	-0,5	24	-0.329	17.40	1.180
S40	0.120	19	0.8	24	27	-0,5	28	-0.165	14.12	1.094
S60	0.130	22	0.8	24	31	-0,5	28	-0.148	15.24	1.130

Tab. 5: Material parameters obtained from adaptations of the model to uniaxial stress-strain data of four S-SBR samples (Buna VSL 2525-0) filled with 40 and 60 phr N220 (C40, C60) and silica (S40, S60), respectively. Further polymer parameters are given as $G_e = 0.2$ MPa and $n_e/T_e = 100$, independent of sample type.

The success of the developed model in predicting uniaxial and equi-biaxial stress strain curves correctly emphasizes the role of filler networking in deriving a constitutive material law of reinforced rubbers that covers the deformation behavior up to large strains. Since different deformation modes can be described with a single set of material parameters, the model appears well suited for being implemented into a finite element (FE) code for simulations of three dimensional, complex deformations of elastomer materials in the quasi-static limit.

Beside the consideration of the up-cycles in stretching direction, the model can also describe the down-cycles in backwards direction. This is demonstrated in Fig. 47a for the case of the S-SBR sample filled with 60 phr N 220, which shows an adaptation of the stress-strain curves in stretching direction with the log-normal cluster size distribution Equ. (55). The depicted down-cycles are simulations obtained by Equ. (49) with the fit parameters from the up-cycles. The difference

between up- and down-cycles quantifies the dissipated energy per cycle due to the cyclic breakdown and re-aggregation of filler clusters. The obtained microscopic material parameters for the viscoelastic response of the samples in the quasi-static limit are summarized in Tab. 5.
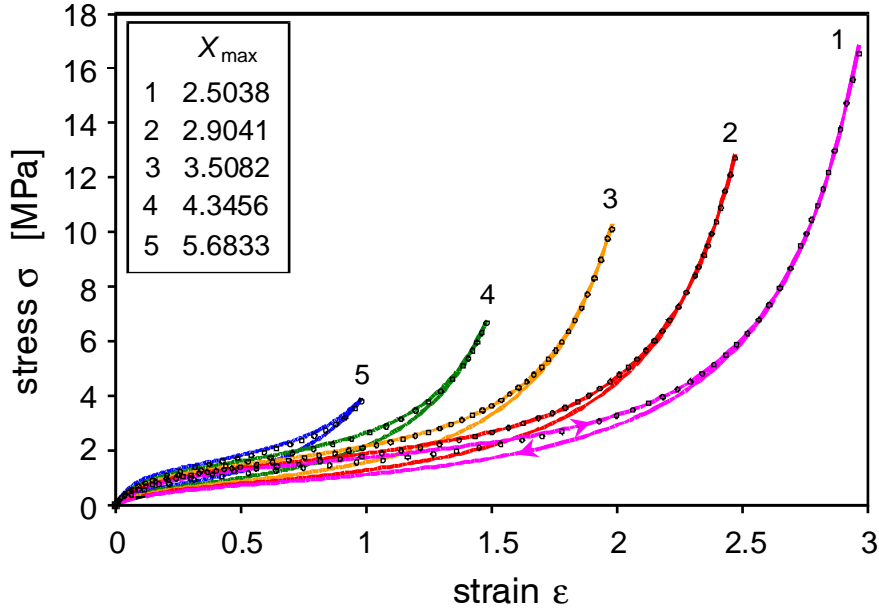

Fig. 47: Quasi-static, uniaxial stress-strain data in stretching direction (symbols) of S-SBR samples (Buna VSL 2525-0) filled with 60 phr N 220 at various pre-strains ε_{max} and simulations (solid lines) of the third up- and down-cycles with the cluster size distribution Equ. (55). Fit parameters are listed in the insert and Tab. 5, sample type C60.

A comparison of the simulation curves in Fig. 47 with experimental stress-strain cycles, depicted e. g. in Fig. 3, shows a slightly different behavior of the down-cycles at large pre-strains. Obviously, the evaluated stress contribution of the strained filler clusters during the down cycle, i. e. the integral term of Equ. (49), is too small to explain the difference between the experimentally observed up- and down-cycles in the high strain regime. The reason for this deviation can probably be found in the pronounced set behavior of reinforced rubbers at large strain that shifts the remaining strain at zero stress to increasing positive values with increasing pre-strain (compare Fig. 3). So far, this set behavior is not considered in the developed model, indicating that it is not part of the "idealized Mullins effect". Probably, the set of the samples results from an inelastic behavior of the polymer network due to very slow relaxation mechanisms. Concerning the measurement results, the set behavior of the samples has been compensated by shifting the experimental stress-strain curves of the pre-strained samples into the origin. This procedure is described more closely in Appendix F.

5.2.4 Stress-strain cycles at medium strain - The Payne effect

In the previous section we demonstrated that the concept of dynamic filler flocculation in strained elastomers is well suited for a quantitative description of stress softening up to large strain, also cited as Mullins effect. On a microscopic level it refers to an irreversible damage of virgin filler-filler bonds and a transition of cluster flexibility with increasing pre-strain, from stiff clusters with virgin bonds to more soft clusters with damaged bonds. Here, we will also consider the filler induced hysteresis more closely, which results from the successive stretching, breakdown and re-aggregation of the fraction of soft clusters during every deformation cycle. Thereby, we focus on the medium strain regime up to about 100%, where the strongly non-linear viscoelastic behavior of filler reinforced elastomers is generally referred to a breakdown of the filler network, also cited as Payne effect. Based on the above developed dynamic flocculation model, we will give here a fundamental explanation of the Payne effect, including influences due to an applied off-set strain. Note however that all our considerations are in the quasi-static limit of slow deformation velocities, corresponding to low frequencies. Nevertheless, we stress that the frequency dependency of the Payne effect is weak in the rubber elastic plateau regime up to some kHz.

In view of a precise description of the stress-strain cycles in the medium strain regime, it appears advantageous to introduce an additional weighting factor into the free energy density Equ. (35), considering the effective volume fraction of the rubber matrix and the filler, respectively. Then, the apparent stress consists of the two contributions:

$$\sigma_{0,\mu}(\varepsilon_\mu) = \left(1 - \Phi/\Phi_p\right)\sigma_{R,\mu}(\varepsilon_\mu) + \left(\Phi/\Phi_p\right)\sigma_{A,\mu}(\varepsilon_\mu) \quad \text{for } \mu = 1, 2, 3 \quad (56)$$

The second contribution from the strained filler clusters has to be evaluated by integrating over the fraction of soft filler clusters that survive the actual stress in the rubber matrix (compare Equs. (47), (49)). These integrals can be solved analytically if the cluster size distribution Equ. (37) is assumed with a fixed width parameter $\Omega = -0.5$. In the case of uniaxial deformations this yields for the up-cycle:

$$\sigma_{A,1}^{up}(\varepsilon) = \hat{\sigma}_{R,1}(\varepsilon)\left\{\left(\frac{2}{<x_1> d^3\,\hat{\sigma}_{R,1}(\varepsilon_{max})}\,Q\varepsilon_b + 1\right)e^{-\frac{2}{<x_1>\,d^3\,\hat{\sigma}_{R,1}(\varepsilon_{max})}Q\varepsilon_b}\right.$$
$$\left. -\left(\frac{2}{<x_1> d^3\,\hat{\sigma}_{R,1}(\varepsilon)}\,Q\varepsilon_b + 1\right)e^{-\frac{2}{<x_1>\,d^3\,\hat{\sigma}_{R,1}(\varepsilon)}Q\varepsilon_b}\right\}$$

(57)

where the only contribution results from the stretching direction $\varepsilon_1 = \varepsilon$ with $\partial\varepsilon_1/\partial t > 0$. For the down-cycle we get two (equal) contributions from the lateral directions ε_2 and ε_3, which now act as stretching directions with $\partial\varepsilon_2/\partial t = \partial\varepsilon_3/\partial t > 0$:

$$\sigma_{A,1}^{down}(\varepsilon) = -2\,\tilde{\sigma}_{R,1}(\varepsilon)\left\{\left(\frac{2}{<x_1>}\,\frac{(1+\varepsilon_{min})^{-3/2}Q\varepsilon_b}{2d^3\,\tilde{\sigma}_{R,1}(\varepsilon_{min})}+1\right)e^{-\frac{1}{<x_1>}\frac{(1+\varepsilon_{min})^{-3/2}Q\varepsilon_b}{d^3\,\tilde{\sigma}_{R,1}(\varepsilon_{min})}}\right.$$
$$\left. -\left(\frac{2}{<x_1>}\,\frac{(1+\varepsilon)^{-3/2}Q\varepsilon_b}{2d^3\,\tilde{\sigma}_{R,1}(\varepsilon)}+1\right)e^{-\frac{1}{<x_1>}\frac{(1+\varepsilon)^{-3/2}Q\varepsilon_b}{d^3\,\tilde{\sigma}_{R,1}(\varepsilon)}}\right\}$$

(58)

Here, the abbreviations Equs. (48) and (50) for the normalized, relative stresses in 1-direction are used and the relation of stresses between 1- and 2-directions is determined by Equ. (51). The stress in the rubber matrix $\sigma_{R,1}$ has to be evaluated with Equ. (44). Note that due to the definition of Equs. (48) and (50), both stress contributions $\sigma_{A,1}{}^{up}$ and $\sigma_{A,1}{}^{down}$ depend on ε_{min} as well as ε_{max}, i. e. the maximum strain- or stress during every cycle.

A similar analytical solution as Equs. (57), (58) can also be obtained for the integral appearing in Equ. (39) for the strain amplification factor X_{max} if $\Omega = -0.5$ is assumed and the exponent is approximated by $d_w - d_f = 1$. This value is not far from the numerical value $d_w - d_f \approx 1.3$ found from computer simulations, which holds for CCA-clusters as well as for percolation clusters in three dimensions. For uniaxial deformations one obtains:

$$X(\varepsilon_{max};\,\varepsilon_{min}) = 1 + c\left(\frac{\Phi}{\Phi_p}\right)^{\frac{2}{3-d_f}}\left\{e^{-\frac{2}{<x_1>}\frac{Q'\varepsilon_b'}{d^3\,\hat{\sigma}_{R,1}(\varepsilon_{max})}}\right. \cdot$$

$$\left.\left[<x_1>-\left(\frac{2}{<x_1>}\left(\frac{Q'\varepsilon_b'}{d^3\,\hat{\sigma}_{R,1}(\varepsilon_{max})}\right)\right)^2 + \frac{2\left(1-<x_1>^{-1}\right)Q'\varepsilon_b'}{d^3\,\hat{\sigma}_{R,1}(\varepsilon_{max})}+<x_1>-1\right]\right\}$$

(59)

$$+2c\left(\frac{\Phi}{\Phi_p}\right)^{\frac{2}{3-d_f}}\left\{e^{-\frac{(1+\varepsilon_{min})^{-3/2}Q'\varepsilon_b'}{<x_1>d^3\,\tilde{\sigma}_{R,1}(\varepsilon_{min})}}\left[<x_1>-\left(\frac{2}{<x_1>}\left(\frac{(1+\varepsilon_{min})^{-3/2}Q'\varepsilon_b'}{2d^3\,\tilde{\sigma}_{R,1}(\varepsilon_{min})}\right)\right)^2\right.\right.$$

$$\left.\left.+\left(\frac{\left(1-<x_1>^{-1}\right)(1+\varepsilon_{min})^{-3/2}Q'\varepsilon_b'}{d^3\,\tilde{\sigma}_{R,1}(\varepsilon_{min})}+<x_1>-1\right)\right]\right\}$$

Obviously, Equ. (59) is an implicit equation for the strain amplification factor X, since the stress in the rubber matrix $\sigma_{R,1}$ depends on the strain amplification factor itself. Nevertheless, Equ. (59) can be solved by iteration.

Figs. 48a and 48b show adaptations of the above model to uniaxial stress-strain cycles of EPDM-samples with 60 phr carbon black (N339) at pre-strains between 5% and 80% (5th up- and down cycles). The measurements have been performed with dumbbells. In Fig. 48a the fifth up- and down cycles are depicted (symbols) together with adaptations according to Equs. (57), (58) (lines) and fitting parameters as shown in the insert. In Fig. 48b, the estimated strain amplification factors from Fig. 48a (crosses) are adapted by Equ. (59), whereby every data point (circle) is obtained by iteration. This procedure has been performed in several steps: First, all parameters, except the tube constraint modulus $G_e = G_N/2$ (see above), are taken as free fitting parameters. Then, the obtained X_{max}-values are adapted according to Equ. (59) also with free fitting parameters c, $<x_1>$ and $Q'\varepsilon_b'/d^3$. In the third step, the stress-strain cycles are fitted again, but now the mean cluster size $<x_1>$, which appears as a common fitting parameter in Equs. (57), (58) and (59), is taken to be fixed as found from the previous fit of X_{max}-values. Finally, the strain amplification factors are again fitted with the newly obtained X_{max}-values. If this leads to a significant deviation of the $<x_1>$-value, step three and four are repeated until $<x_1>$ becomes stable. The final two steps are depicted in Figs. 48a and 48b.

The data depicted in Figs. 48a and 48b show good agreement between experiment and theory. The fitting parameters appear reasonable, though they deviate somewhat from the results shown in Table 5. In particular, the cross-link modulus G_C is larger, $<x_1>$ is somewhat smaller, n_e/T_e is smaller and $Q\varepsilon_b/d^3$ is larger in the present case. The main reason for these deviations is the modified fitting procedure. However, the large difference in G_C can also be attributed to the different rubber matrices, i. e. EPDM and S-SBR, since for EPDM-samples a higher amount of cross-linking agent is used, generally. This is often referred to the fewer number of double bonds, but is also due to the high entanglement density of EPDM, which requires a higher cross-linking density for optimum mechanical properties. The entanglement sensitive plateau modulus of EPDM has been estimated from dynamic-mechanical measurements as $G_N = 1.2$ MPa. This implies for the tube constraint modulus the relatively high value $G_e = 0.6$ MPa, which was used as a fixed parameter in the fitting procedure.

An important point is the stability of the above applied extended fitting procedure, which delivers much saver values for the fitting parameters if $<x_1>$ is evaluated with Equ. (59). A simultaneous fit of $Q\varepsilon_b/d^3$ and $<x_1>$ with Equs. (57) and (58) always leads to a high uncertainty of the two parameters. This can be understood, since e.g. an increase of the hysteresis due to more stable filler clusters can be obtained by a higher tensile strength $Q\varepsilon_b/d^3$ of the repeatedly broken filler-
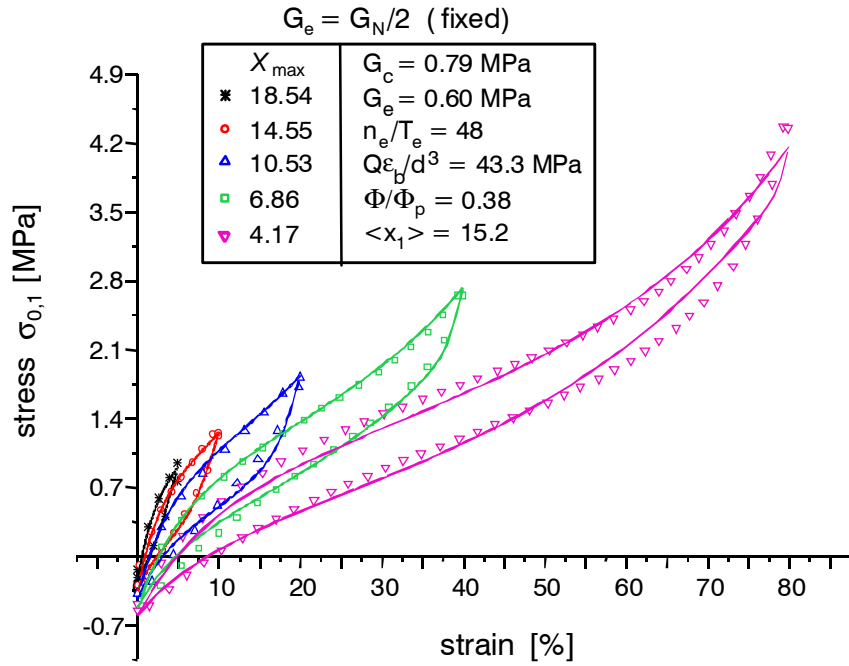
Fig. 48a: Quasi-static stress-strain cycles in uniaxial extension (fifth up- and down-cycles) of EPDM samples with 60 phr carbon black (N339) for pre-strains ε_{max} between 5% and 80% (symbols) and adaptations with Equs. (57), (58) (lines). Fitting parameters are shown in the insert.
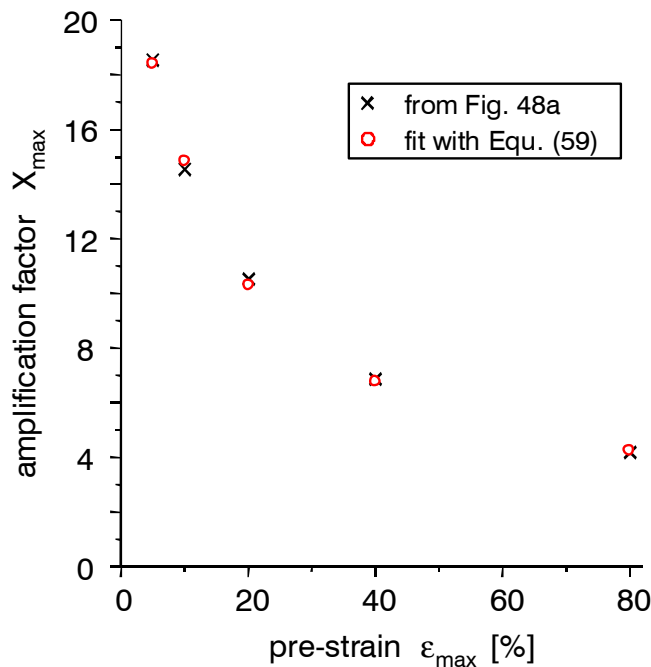

Fig. 48b: Variation of the strain amplification factor X_{max} with pre-strain ε_{max} for the EPDM samples shown in Fig. 48a; (crosses): values obtained from stress-strain simulations; (circles): iterative adaptations with Equ. (59) and parameters c = 2.41, $<x_1>$ = 15.2 and $Q'\varepsilon_b'/d^3$ = 69.6 MPa;

filler bonds or by a larger mean cluster size $<x_1>$, alternatively. The fitting results, shown in the insert of Fig. 48a, demonstrate that a high value of $Q\varepsilon_b/d^3 = 43.3$ MPa, is responsible for the strong hysteresis of the carbon black filled EPDM-samples.

The situation is somewhat different in the case of silica filled S-SBR-samples, where the observed hysteresis is significantly smaller. This is demonstrated in Figs. 49a and 49b, showing uniaxial stress-strain cycles of S-SBR-samples with 65 phr silica (5th up- and down cycles) at pre-strains between 20% and 100% together with adaptations according to the extended fitting procedure, as already applied for the fits in Figs. 48a and 48b. The measurements are again performed with dumbbells. The fitting parameters, shown in the insert of Fig.49a, make clear that the failure stress of the damaged filler-filler bonds $Q\varepsilon_b/d^3 = 21.4$ MPa for the silica filled S-SBR-samples is significantly smaller than for the carbon black filled EPDM-samples. This confirms the strong influence of the failure stress of the repeatedly broken filler-filler bonds on the hysteresis properties of filler reinforced elastomers.

In contrast, the quantity $Q'\varepsilon_b'/d^3$, representing the failure stress of virgin filler-filler bonds, is found to be significantly larger than the failure stress of damaged filler-filler bonds. From the fits in Figs. 48b and 49b we obtain $Q'\varepsilon_b'/d^3 = 69.4$ MPa for the EPDM/N339 system and $Q'\varepsilon_b'/d^3 = 58.8$ MPa for the S-SBR/silica system. Note that the obtained order of magnitude for $Q'\varepsilon_b'/d^3$ is typical for the yield stress of glassy polymers. However, it is about three times larger than the value of the tensile strength obtained for filled rubber samples, which typically lies around 20 to 25 MPa. This can be understood as follows: The tensile strength of the samples can be identified with the limiting relative stress $\hat{\sigma}_{R,1}(\varepsilon_1)$ of the rubber matrix at rupture. If this is inserted into Equ. (34) together with the above value of $Q'\varepsilon_b'/d^3$ for the failure stress of the virgin filler-filler bonds, one obtains for the limiting cluster size at rupture $\xi \approx 3d$. This demonstrates that the proposed mechanism of rubber reinforcement by stress-induced filler cluster breakdown can also considered to be responsible for the strongly enhanced tensile strength of filled rubbers. Obviously, the breakdown of filler clusters leads to a homogenization of the stress field of the rubber matrix, since clusters preferably break close to the stress peaks of the generally not very homogeneously cross-linked rubber matrix. Rupture of the whole sample appears when this mechanism is almost exhausted and only a few small clusters with $\xi < 3d$ remain to break.

We point out that the adapted values for the two parameters c and Φ/Φ_p appear reasonable, as well. In particular, the front factor c of Equ. (39) is found to be almost equal for both sample types ($c = 2.41$ and $c = 2.34$, respectively), confirming that this is a universal scaling factor of order one. The effective filler volume fraction $\Phi/\Phi_p = 0.38$ for the EPDM/N339 sample is obtained significantly larger than the volume fraction $\Phi = 0.23$, corresponding to 60 phr carbon black. This yields for the solid fraction of primary aggregates $\Phi_p \approx 0.6$, which compares to the value obtained
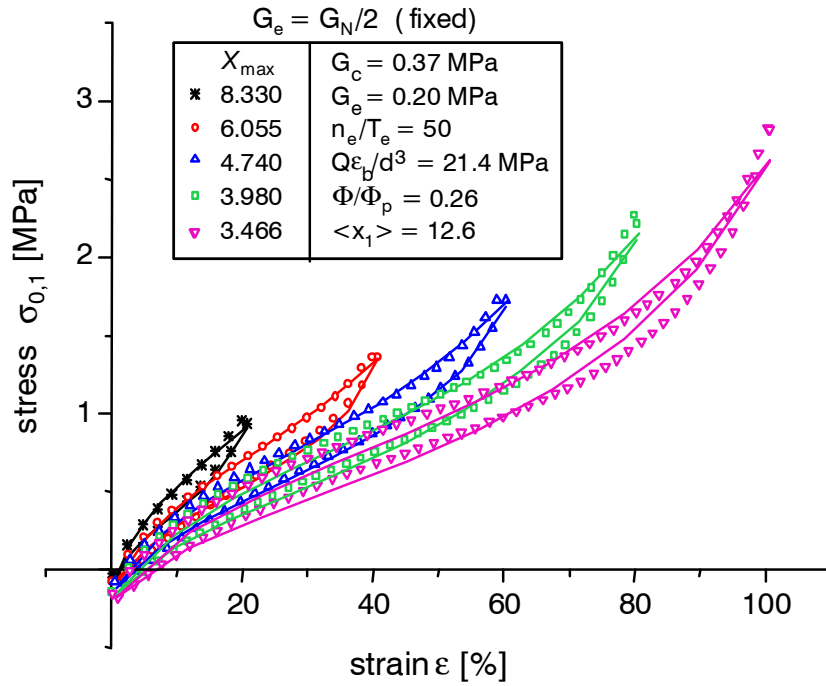
Fig. 49a: Quasi-static stress-strain cycles in uniaxial extension (fifth up- and down-cycles) of S-SBR samples (Buna VSL 2525-0) with 65 phr silica for pre-strains ε_{max} between 20% and 100% (symbols) and adaptations with Equs. (57), (58) (lines). Fitting parameters are shown in the insert.
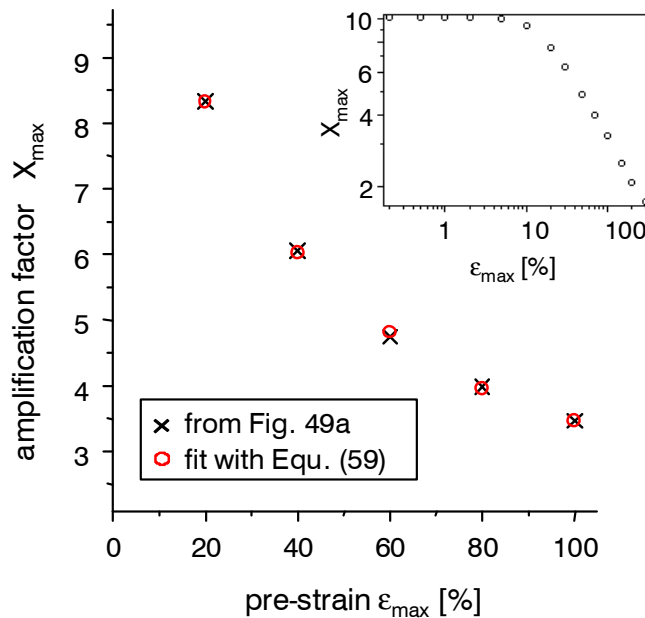

Fig. 49b: Variation of the amplification factor X_{max} with pre-strain ε_{max} for the S-SBR samples shown in Fig. 49a; (crosses): values obtained from stress-strain simulations; (circles): iterative adaptations with Equ. (59) and parameters $c = 2.34$, $<x_1> = 12.6$ and $Q'\varepsilon_b'/d^3 = 58.8$ MPa;

from the TEM investigations shown in Fig. 24 or the estimated values from CDBP-adsorption listed in Tab. 4. Contrary, the adapted value of the effective filler volume fraction $\Phi/\Phi_p = 0.26$ for the S-SBR/silica samples is only slightly larger than Φ, indicating that the solid fraction Φ_p of primary silica aggregates is close to one. This can be related to a low stability of the silica primary aggregates, implying that the breakdown during mixing is almost complete. This correlates with the extremely low values of the CDBP-adsorption measurements, after mechanical treatment of the silica (compare Section 4.2.1). Accordingly, the in-rubber morphology of the silica particles can considered to be close to that of the primary particles, i. e. almost spherical with $\Phi_p \approx 1$.

Note that, contrary to the previous section, the experimental data in Figs. 48a and 49a are not shifted to the origin, but the permanent set is considered by introducing suitable set-stresses, which are subtracted from the apparent stress $\sigma_{0,1}$ in Equ. (56). These set-stresses are found to be relatively small and can easily be extracted from the experimental data. Obviously, they have a negative sign and increase with rising pre-strain from about -0.3 to -0.6 MPa for the EPDM/carbon black samples. The silica filled S-SBR samples show significantly smaller set-stresses in the range of -0.1 to -0.2 MPa.
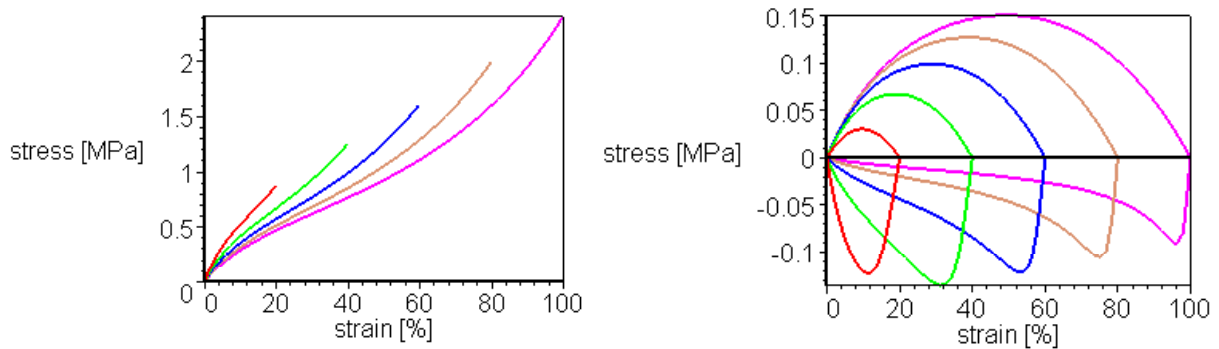

Fig. 50: Simulation of the two stress contributions given by Equ. (56) for the S-SBR samples with 65 phr silica, from the rubber matrix (left) and the strained and broken filler clusters (right). Material parameters are taken from the fits in Figs. 49a and 49b.

In view of an illustration of the applied model, Fig. 50 shows simulations of the two separate stress contributions of $\sigma_{0,1}$ for the S-SBR samples with 65 phr silica. Here, the set stresses are not considered. The left side shows the pure elastic contributions of the rubber matrix (Equs. (38) and (44)) for five different strain amplification factors evaluated according to Equ. (59). The right side shows the hysteresis contributions of the strained and broken filler clusters for the up- and down cycles according to Equs. (57) and (58), respectively. A further simulation is

depicted in the insert of Fig. 49b, where the dependency of the strain amplification factor at small and large pre-strains demonstrated in a double logarithmic plot. It becomes obvious that in the large strain regime, the strain amplification factor follows a power law quite well, in agreement with the empirical Equ. (53) and the approach considered in Refs. [57, 58] or Appendix F. For small pre-strains below 5%, the strain amplification factor levels out at a value close to ten. Accordingly, the slope of the stress-strain cycles, corresponding to the storage modulus G', remains almost constant below 5%. This behavior is typically observed for the small strain plateau regime of the Payne effect of reinforced rubbers (compare e. g. Fig. 2a).
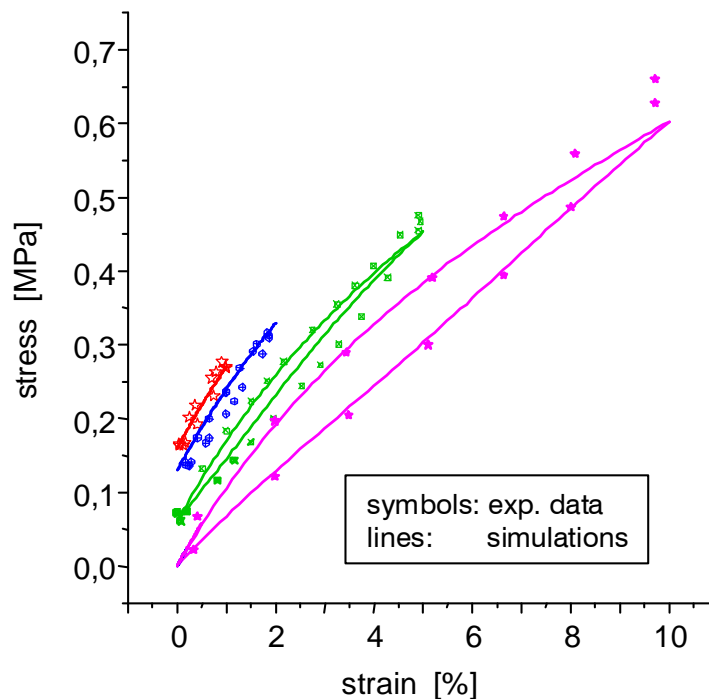

Fig. 51: Comparison of experimental data (symbols) and simulations (lines) of uniaxial hysteresis cycles in the small strain regime between 1% and 10% for the S-SBR samples with 65 phr silica. Material parameters are taken from the fits in Figs. 49a and 49b.

The predicted constant slope of the stress-strain cycles below 5% becomes also apparent in the experimental data (5th up- and down cycles) and simulations depicted in Fig. 51, which show fair agreement. However, a closer examination makes clear that the experimentally detected hysteresis remains on a certain level, while the simulated hysteresis disappears totally below 5%. It means that the developed model can not explain the small strain hysteresis, which must be related to another dissipation mechanism. From the basic principles of the model this is not surprising, since the plateau regime corresponds to very large values of the boundary cluster size beyond the size of the largest clusters in the system. In this

situation, all clusters contribute to the hydrodynamic reinforcement and no cyclic cluster breakdown and re-aggregation can take place.

For a further test of the developed model, we will next compare the predictions for further deformation modes with experimental data. For finding the simulation curves, we will again apply Equ. (56) and evaluate the nominal stress contributions of the filler clusters from the free energy density Equ. (36) with the cluster size distribution Equ. (37) and $\Omega = -0.5$. In the case of equi-biaxial stretching with $\varepsilon_1 = \varepsilon_2 = \varepsilon$, $\varepsilon_3 = (1+\varepsilon)^{-2}-1$ one finds for $\sigma_{A,1} = \partial W_A/\partial \varepsilon_{A,1}$ during the up-cycle almost the same expression as for uniaxial stretching:

$$\sigma_{A,1}^{up}(\varepsilon) = \hat{\sigma}_{R,1}(\varepsilon) \left\{ \left(\frac{2}{<x_1> d^3 \hat{\sigma}_{R,1}(\varepsilon_{max})} Q\varepsilon_b + 1 \right) e^{-\frac{2}{<x_1>} \frac{Q\varepsilon_b}{d^3 \hat{\sigma}_{R,1}(\varepsilon_{max})}} \right.$$
$$\left. - \left(\frac{2}{<x_1> d^3 \hat{\sigma}_{R,1}(\varepsilon)} Q\varepsilon_b + 1 \right) e^{-\frac{2}{<x_1>} \frac{Q\varepsilon_b}{d^3 \hat{\sigma}_{R,1}(\varepsilon)}} \right\} \tag{60}$$

Here, two contributions, resulting from the stretching directions $\varepsilon_1 = \varepsilon_2 = \varepsilon$ with $\partial \varepsilon/\partial t > 0$ are taken into account and the abbreviation Equ. (48) is used. The stress of the rubber matrix $\sigma_{R,1}$ must here be evaluated according to the equi-biaxial case with Equ. (45). For the down-cycle we have to consider one contribution from the lateral direction ε_3, which now acts as stretching directions with $\partial \varepsilon_3/\partial t > 0$:

$$\sigma_{A,1}^{down}(\varepsilon) = -2\widetilde{\sigma}_{R,1}(\varepsilon) \left\{ \left(\frac{2}{<x_1>} \frac{2(1+\varepsilon_{min})^{-3} Q\varepsilon_b}{d^3 \widetilde{\sigma}_{R,1}(\varepsilon_{min})} + 1 \right) e^{-\frac{2}{<x_1>} \frac{2(1+\varepsilon_{min})^{-3} Q\varepsilon_b}{d^3 \widetilde{\sigma}_{R,1}(\varepsilon_{min})}} \right.$$
$$\left. - \left(\frac{2}{<x_1>} \frac{2(1+\varepsilon)^{-3} Q\varepsilon_b}{d^3 \widetilde{\sigma}_{R,1}(\varepsilon)} + 1 \right) e^{-\frac{2}{<x_1>} \frac{2(1+\varepsilon)^{-3} Q\varepsilon_b}{d^3 \widetilde{\sigma}_{R,1}(\varepsilon)}} \right\} \tag{61}$$

with the abbreviation:

$$\widetilde{\sigma}_{R,1}(\varepsilon) = \left| \sigma_{R,1}(\varepsilon) - \left(\frac{1+\varepsilon_{max}}{1+\varepsilon} \right)^3 \sigma_{R,1}(\varepsilon_{max}) \right| \tag{62}$$

The strain amplification factor for equi-biaxial stretching is obtains with the approximations $\Omega = -0.5$ and $d_w - d_f = 1$ from Equs. (36), (37) as an expression similar to Equ. (59), where the stress of the rubber matrix $\sigma_{R,1}$ must again be evaluated with Equ. (45):

$$X(\varepsilon_{max}; \varepsilon_{min}) = 1 + 2c \left(\frac{\Phi}{\Phi_p}\right)^{\frac{2}{3-d_f}} \left\{ e^{-\frac{2}{<x_1>}\frac{Q'\varepsilon_b'}{d^3\,\hat{\sigma}_{R,1}(\varepsilon_{max})}} \right. .$$

$$\left[<x_1> - \left(\frac{2}{<x_1>}\left(\frac{Q'\varepsilon_b'}{d^3\,\hat{\sigma}_{R,1}(\varepsilon_{max})}\right)\right)^2 + \frac{2\left(1-<x_1>^{-1}\right)Q'\varepsilon_b'}{d^3\,\hat{\sigma}_{R,1}(\varepsilon_{max})} + <x_1> -1 \right] \right\}$$

(63)

$$+ c\left(\frac{\Phi}{\Phi_p}\right)^{\frac{2}{3-d_f}} \left\{ e^{-\frac{4(1+\varepsilon_{min})^{-3}Q'\varepsilon_b'}{<x_1>d^3\,\widetilde{\sigma}_{R,1}(\varepsilon_{min})}} \left[<x_1> - \left(\frac{2}{<x_1>}\left(\frac{2(1+\varepsilon_{min})^{-3}Q'\varepsilon_b'}{d^3\,\widetilde{\sigma}_{R,1}(\varepsilon_{min})}\right)\right)^2 \right. \right.$$

$$\left. \left. + \left(\frac{4\left(1-<x_1>^{-1}\right)(1+\varepsilon_{min})^{-3}\,Q'\varepsilon_b'}{d^3\,\widetilde{\sigma}_{R,1}(\varepsilon_{min})} + <x_1> -1 \right) \right] \right\}$$

Fig. 52 compares simulations and experimental data of equi-biaxial stretching cycles of rubber reinforcement between 20% and 80% pre-strain for the S-SBR samples with 65 phr silica. For the smallest pre-strains, agreement between experiment and simulation is fairly well, but with increasing pre-strain one finds signi-
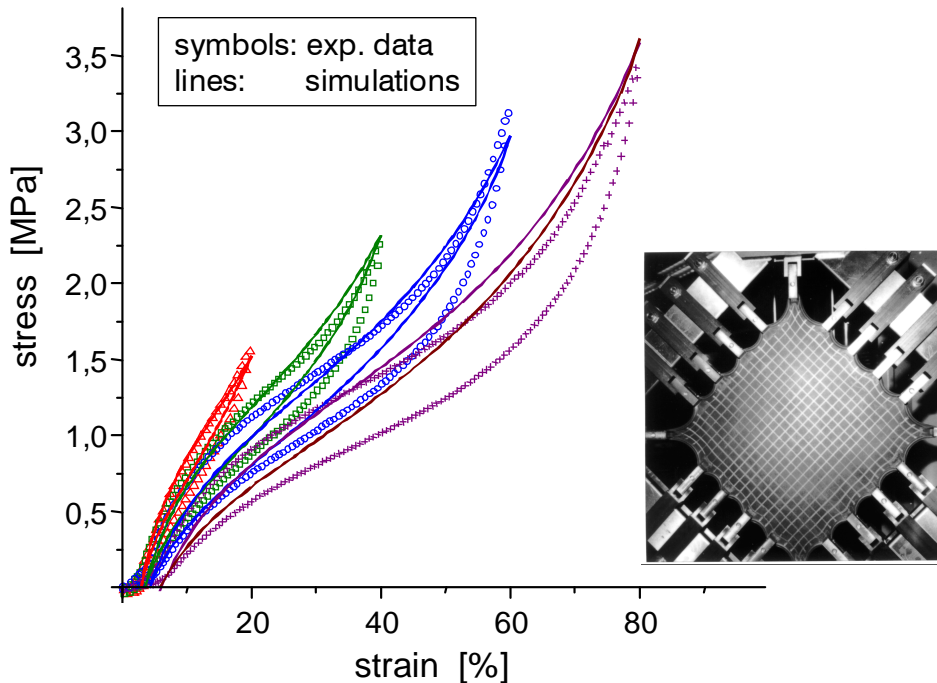

Fig. 52: Comparison of experimental data (symbols) and simulations (lines) of equi-biaxial hysteresis cycles between 20% and 80% pre-strain for the S-SBR / silica samples with material parameters from the fits in Figs. 49a and 49b. The insert shows the stretching frame applied for equi-biaxial testing.

ficantly more hysteresis of the experimental stress-strain curves as compared to the simulations. Nevertheless, the strain amplification factors, evaluated with Equ. (63), appear reasonable, since the simulated stress maxima fit quite well to the experimental data. For a discussion of the observed large deviations of hysteresis it is necessary to consider the experimental equipment for the equi-biaxial investigations more closely. The data were obtained with a stretching frame with 20 clamps holding the rubber sheet and rolls running on a steel frame, as depicted in the insert of Fig. 52. Due to this construction it is clear that the friction of the rolls, which increases with loading, contributes to the overall hysteresis measured between the up- and down cycles. Accordingly, the successive deviations in hysteresis with increasing loading can possibly be explained by the insufficient experimental equipment. A final answer to this question can not be given at this stage, but further investigations have to be performed in the future.

So far we considered uniaxial and equi-biaxial stretching of carbon black and silica filled elastomers with $\varepsilon_1 > 0$. We next look at the predictions of the model in the stretching-compression mode when ε_1 also becomes negative. In this case we have to take into account that in general the strain amplification factor does not remain constant, but depends on $\varepsilon_{\mu,max}$ as well as on the actual strain ε_μ ($X_\mu = X_\mu(\varepsilon_\mu, \varepsilon_{\mu,max})$). This follows directly from the two conditions of constant sample volume used above for the estimation of the lateral strain values, i. e. the (internal) condition of constant volume of the rubber matrix $\lambda_1 \lambda_2 \lambda_3 = (1+X_1\varepsilon_1)(1+X_2\varepsilon_2)(1+X_3\varepsilon_3) = 1$ and the (external) condition of constant volume of the sample $(1+\varepsilon_1)(1+\varepsilon_2)(1+\varepsilon_3) = 1$. Since for uniaxial stretching the strain amplification factor $X_1 = X(\varepsilon_{1,max}) \equiv X_{max}$ is assumed to be independent of ε_1, provided ε_1 is in stretching direction ($\partial\varepsilon_1/\partial t > 0$), both conditions imply for the two compression directions:

$$X_2 = X_3 = \frac{\left(1 + X_{max}\,\varepsilon_1\right)^{-1/2} - 1}{\left(1 + \varepsilon_1\right)^{-1/2} - 1} \tag{64}$$

This dependency on ε_1 holds for the two lateral directions in the case of uniaxial stretching. For uniaxial compression these two lateral strains $\varepsilon_2 = \varepsilon_3$ are in stretching direction ($\partial\varepsilon_2/\partial t = \partial\varepsilon_3/\partial t > 0$) and hence the corresponding strain amplification factors $X_2 = X_3 = X_{max}$ are independent of ε_2 and ε_3. Then, the above two conditions of constant volume imply for the amplification factor X_1 in compression direction ($\partial\varepsilon_1/\partial t < 0$):

$$X_1(\varepsilon_1,\, \varepsilon_{1,max}) = \frac{\left(1 + X(\varepsilon_{1,max})\left(\left(1 + \varepsilon_1\right)^{-1/2} - 1\right)\right)^{-2} - 1}{\varepsilon_1} \tag{65}$$

In the framework of a constitutive formulation we find the following general dependency $X_\mu(\varepsilon_\mu)$ for the compression directions with $\partial\varepsilon_\mu/\partial t < 0$:

$$X_\mu(\varepsilon_\mu,\varepsilon_{\mu,max}) = \frac{\left(1 + X(\varepsilon_{\mu,max})\left(\left(1+\varepsilon_\mu\right)^{-\theta} - 1\right)\right)^{-1/\theta} - 1}{\varepsilon_\mu} \qquad (66)$$

and $X_\mu = X(\varepsilon_{\mu,max}) \equiv X_{max}$ for the stretching directions with $\partial\varepsilon_\mu/\partial t > 0$. Here, θ is the ratio between the number of stretching and compression directions. In three dimensional space this number can take the three values 1/2, 1 or 2. It is important to note that the function $\lambda_\mu(\varepsilon_\mu) = (1+X_\mu\varepsilon_\mu)$ is smooth at $\varepsilon_\mu = 0$ with the same slope $\partial\lambda_\mu/\partial\varepsilon_\mu = X_{max}$ for $\varepsilon_\mu \to \pm 0$. Accordingly, the differential $\partial\lambda_\mu$ is well defined for all values $\varepsilon_\mu \geq -1$.

In particular, Fig. 53 demonstrates the dependency of the internal strain ratio $\lambda_1 = (1+X_1\varepsilon_1)$ on external strain ε_1 in the cases of uniaxial deformations for five arbitrary chosen values of X_{max}, where Equ. (65) is used in the compression regime and $X_1 = X_{max}$ in the stretching regime Obviously, similar as in the case of unfilled samples, λ_1 becomes zero for the limiting value $\varepsilon_1 \to -1$, independent of X_{max}. The smoothness of λ_1 at $\varepsilon_1 = 0$ becomes apparent.
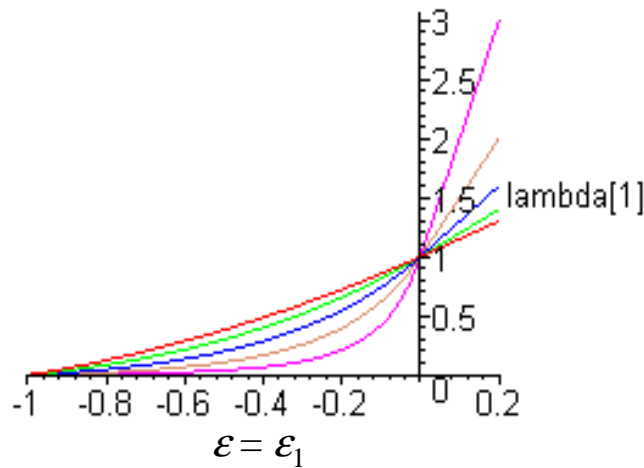
Fig. 53: Variation of the strain ratio $\lambda_1 = (1+X_1\varepsilon_1)$ with external strain ε_1 for uniaxial deformations in the compression ($\varepsilon_1 < 0$) and stretching regime ($\varepsilon_1 > 0$) with $X_1(\varepsilon_1)$ given by Equ. (65).

We point out that the simulations of uniaxial and equi-biaxial stretching shown in Figs. 48 to 52 could be performed without taking into account the explicit strain dependency of X_2 or X_3 given by Equ. (64), since all parameterizations were made with respect to the stretching direction with strain amplification factor $X(\varepsilon_{1,max})$ independent of ε_1. For the uniaxial compression mode this situation changes and

Equ. (65) has to be applied, explicitly, if the same parameterization is used. Fig. 54 compares experimental data (5th up- and down cycles) and simulation curves for the stretching-compression mode of the EPDM samples with 60 phr carbon black (N339). Material parameters for the simulations are taken from the fits in Figs. 48a and 48b. Obviously, the simulations yield too high stress values in the compression regime, while the stress-strain curves in the stretching regime lie somewhat too low. The predicted hysteresis agrees fairly well with the experimental data. The deviations in the stretching regime indicate that the evaluated strain amplification factors are somewhat too small. The deviations in the compression regime are probably related to volume changes of the samples that are not considered in the model. Recent investigations showed that the volume of carbon black filler natural rubber increases under uniaxial stretching by more than 10%, while it decreases under uniaxial compression [176]. Such strong deviations from the assumed ideal incompressible behavior can not be ignored. They will be investigated and implemented into the model in the near future.
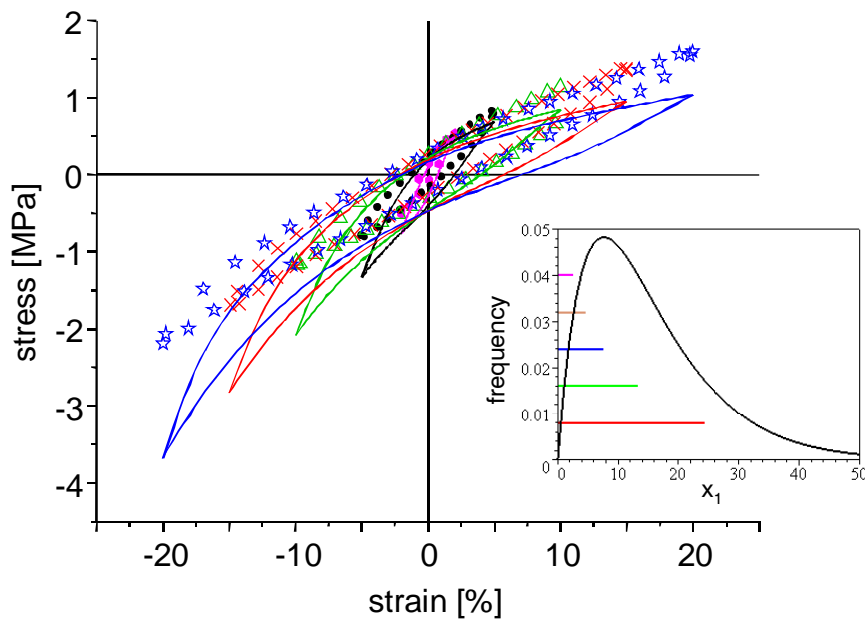
Fig. 54: Comparison of simulated stress-strain curves (lines) with quasi-static data (symbols) in uniaxial stretching-compression mode of the EPDM/N339 samples for pre-strains ε_{max} and ε_{min} between $\pm$ 2% and $\pm$ 20%. Material parameters are taken from the fits in Figs. 48a and 48b. The insert shows the cluster size distribution, with bars indicating the size regimes of the rigid clusters for the stress-strain cycles of $\pm$ 20% (top) up to $\pm$ 2% (bottom).

The insert of Fig. 54 shows the cluster size distribution. The solid bars indicating the size regimes of the rigid clusters for the different stress-strain cycles, i. e. the integration regimes for evaluating the strain amplification factor in 1-direction.

We point out that the integration regimes in 2- and 3-direction are larger than the regime in 1-direction due to smaller values of the normalized relative stress in 2- and 3-direction. This leads to an increasingly anisotropic, oblate shape of the rigid clusters with increasing pre-strain. Contrary, for the pure uniaxial stretching mode, the shape of the rigid clusters becomes more and more elliptical. According to Equ. (39), the evaluated strain amplification factor averages over this anisotropy, i. e. we apply the geometrical mean value of the X_{max}-value in the different space directions. This choice is not compelling but more intuitive and therefore a possible source of inaccuracy of the model.

Nevertheless, the basic micro-mechanical assumptions of the dynamic flocculation model, introduced above, seem to be well suited for a quantitative explanation of stress softening and hysteresis phenomena of filler reinforced rubber. This is confirmed by the systematic variation of material parameters with polymer- and filler type as summarized in Tab. 6. They were obtained by the same adaptation method as applied in Figs. 48 and 49. Some specific differences between the parameters of the silica and carbon black composites, shown in the first two rows of Tab. 6, were already discussed above. A comparison of the material parameters of the EPDM- and S-SBR composites with the same carbon black N339 shows no pronounced differences, apart from the finite extensibility parameter n_e/T_e. For both systems, we find the highest values of the cross-link modulus G_c, mean cluster size $<x_1>$, effective filler volume fraction Φ/Φ_P and tensile strength of damaged bonds $Q\varepsilon_b/d^3$, which is responsible for the large hysteresis of these systems. All these microscopic properties can be related to the high activity (structure and specific surface) of the fine black N339, which is often used in highly hysteretic tire treads. In comparison, the NR-composite with the low activity coarse black N772, which is typi-

Sample Type	G_c [MPa]	G_e [MPa]	n_e/T_e	$Q\varepsilon_b/d^3$ [MPa]	$Q'\varepsilon_b'/d^3$ [MPa]	$<x_1>$	Φ/Φ_P	c
S-SBR[1] / Silica	0.37	0.2	50	21.4	58.8	12.6	0.26	2.34
EPDM / N339	0.79	0.6	48	43.3	69.6	15.2	0.38	2.41
S-SBR[2] / N339	0.73	0.2	86	41.0	81.3	14.7	0.39	2.18
NR / N772	0.48	0.3	67	11.8	81.6	3.8	0.22	5.63
S-SBR[1] / Microgel[3]	0.68	0.2	50	8.0	16.4	7.0	0.27	1.29

[1] VSL 2525-0

[2] VSL 5025-0

[3] Micromorph-1P

Tab. 6: Material parameters obtained from adaptations of the model to uniaxial stress strain cycles in stretching mode between 5% and 100 % strain. The filler volume fraction is kept constant $\Phi \approx 0.23$ for all samples.

cally applied in weakly hysteretic engine bearings, shows lower values for all of these four parameters. This can be well understood as follows: first, the effective filler

volume fraction is smaller, since N772 is a low structure black and the mean cluster size is smaller due to the lower mobility of the coarse filler particles in the rubber matrix. Second, the strongly reduced tensile strength of the damaged filler-filler bonds $Q\varepsilon_b/d^3$ can be identified as the micro-mechanical origin of the low hysteresis of the black N772. However, the value of the tensile strength of the virgin bonds $Q'\varepsilon_b'/d^3$ is found to be relatively large for the NR/N772 composite and compares to that of the S-SBR/N339 system. Nevertheless, the stiffness (mean slope of the of the stress-strain cycles) of the second system is significantly larger because the mean cluster size is larger, resulting in higher strain amplification factors.

The different G_c-values of the composites listed in Tab. 6 can partly be related to the differences in cross-linking efficiency of the rubbers and the deactivation of the accelerators at the various filler surfaces. However, it also reflects the characteristic difference in coupling density between the polymer chains and the filler surface, since G_c represents all kind of network junctions in the system. The higher G_c-values indicate that the coupling density of the fine black N339 is larger than that of the coarse black N772 and the coupling density of the S-SBR/microgel system is larger than that of the S-SBR/silica composite. Recent investigations of filled S-SBR composites by NMR- and mechanical analysis have demonstrated that the coupling density of the polymer chains to the filler surface is smaller for silica (Ultrasil GR 7000) as for carbon black (N220). The mean distance of polymer-filler couplings was obtained as 1.2 nm for silica and 1.7 nm for carbon black [177].

It is important to note that stress softening is also present during dynamic stress-strain cycles of filled rubbers at small and medium strain. This was demonstrated in recent studies of the impact of pre-strain on dynamic mechanical properties of filler reinforced rubbers [178]. In particular, stress softening is observed for the dynamic mechanical data depicted in Fig. 55. They were obtained with dumbbells for various pre-strains in stretching and compression direction of S-SBR composites with 60 phr N220. In the framework of the above model, the observed shift of the center points of the cycles to smaller stress values with increasing strain amplitude or maximum strain and the accompanied drop of the slope of the hysteresis cycles is related to a decreasing strain amplification factor X_{max}. From the micro-mechanical concept of filler cluster breakdown and re-aggregation it is clear that a pronounced Payne effect must appear also for pre-strained samples that compares to the one observed for dynamic excitations around the stress-strain origin. This has led to some conceptual problems in relating the Payne effect to filler network breakdown [179,180], which is briefly reviewed in the introduction of Appendix B. The problems arise primary from the fact that the shifting of the center

points of the hysteresis cycles due to stress softening is ignored if the concept of linear viscoelasticity is applied and the dynamic storage and loss moduli are considered, only.
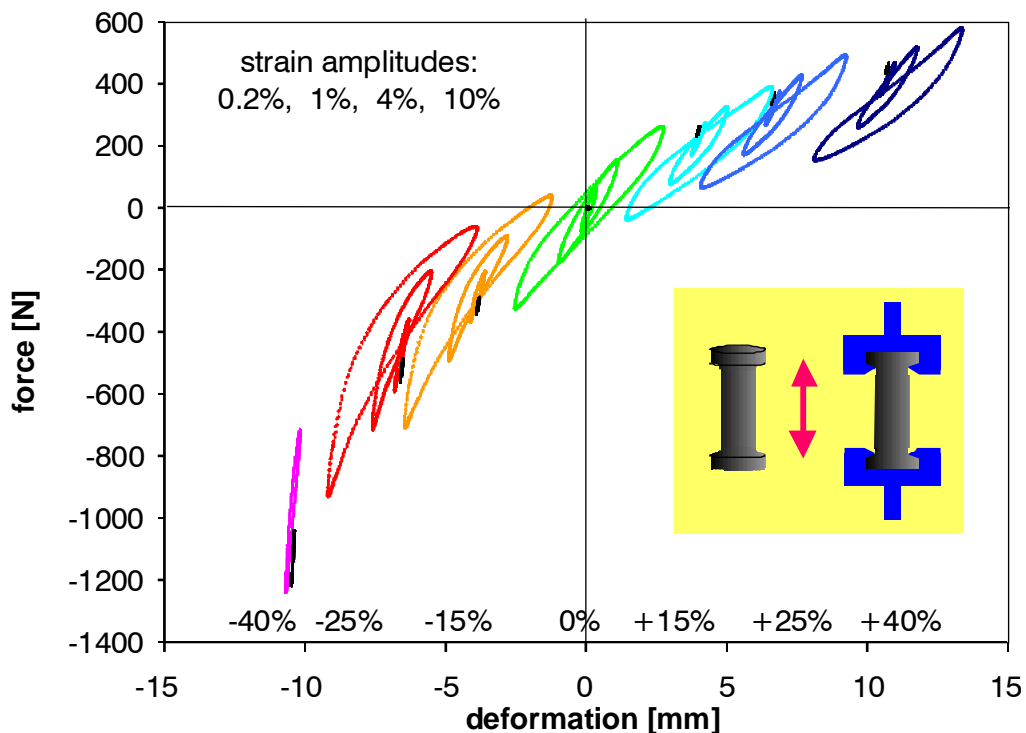

Fig. 55: Dynamic deformation cycles for uniaxial harmonic excitations in tension and compression at 1 Hz of S-SBR samples (VSL 2525-0) filled with 60 phr N 220 at various pre-strains and strain amplitudes, as indicated. The insert shows the applied samples (dumbbells) together with the fixing tools.

The experimental stress-strain cycles shown in Fig. 55 are quite similar to the simulation curves evaluated in this section. However, at present an adaptation of the developed model to the dynamic data is not possible, mainly because of two reasons. On the one side, an explicit time dependency of the stress-strain cycles is not considered so far. On the other side, only full cycles from maximum to minimum strain can be described, where all fragile clusters break down and re-combine. A more general model must also consider the re-aggregation mechanism in dependence of strain, in order to describe all kind of stress-strain cycles. This will be a task of future work. Despite of these limitations there is strong evidence that the Payne effect can be described on the basis of the derived model of stress softening and filler-induced hysteresis, which allows for a proper simulation of quasi-static stress-strain curves, referred to as Mullins effect. This demonstrates that both effects can be traced back to the same micro-mechanical mechanism.

6.   Summary and conclusions

In the first part of the paper (Section 3, Appendix A and C), the morphology and surface activity of carbon black, the most important filler in rubber industry, are analyzed. It is shown that due to the disordered nature of carbon black formation during processing in a furnace reactor, the morphology of furnace blacks is well described by referring to a fractal analysis. Investigations of the surface roughness of carbon blacks by static gas adsorption point out that all furnace blacks exhibit a pronounced surface roughness with an almost unique value of the surface fractal dimension $d_s \approx 2.5 - 2.6$ on atomic length scales below 6 nm. This universality is related to a particular random deposition mechanism of carbon nuclei on condensed carbon particles that governs the surface growth of carbon blacks during processing. Graphitization of carbon blacks diminishes the roughness of the surface on length scales below $z < 1$ nm, while on larger length scales the surface fractal dimension remains unchanged. The surface fractal dimension of all examined graphitized blacks is found as $d_s \approx 2.3$ below 1 nm, independent of the applied evaluation procedure. The investigations make clear that the pronounced surface roughness contributes to the highly reinforcing potential of furnace blacks, since it supports a strong polymer-filler coupling.

A second quantity, which impacts the polymer-filler coupling, is the surface energy distribution of reinforcing fillers. The analysis by static gas adsorption in the low pressure regime demonstrates that four different energetic sites can be distinguished, which are shown to be related to the characteristic surface morphology of furnace blacks. The fraction of highly energetic sites decreases significantly with grade number and disappears almost completely during graphitization. It indicates that the reinforcing potential of carbon black is closely related to the amount of highly energetic sites that can be well quantified by the applied gas adsorption technique at low pressure. According to the universal surface roughness of furnace blacks independent of grade number, one expects that the reinforcing potential owing to the surface roughness of carbon blacks is not much different. Nevertheless, the detected high energetic and morphological disorder of the carbon black surface can considered to be responsible for a strong polymer-filler coupling and phase bonding. Beside the specific surface, this is an important factor for obtaining adequate ultimate properties of carbon black reinforced rubbers.

The morphology of the more or less ramified primary carbon black aggregates, as analyzed by TEM techniques, is readily described by a fractal approach. This refers to the specific cluster-cluster aggregation mechanism of primary particles under ballistic conditions, which is realized during carbon black processing. It implies a mass fractal dimension $d_f \approx 1.9 - 1.95$, which is indeed found

for the fine blacks. For the more coarse furnace blacks larger values of d_f are obtained that increase with the grade number. This results from electrostatic repulsive interactions between the aggregates due to the application of processing agents. During compounding of carbon blacks with highly viscous rubbers, rupture of primary aggregates takes place depending on the mixing severity and grade number. It implies that the aggregate size decreases with increasing mixing time or filler loading, preferably for the high structured coarse blacks. The resulting influence on the mechanical properties of the composites can be described on a quantitative level by considering the rising solid fraction of primary aggregates with increasing mixing severity, which impacts the mechanically effective filler concentration.

In the second part of the paper (Section 4, Appendix C, D and E), carbon black networking in elastomer composites is analyzed by applying TEM-, electrical percolation-, dielectric- as well as flocculation investigations. This provides information on the fractal nature of filler networks as well as the morphology of filler-filler bonds. It becomes obvious that TEM analysis gives a limited microscopic picture of the filler network morphology, only, due to spatial inter-penetration of flocculated neighboring filler clusters. Investigations of the dc-conductivity demonstrate that no universal percolation structure for the filler network is realized on mesoscopic length scales, if a critical filler concentration is exceeded. Instead, the structure appears to be modified by a superimposed kinetic aggregation process, which explains the detected non-universal value of the percolation exponent and the impact of specific surface and polymer micro-structure on the percolation threshold. Flocculation studies, considering the small strain mechanical response of the uncross-linked composites during heat treatment (annealing), demonstrate that a relative movement of the particles takes place that depends on particle size, molar mass of the polymer as well as polymer-filler and filler-filler interaction. This provides strong experimental evidence for a kinetic cluster-cluster aggregation mechanism of filler particles in the rubber matrix to form a filler network. The ac-conductivity exponent in the high frequency regime is shown to be related to an anomalous diffusion mechanism of charge carriers on fractal carbon black clusters. This confirms the fractal nature of filler networks in elastomers below a certain length scale, though it gives no definite information on the particular network structure.

From the dielectric investigations it becomes obvious that charge transport above the percolation threshold is limited by a hopping or tunneling mechanism of charge carriers over small gaps of order 1 nm between adjacent carbon black particles. From this finding and the observed dependency of the flocculation dynamics on the amount of bound rubber, a model of filler-filler bonds is developed. It relates the mechanical stiffness of filler-filler bonds to the remaining gap size

between the filler particles that develops during annealing (and cross-linking) of filled rubbers. In this model, stress between adjacent filler particles in a filler cluster is assumed to be transmitted by nanoscopic, flexible bridges of glassy polymer, implying that a high flexibility and strength of filler clusters in elastomers is reached. This picture of filler-filler bonds allows for a qualitative explanation of the observed flocculation effects by referring to the amount of bound rubber and it is impact on the stiffness and strength of filler-filler bonds.

In the last part of the paper (Section 5, Appendix B, C, D, E and F), a micro-mechanical model of rubber reinforcement by flexible filler clusters is developed that allows for a quantitative analysis of stress softening and hysteresis of filler reinforced rubbers up to large quasi-static deformations. It is shown that the kinetic cluster-cluster aggregation (CCA) model of filler networking in elastomers represents a reasonable theoretical basis for understanding the linear viscoelastic properties of reinforced rubbers. According to this model, filler networks consists of a space-filling configuration of CCA-clusters with characteristic mass fractal dimension $d_f \approx 1.8$. The consideration of flexible chains of filler particles, approximating the elastically effective backbone of the filler clusters, allows for a micro-mechanical description of the elastic properties of tender CCA-clusters in elastomers. The main contribution of the elastically stored energy in the strained filler clusters results from the bending-twisting deformation of filler-filler bonds. The predicted power-law behavior of the small strain modulus of filler reinforced rubbers is confirmed by a variety of experimental data, including carbon black and silica filled rubbers as well as composites with model fillers (microgels).

Beside the elastic behavior, the failure properties of filler-filler bonds and filler clusters are considered in dependence of cluster size. This completes the micro-mechanical description of tender but fragile filler clusters in the stress field of a strained rubber matrix. By assuming a specific cluster size distribution in reinforced rubbers, which is motivated by an asymptotic solution of Smoluchowski's equation for the kinetics of irreversible cluster-cluster aggregation, a constitutive material model of filler reinforced rubbers is derived. It is based on a non-affine tube model of rubber elasticity, including hydrodynamic amplification of the rubber matrix by a fraction of rigid filler clusters with filler-filler bonds in the unbroken, virgin state. The filler-induced hysteresis is described by an anisotropic free energy density, considering the cyclic breakdown and re-aggregation of the residual fraction of more fragile filler clusters with already broken filler-filler bonds. The model assumes that the breakdown of filler clusters during the first deformation of the virgin samples is totally reversible, though the initial virgin state of filler-filler bonds is not recovered. This implies that, on the one side, the fraction of rigid filler clusters decreases with increasing pre-strain, leading to the pronounced stress softening after the first

deformation cycle. On the other side, the fraction of fragile filler clusters increases with increasing pre-strain, which impacts the filler-induced hysteresis.

It is demonstrated that the quasi-static stress-strain cycles of carbon black as well as silica filled rubbers can be well described in the scope of the theoretic model of stress softening and filler-induced hysteresis up to large strain. The obtained microscopic material parameter appear reasonable, providing information on the mean size and distribution width of filler clusters, the tensile strength of filler-filler bonds and the polymer network chain density. In particular it is shown that the model fulfils a "plausibility criterion" important for FE applications. Accordingly, any deformation mode can be predicted based solely on uniaxial stress-strain measurements, which can be carried out relatively easily.

From the simulations of stress-strain cycles at small and medium strain it can be concluded that the model of anisotropic cluster breakdown and re-aggregation for pre-strained samples represents a fundamental micro-mechanical basis for the description of non-linear viscoelasticity of filler reinforced rubbers. Thereby, the mechanisms of energy storage and dissipation are traced back to the elastic response of the polymer network as well as the elasticity and fracture properties of flexible filler clusters. For a time dependent, complete characterization of non-linear viscoelastic stress-strain cycles of filler reinforced rubbers, the dynamic-mechanical response of the polymer matrix has to be considered, as well. Furthermore, the re-aggregation rate must be specified in dependence of strain, in order to describe any kind of stress-strain cycles. This will be a task of future work.

At present, the following research projects and scientific questions are investigated in the research group of the author, partly in cooperation with university institutes and industrial companies:

- Development of a non-linear viscoelastic material law for FE-simulations of dynamically excited high performance rubber goods, e. g. rolling or sliding tires.
- Analysis of filler network morphology and filler distribution between the phases of multi-component rubber blends by TEM-, dielectric- and dynamic-mechanical investigations.
- Online application of the dielectric characterization method for analyzing the morphological evolution during compounding of elastomer composites.
- Continuation of the investigations of surface structure of colloidal fillers by static gas adsorption and application of the technique to new types of fillers like silica or plasma blacks.

References:

1. B. B. Mandelbrot, "Fractals: Form, Chance and Dimension," W.H. Freeman and Co., San Francisdo, 1977.

2. B. B. Mandelbrot, "The Fractal Geometry of Nature," W. H. Freeman and Co., New York, 1982.

3. P. Meakin, Prog. Solid State Chem. **20**, 135 (1990).

4. M. Y. Lin, H.N. Lindsay, D. A. Weitz, R. C. Ball, and R. Klein, Nature **339**, 360 (1989).

5. T. A. Witten and M. E. Cates, Science **232**, 1607 (1986).

6. Bunde and S. Havlin, Eds., "Fractals and Disordered Systems, "Springer Verlag, Berlin, Heidelberg, 1991.

7. Bunde and S. Havlin, Eds., "Fractals in Science, " Springer Verlag, Berlin, Heidelberg, NY, 1994.

8. B. Jullien, New J. Chem. **14**, 239 (1990)

9. T. A. Witten and L. M. Sander, Phys. Rev. Lett. **47**, 1400 (1981); Phys. Rev. B: Condens. Matter **B27**, 5686 (1983).

10. P. Meakin, Phys. Rev. **A 29**, 997 (1984).

11. R. C. Ball and R. Jullien, J. Phys. (Paris) Lett. **45**, L103 (1984)

12. P. Meakin, Adv. Colloid Interface Sci. **28**, 249 (1988).

13. D. A. Weitz and M. Oliveria, Phys. Rev. Lett. **52**, 1433 (1983).

14. P. Meakin, B. Donn and G. W. Mulholland, Langmuir **5**, 510 (1989).

15. C. M. Megaridis and R. A. Dobbins, Combust. Sci. and Tech. **71**, 95 (1990).

16. R. J. Samson, G. W. Mulholland and J. W. Gentry, Langmuir **3**, 272 (1987).

17. D. N. Sutherland, Nature **226**,1241 (1970).

18. G. Heinrich and M. Klüppel, Kautschuk Gummi Kunstst. **54**, 159 (2001).

19. A.-L. Barabasi and H. E. Stanley, "Fractal concepts in surface growth", Cambridge University Press, 1996; A.-L. Barabasi, M. Araujo and H. E. Stanley, Phys. Rev. Lett. **68**, 3729 (1992).

20. A. Schröder, M. Klüppel, R. H. Schuster and J. Heidberg, Kautschuk Gummi Kunstst. **54**, 260 (2001).

21. T. A. Witten, M. Rubinstein and R. H. Colby, J. Phys. II (France) **3**, 367 (1993)

22. M. Klüppel and G. Heinrich, Rubber Chem. Technol. **68**, 623 (1995).

23. M. Klüppel, R. H. Schuster and G. Heinrich, Rubber Chem. Technol. **70**, 243 (1997).

24. G. Heinrich and M. Klüppel, Adv. Polym. Sci. **160**, 1 (2002)

25. D. Brown, PhD Thesis, University of Cambridge, UK, 1987.

26. J.-B. Donnet, R. C. Bansal, M. J. Wang, Eds., "Carbon Black: Science and Technology", Marcel Decker Inc., New York, Hongkong, 1993

27. G. Kraus, Ed., "Reinforcement of Elastomers", Interscience Pub., New York, London, Sydney, 1965

28. A. R. Payne, J. Appl. Polym. Sci. **6**, 57 (1962).

29. A. R. Payne, J. Appl. Polym. Sci. **7**, 873 (1963).

30. A. R. Payne, J. Appl. Polym. Sci. **8**, 2661 (1964).

31. A. R. Payne, Trans. IRI **40**, T135 (1964).

32. A. R. Payne, in G. Kraus, Ed., "Reinforcement of Elastomers", Chap. 3, Interscience Publ., N. Y., London, Sydney 1965

33. A. R. Payne, J. Appl. Polym. Sci. **9**, 2273, 3245 (1965).

34. A. R. Payne, J. Appl. Polym. Sci. **16**, 1191 (1972).

35. A. R. Payne, Rubber Chem. Technol. **36**, 432 (1963)

36. A. I. Medalia, Rubber Chem. Technol. **46**, 877 (1973)

37. A. I. Medalia, Rubber Chem. Technol. **47**, 411 (1974)

38. A. Voet and F. R. Cook, Rubber Chem. Technol. **40**, 1364 (1967)

39. A. Voet and F. R. Cook, Rubber Chem. Technol. **41**, 1215 (1968)

40. N. K. Dutta and D. K. Tripathy, Kautschuk Gummi Kunstst. **42**, 665 (1989)

41. N. K. Dutta and D. K. Tripathy, J. Appl. Polym. Sci. **44**, 1635 (1992)

42. N. K. Dutta and D. K. Tripathy, Polymer Testing **9**, 3 (1990)

43. J. D. Ulmer, W. L. Hergenrother and D. F. Lawson, Rubber Chem. Technol. **71**, 637 (1998)

44. M.-J. Wang, W. J. Patterson and G. B. Ouyang, Kautschuk Gummi Kunstst. **51**, 106 (1998)

45. B. Freund and W. Niedermeier, Kautschuk Gummi Kunstst. **51**, 444 (1998)

46. K. Mukhopadhyay and D. K. Tripathy, J. Elastomers and Plastics **24**, 203 (1992)

47. M.-J. Wang, Rubber Chem. Technol. **71**, 520 (1998)

48. A. Bischoff, M. Klüppel and R. H. Schuster, Polym. Bulletin **40**, 283 (1998)

49. S. Vieweg, R. Unger, G. Heinrich and E. Donth, J. Appl. Polym. Sci. **73**, 495 (1999)

50. A. R. Payne and W. F. Watson, Rubber Chem. Technol. **36**, 147 (1963)

51. T. Amari, K. Mesugi and H. Suzuki, Progr. in Organic Coatings **31**, 171 (1997)

52. A. R. Payne and R. E. Wittaker, Rheol. Acta **9**, 91 (1970)

53. A. R. Payne and R. E. Wittaker, Rheol. Acta **9**, 97 (1970)

54. G. Kraus, J. Appl. Polym. Sci., Appl. Polym. Symp., **39**, 75 (1984).

55. van de Walle, C. Tricot and M. Gerspacher, Kautsch. Gummi Kunstst. **49**, 173 (1996).

56. C.-R. Lin, Y.-D. Lee, Macromol. Theory Simul. **5**, 1075 (1996); ibid. **6**, 102 (1997).

57. G. Heinrich, E. Straube and G. Helmis, Adv. Polym. Sci. **85**, 33 (1988).

58. L. Mullins, Rubber Chem. Technol. **21**, 281 (1948)

59. L. Mullins and N. R. Tobin, Rubber Chem. Technol. **30**, 355 (1957)

60. L. Mullins, in G. Kraus, Ed., "Reinforcement of Elastomers", Interscience Publ., N. Y., London, Sydney 1965

61. A. I. Medalia, Rubber Chem. Technol. **51**, 437 (1978)

62. S. F. Edwards and T. A. Vilgis, Rep. Prog. Phys. **51**, 243 (1988); Polymer **27**, 483 (1986)

63. E. Guth and O. Gold, Phys. Rev. 53, 322 (1938)

64. G. Huber, PhD-Thesis, University Mainz, Germany (1997)

65. G. Huber and T. A. Vilgis, Euro. Phys. J. B **3**, 217 (11998); ibid. Kautschuk Gummi Kunstst. **52**, 102 (1999)

66. G. Heinrich and T. A. Vilgis, Macromolecules **26**, 1109 (1993)

67. U. Eisele and H.-K. Müller, Kautschuk Gummi Kunstst. **43**, 9 (1990)

68. F. Bueche, J. Appl. Polym. Sci, **4**, 107 (1960); **5**, 271 (1961)

69. S. Govindjee and J. Simo, J. Mech. Phys. Solids **39**, 87 (1991); **40**, 213 (1992)

70. E. M. Dannenberg, Rubber Chem. Technol. **47**, 410 (1974)

71. Z. Rigbi, Adv. Polym. Sci. **36**, 21 (1980)

72. G. R. Hamed and S. Hatfield, Rubber Chem. Technol. **62**, 143 (1989)

73. J. A. Haarwood, L. Mullins and A. R. Payne, J. Appl. Polym. Sci. **9**, 3011 (1965)

74. J. A. Haarwood and A. R. Payne, J. Appl. Polym. Sci. **10**, 315, 1203 (1966)

75. M. Klüppel and J. Schramm, "An Advanced Micro-Mechanical Model of Hyperelasticity and Stress Softening of Reinforced Rubbers", S. 211 in A. Dorfmann, A. Muhr (Eds.), „Constitutive Models for Rubber", A. A. Balkema, Rotterdam, 1999

76. M. Klüppel and J. Schramm, Macromol. Theory Simul. **9**, 742 (2000)

77. M. Kaliske and G. Heinrich, Rubber Chem. Technol. **72**, 602 (1999)

78. G. Heinrich and M. Kaliske, Computational and Theoretical Polym. Sci **7**, 227 (1997)

79. A. Schröder, "Charakterisierung verschiedener Rußtypen durch systematische statische Gasadsorption" PhD-Thesis, University Hannover (2000)

80. A. Schröder, M. Klüppel and R. H. Schuster, Kautschuk Gummi Kunstst. **52**, 814 (1999).

81. A. Schröder, M. Klüppel and R. H. Schuster, Kautschuk Gummi Kunstst. **53**, 257 (2000).

82. A. Schröder, M. Klüppel, R. H. Schuster and J. Heidberg, Carbon **40**, 207 (2002)

83. M. Klüppel, A. Schröder, R. H. Schuster and J. Schramm, "The disordered morphological structure of carbon black", Paper No. XLI, ACS Rubber Division Meeting, Dallas, Texas, 4. - 6. April 2000

84. M. Klüppel, A. Schröder, G. Heinrich, R. H. Schuster and J. Heidberg, "Universality of carbon black surface roughness", Proceedings: Kautschuk-Herbst-Kolloquium 2000, P. 193, 6.-8. Nov., 2000

85. R. H. Schuster, M. Klüppel, J. Schramm and G. Heinrich, "Concerning the Relation between the Fractal Nature of Carbon Black Networks and the Dynamic Behavior of Elastomers at Low Strain Amplitude", Paper No. 56, ACS Rubber Division Meeting, Indianapolis, Indiana, 5. - 8. May 1998

86. M. Klüppel, R. H. Schuster and J. Schaper, Rubber Chem. Technol. **72**, 91 (1999)

87. R. H. Schuster, J. Meier and M. Klüppel , Kautschuk Gummi Kunstst. **53**, 663 (2000).

88. R. H. Schuster, M. Klüppel and Th. Früh, "Reinforcement of Polydiene Elastomers by Kinetically Aggregated Microgels", Paper No. 53, ACS Rubber Division Meeting, Anaheim, California, 6. - 9. May 1997

89. M. Klüppel and J. Meier, "Modeling of Soft Matter Viscoelasticity for FE-Applications", in D. Besdo, R. H. Schuster and J. Ihlemann (Eds.), "Constitutive Models for Rubber II", p. 11, A. A. Balkema, Lisse, Abingdon, Exton, Tokyo, 2001

90. H. Raab, J. Fröhlich and D. Göritz, Kautschuk Gummi Kunstst. **53**, 137 (2000)

91. W. Niedermeier et al., Rubber Chem. Technol. **67**, 148 (1994)

92. W. Niedermeier et al., Kautschuk Gummi Kunstst. **47**, 799 (1994)

93. R. P. Hjelm, W. A. Wampler and P. A. Serger, Paper No. 5, ACS Rubber Division Meeting, 21.-24. May, 1991

94. T. P. Rieker, S. Misono and F. Ehrenbourger-Dolle, Langmuir **15**, 914 (1999)

95. T. P. Rieker, M. Hindermann-Bischoff and F. Ehrenbourger-Dolle, Landmuir **16**, 5588 (2000)

96. J. Fröhlich, St. Kreitmeier and D. Göritz, Kautschuk Gummi Kunstst. **51**, 370 (1998).

97. T. W. Zerda, H. Yang and M. Gerspacher, Rubber Chem. Technol. **65**, 130 (1992)

98. J. M. K. Isamail and P. Pfeifer, Langmuir **10**, 1532 (1994)

99. J. M. K. Isamail, Langmuir **8**, 360 (1992)

100. P. Pfeifer, M.Obert and M.W. Cole; Proc. R. Soc. Lond.; **A 423**, 169, (1989).

101. P. Pfeifer and M.W. Cole; New J. Chem.; **14**, 221, (1990).

102. B.C. Lippens, B.G. Linsen and J.H. De Boer; J. Catalysis; **3**, 32, (1964).

103. A. W. Adamson and J. Ling, Adv. Chem. **33**, 51 (1961).

104. I. Langmuir, J. Am. Chem. Soc. **40**, 1316 (1918).

105. R. H. Fowler and E. A. Guggenheim, "Statistical Thermodynamics", Cambridge Univ. Press, Cambridge, 1952

106. J. F. Douglas, Macromolecules **22**, 3707 (1989)

107. T. A. Vilgis and G. Heinrich, Macromolecules **27**, 7846 (1994)

108. C. R. Herd, G. C. McDonald and W. M. Hess, Rubber Chem. Technol. **65**, 107 (1992)

109. M. Gerspacher and C. P. O'Farrell, Kautschuk Gummi Kunstst. **45**, 97 (1992).

110. A. Le Mehaute, M. Gerspacher and C. Tricot, "Fractal Geometry", in Ref. 26

111. A. I. Medalia, J. Colloid Interface Sci. **24**, 393 (1967)

112. A. I. Medalia and F. A. Heckman, Carbon **7**, 567 (1996)

113. R. Viswanathan and M. B. Heaney, Phys. Rev. Lett. **75**, 4433 (1995)

114. F. Ehrburger-Dolle and M. Tence, Carbon 28, 448 (1990)

115. B. Oppermann, "Einfluß der Rußdispersion auf die elektrische Leitfähigkeit", PhD-Thesis, University Hannover (1994)

116. F. A. Heckman and A. I. Medalia, J. Inst. Rubber Ind. **3**, 66 (1969)

117. W. M. Hess, V. E. Chirico and K. A. Burgess, International Rubber Conf. Prague, Sept. 1973

118. M. Gessler, Rubber Chem. Technol. **43**, 943 (1970)

119. U. Sgodzaj, "Einfluß der Polymerstruktur auf die Rheologie und das Dispersionsverhalten von BR- und SBR-Systemen", PhD-Thesis, University Karlsruhe (2001)

120. K.-M. Jäger and D. H. McQueen, "Fractal structures in carbon black polymer composites", Proceedings: Kautschuk-Herbst-Kolloquium 2000, P. 145, Hannover, 6.-8.Nov. 2000; ibid. Polymer **42**,9575 (2001)

121. A. I. Medalia, Rubber Chem. Technol. **59**, 432 (1986).

122. H. Boettger and U. V. Bryksin, "Hopping conduction in solids", Berlin Verlag Akademie, 1986

123. K. Miyasaka, Nippon Gomu Kyokaishi **58**, 561 (1985)

124. C. P. O'Farrell, M. Gerspacher and L. Nikiel, Kautschuk Gummi Kunstst. **53**, 701 (2000).

125. N. Probst and E. Grivei, "Carbon black structure, measurement techniques and effect on properties", Proceedings: Kautschuk-Herbst-Kolloquium 2000, P. 205, Hannover, 6.-8 Nov. 2000

126. I. Balberg, Trends in Stat. Phys. **2**, 39 (1998); ibid. Phys. Rev. Lett. **59**, 1305 (1987)

127. Z. Rubin, A. Sunshine, M. B. Heaney, I. Bloom and I. Balberg, Phys. Rev. B **59**, 12196 (1999)

128. D. Stauffer and A. Aharoni, "Introduction to percolation theory", Taylor and Francis, London, 1992

129. J. A. Ayala, W. M. Hess, A. O. Dotson and G. A. Joyce, Rubber Chem. Technol. **63**, 747 (1990)

130. W. M. Hess and V. E. Chirico, Proc. Plast. Rubber Inst. 1st Eur. Conf., Brussels, April 1975.

131. L. K. H. van Beek, "Dielectric behavior of heterogeneous systems", in J. B. Birks (Ed.), "Progress in dielectrics", Vol. 7, Heywood, London, p. 69-114, 1967

132. G. B. Ouyang, Kautschuk Gummi Kunstst., in press.

133. G. Schwartz, S. Cerveny and A. J. Marzocca, Polymer **41**, 6589 (2000).

134. F. Kremer, T. A. Ezquerra, M. Mohamadi, W. Bauhofer, T. A. Vilgis and G. Wegner, Solid State Commun. **66**, 153 (1988).

135. K.-M. Jäger, D. H. McQueen, I. A. Tchmutin, N. G. Ryvtina and M. Klüppel, J. Phys. D: Appl. Phys. **34**, 2699 (2001)

136. Y. Gefen, A. Aharony and S. Alexander, Phys. Rev. Lett. **50**, 77 (1983)

137. S. Havlin and A. Bunde, "Percolation II", in Ref. 6

138. A. Kastner, I. Alig, G. Heinrich and M. Klüppel, in preparation.

139. M. Klüppel, Kautschuk Gummi Kunstst. **50**, 282 (1997).

140. G. Georg, A. Böhm, M. Nguyen, J. Appl. Polym. Sci. **55,** 1041 (1995)

141. J. Fröhlich and W. Niedermeier, Proceedings: IRC 2000, P. 107, Nürnberg, 4. - 7. Sept. 2000.

142. J. Fröhlich and H. D. Luginsland, Proceedings: Kautschuk-Herbst-Kolloquium 2000, P. 13, Hannover, 6.-8 Nov. 2000

143. T. Wang, M.-J. Wang, J. Shell and N. Tokita, Kautsch. Gummi Kunstst. **53**, 497 (2000)

144. R. H. Schuster, "Verstärkung von Elastomeren durch Ruß", Teil 1, WDK - Grünes Buch Nr. 40, 1989

145. G. R. Cotten, Rubber Chem. Technol. **48**, 548 (1975)

146. G. Kraus and J. T. Gruver, Rubber Chem. Technol. **41**, 1256 (1968)

147. B. Meissner, J. Appl. Polym. Sci. **18**, 2483 (1974)

148. J. J. Brennan, T. E. Jermyn and B. B. Boonstra, Gummi Asbest Kunstst. **18**, 266 (1965)

149. B. B. Boonstra, J. Appl. Polym. Sci. **11**, 389 (1967)

150. A. K. Sircar and A. Voet, Rubber Chem. Technol. **43**, 973 (1970)

151. S. Wolff, M.-J. Wang and E.-H. Tan, Rubber Chem. Technol., **66**, 163 (1993)

152. A. V. Chapman, W. S. Fulton and A. J. Tinker, "Carbon black elastomer interaction: Bound rubber measurements at elevated temperature", Proceedings: Kautschuk-Herbst-Kolloquium 2000, P. 23, Hannover, 6. − 8. Nov., 2000

153. N. Kida, M. Ito, F. Yatsunyanagi and H. Kaido, J. Appl. Polym. Sci. **61**, 1345 (1996)

154. A. K. Sircar and T. G. Lamond, Rubber Chem. Technol. **48**, 79, 89 (1975)

155. Y. Kantor andI. Webman, Phys. Rev. Lett. **52**, 1891 (1984)

156. S. K. Friedlander, H. D. Jang and K. H. Ryu, Appl. Phys. Lett. **72**, 173 (1998)

157. S. K. Friedlander, K. Ogawa and M. Ullmann, J. Pol. Sci., Pol. Phys. **38**, 2658 (2001)

158. M. Müller, PhD-Thesis, University Hannover, in preparation.

159. M. Müller and R. H. Schuster, Proceedings: German Rubber Conference, Nürnberg, 4.-7. Sept., 2000

160. N. W. Tschoegl, "The phenpmenological theory of linear viscoelastic behavior", Springer, Berlin, Heidelberg, N. Y., 1989

161. P. G. J. van Dongen and M. H. Ernst, Phys. Rev. Lett. **54**, 1396 (1985); ibid. J. Phys. A, **18**, 2779 (1985).

162. R. M. Ziff, E. D. McGrady and P. Meakin, J. Chem. Phys. **82**, 5269 (1985).

163. G. Heinrich and E. Straube, Acta Polymerica **35**, 115 (1984)

164. G. Heinrich and E. Straube, Polym. Bulletin **17**, 247 (1987)

165. M. Rubinstein and S. Panyukow, Macromolecules **30**, 8036 (1997)

166. E. Straube, V. Urban, W. Pyckhout-Hintzen, D. Richter and C. W. Glinka, Phys. Rev. Lett. **74**, 4464 (1995)

167. M. Klüppel, Macromolecules **27**, 7179 (1994)

168. M. Klüppel, H. Menge, H. Schmidt, H. Schneider and R. H. Schuster, Macromolecules **34**, 8107 (2001)

169. S. F. Edwards and T. A. Vilgis, Rep. Prog. Phys. **51**, 243 (1988); Polymer **27**, 483 (1986)

170. M. Klüppel and G. Heinrich, Macromolecules **27**, 3569 (1994)

171. L. J. Fetters, D. J. Lohse, D. Richter, T. A. Witten and A. Zirkel, Macromolecules **27**, 4639 (1994)

172. M. Klüppel, Prog. Colloid Polym. Sci. **90**, 137 (1992)

173. M. Klüppel, J. Appl. Polym. Sci. **48**, 1137 (1993)

174. J. Meier, "Untersuchungen und Modellierungen zur linearen Viskoelastizität von Poly (Styrol-co-Butadien)", PhD-Thesis, Technical University Clausthal (2002)

175. J. Meier, E. Giebeler, M. Klüppel and R. H. Schuster, " Macro- and microstructural determined viscoelastic behavior by tailor-made polydiens", Paper No. XX, ACS Rubber Division Meeting, Provicence, Rhode Island, 24. - 27. April 2001

176. K. Layouni, I. Laiarinandrasana and R. Piquet, "Compressibility induced by damage in carbon black reinforced natural rubber", in J. J. C. Busfield and A. H. Muhr (Eds.), "Constitutive Models for Rubber III", p. 273, A. A. Balkema, Lisse, Abingdon, Exton, Tokyo, 2003

177. H. Luo, M. Klüppel and H. Schneider, Macromolecules, in press

178. M. Klüppel, J. Meier and G. Heinrich, "Impact of pre-strain on dynamic-mechanical properties of carbon black and silica filled rubbers", in J. J. C. Busfield and A. H. Muhr (Eds.), "Constitutive Models for Rubber III", p. 333, A. A. Balkema, Lisse, Abingdon, Exton, Tokyo, 2003

179. J. D. Brown, "Nonlinear dynamic behavior of filled elastomers at small strain amplitudes", PhD-Thesis, Rensselaer Polytechnic Institute, Troy, New York (1997)

180. L. Chazeau, J. D. Brown, L. C. Yanyo and S. S. Sternstein, Polym. Composites **21**, 202 (2000)

Appendix A:

G. Heinrich and M. Klüppel,
"A hypothetical mechanism of carbon black formation based on molecular ballistic deposition"

Abstract

The paper summarizes numerical and analytical results concerning the mechanism of carbon black formation during processing and the generation of rough surfaces in the framework of molecular ballistic deposition. It provides a theoretical background for explaining the detected universality of carbon black surface roughness with fractal dimension $d_f \approx 2.5 - 2.6$ (as described in Section 3.1.1). It is shown that in many models the generated surface falls into an universality class with a surface fractal dimension close to the one obtained for the furnace blacks from static gas adsorption measurements. This demonstrates that the universality of surface roughness of carbon black can be traced back to the deeper physical origin of correlation between neighboring sites during the growth process of the surface in the processing reactor.

Appendix B:

G. Heinrich and M. Klüppel,
"Recent advances in the theory of filler networking in elastomers"
Adv. Polym. Sci. 160, 1 (2002)

Abstract

The paper presents a review of various theoretical approaches of filler networking in elastomer composites that focus on a micro-mechanical explanation of the pronounced dependency of the complex modulus on strain amplitude (Payne effect). The described models consider the breakdown and re-aggregation of filler-filler bonds to be the main mechanism leading to the Payne effect. They mainly differ in the assumptions concerning the nature and strength of filler-filler bonds and the arrangement of filler particles in the rubber matrix. Accordingly, macroscopic consequences of the dynamics of polymer bridges between adjacent filler particles (NJ-model) as well as van der Waals bonds under strain (Kraus model, VTG-model) are considered. The two other models (L-N-B-model, CCA-model) start from different arrangements of filler particles in fractal networks, i. e. Percolation- and CCA-networks, respectively, while the filler-filler bonds are described in a similar way by elastic constants that are assumed to be controlled by the rubber phase around fillers (compare Section 4.3). Both of these models are based on the Kantor-Webman approach concerning the elasticity of filler chain aggregates with tension- and bending-twisting deformations of filler-filler bonds (considered in Section 5.1.2).

Appendix C:

M. Klüppel and G. Heinrich,

"Fractal structures in carbon black reinforced rubbers"
Rubber Chem. Technol. 68, 623 (1995)

Abstract

The paper represents a first attempt for an explanation of the specific mechanical and electric properties of carbon black filled rubbers by referring to a fractal analysis of the filler network. Many basic features of rubber reinforcement by fractal filler networks are outlined in this article. In particular, the fractal analysis of primary carbon black aggregates (considered in Section 3.2.1) is described in some detail. The model of kinetic cluster-cluster aggregation of filler particles in elastomers is introduced and the power law behavior of the small strain modulus (considered in Section 5.1.3) is formulated and compared to experimental data from the literature. The non-universal value of the percolation exponent of the dc-conductivity of carbon black filled rubbers (considered in Section 4.2.1) is analyzed by referring to a kinetic aggregation mechanism of colloidal fillers in elastomers. The scaling behavior of the ac-conductivity of conducting composites in the high frequency regime (considered in Section 4.2.2) is shown to be related to the anomalous diffusion of charge carriers on fractal filler clusters.

Appendix D:

M. Klüppel, R. H. Schuster and G. Heinrich,
"Structure and properties of reinforcing fractal filler networks in elastomers"
Rubber Chem. Technol. 70, 243 (1997)

Abstract

The paper describes basic structure-property relationships of two different models of fractal filler networks in elastomers, the percolation model and the model of kinetic cluster-cluster aggregation (CCA), respectively. Thereby, mechanical and electrical properties are considered and compared to experimental results. The main interest focuses on various interrelationships between the fractal exponents that refer to the characteristic scaling properties of the two model. In particular, the scaling law for the elastic modulus with filler concentration (considered in Section 5.1.3) is analyzed, which offers a significantly different prediction for the two models. It becomes obvious that, contrary to the CCA-model, the predicted scaling exponent of percolation theory does not agree with the experimental value. Furthermore, the influence of anomalous diffusion of charge carriers on the conductivity in the high frequency regime (considered in Section 4.2.2) is analyzed for both types of fractal filler networks. It is found that the mechanical properties can be well described by the CCA-model, while the dielectric properties give a better fit to the percolation model.

Appendix E:

A. Bischoff, M. Klüppel and R. H. Schuster,
"Mechanical behavior at low strain of microgel containing elastomers"

Abstract

The paper considers the mechanisms of rubber reinforcement due to the incorporation of colloidal fillers, by analyzing the effects of polymeric model fillers (microgels) of various size, stiffness and chemical nature on the elastic modulus of composites, primary at low strain amplitude. The microgels are well suited for testing micro-mechanical models of reinforcement, since TEM-investigations shows that they have a spherical shape of definite size with an almost monodisperse size distribution. In addition, the stiffness can be altered by the state of curing and the surface activity, as described by the solubility parameter, can be modified by applying different polymers for the preparation of the microgels or performing a chemical treatment of the surface. The preparation procedure of different kinds of microgels is described in some detail. It is found that the predictions of the kinetic cluster-cluster aggregation model (considered in Section 5.1) fit well to the measured dependency of the Young modulus on microgel concentration and size. The data obtained at low microgel concentations can be well understood on the basis of hydrodynamic reinforcement by rigid microgel clusters, if a kinetic aggregation mechanism is assumed that depends on the size and concentration of microgels. Measurements of the Payne effect show that the breakdown of the clusters appears at relatively small strain amplitudes of about 0.1 %, implying that the strength of microgel clusters is relatively weak.

Appendix F:

M. Klüppel and J. Schramm,
"A generalized tube model of rubber elasticity and
stress-softening of filler reinforced elastomer systems"
Macromol. Theory Simul. 9, 742 (2000)

Abstract

The paper describes a first approach towards a constitutive micro-mechanical material model of hyperelasticity and stress softening of reinforced rubbers with well defined microscopic material parameters (considered in Section 5). The path integral formulation of rubber elasticity, representing the physical background of the applied non-affine tube model, is briefly reviewed. The Edwards-Vilgis approach of finite network extensibility is introduced and compared to the classical inverse Langevin approach. It is found that the proposed generalized tube model of rubber elasticity represents a constitutive physical basis for the description of quasi-static stress-strain properties of unfilled rubber up to large strain. The tube model with non-affine tube deformations is shown to fulfill the "plausibility criterion" (considered in Section 5.2.2), allowing for a description of various deformation modes simply on the basis of uniaxial stress-strain fitting parameters. The consideration of hydrodynamic reinforcement by rigid filler clusters and stress-induced, irreversible filler cluster breakdown allows for an extension of the model to filler reinforced rubbers. By applying a strain-or pre-strain dependent hydrodynamic amplification factor, a fair simulation of stress softening of filled rubbers is obtained, though the presented concept is not constitutive. Nevertheless, it constitutes a conceptual basis for the development of a constitutive theory (described in Section 5) that can be applied to any quasi-static deformation mode.

Lebenslauf

Angaben zur Person:

Name: Manfred Klüppel

Akad. Grad: Dr. rer. nat.

Geburtsdatum: 04. 10. 1954

Geburtsort: Medelon/Westfalen

Nationalität: Deutsch

Anschrift: D-30974 Wennigsen, Am Tongrund 1

Familienstand: verheiratet, ein Kind (geb. 1981)

Schulischer Bildungsgang:

1961 - 1966 Volksschule Medelon

1966 - 1971 Progymnasium Medebach

1971 - 1974 Alte Landesschule Korbach

1974 Allgemeine Hochschulreife

Universitärer Bildungsgang:

1974 - 1982 Physikstudium an der Philipps Universität Marburg/Lahn

1982 - 1988 Mitarbeit im Wissenschaftsbereich "Grundlagen der Physik und mathematische Physik" unter Leitung von Prof. Dr. G. Ludwig

1982 Diplomarbeit bei Prof. Dr. G. Ludwig, Thema: "Schwarze Löcher"

1982 Diplomhauptprüfung

Promotion bei Prof. Dr. H. Neumann, Thema: "Axiomatischer Aufbau der nichtrelativistischen Quantentheorie für eine Wechselwirkung mit klassischen Feldern"

Wissenschaftliche Tätigkeit:

1982 - 1987 Wissenschaftlicher Mitarbeiter (befristet) an der Philipps-Universität Marburg/Lahn

1989 - 1993 Wissenschaftlicher Mitarbeiter (befristet) am Deutschen Institut für Kautschuktechnologie, Hannover

1995 - 2002 Wissenschaftlicher Angestellter (unbefristet) am Deutschen Institut für Kautschuktechnologie

seit 2002 Abteilungsleiter am Deutschen Institut für Kautschuktechnologie, Forschungsbereich: Materialkonzepte und Modellierung

Lehrtätigkeit:

1982 - 1987 Anleitung: Physikalisches Praktikum für Naturwissenschaftler

seit 1989 Vorlesungen am Deutschen Institut für Kautschuktechnologie: "Viskoelastizität-Rheologie"

seit SS 2003 Vorlesungen an der Universität Hannover: "Fraktale Strukturen und Skalengesetze ungeordneter Festkörper" "Molekularstatistische Mechanik polymerer Werkstoffe"

Erklärung:

Hiermit erkläre ich an Eides statt, dass ich die vorliegende Arbeit selbstständig und ohne fremde Hilfe verfasst und nur die angegebenen Quellen und Hilfsmittel verwendet habe. Ergebnisse aus anderen wissenschaftlichen Arbeiten wurden als solche gekennzeichnet. Diese Arbeit wurde bisher weder im In- noch im Ausland in gleicher oder ähnlicher Form in einem Prüfungsverfahren vorgelegt.

Hannover, im August 2004   (Dr. Manfred Klüppel)